CHALMERS
UNIVERSITY OF TECHNOLOGY

a)

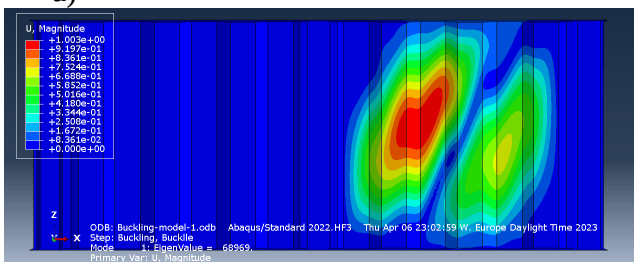

b)

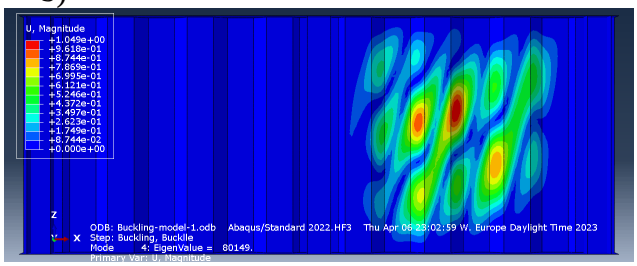

c)

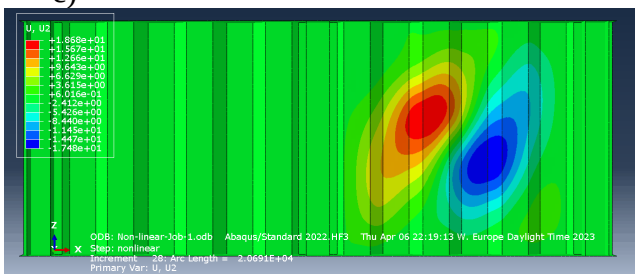

d)

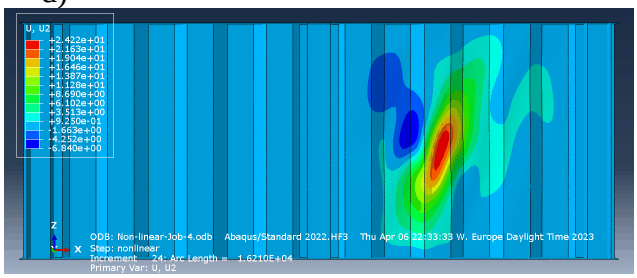

Imperfection Sensitivity of the Shear Behaviour of Corrugated Web Beams

Master's thesis in Master Program Structural engineering and building technology

Shahriar Khalili

Department of Architecture and Civil Engineering
Division of Structural Engineering
CHALMERS UNIVERSITY OF TECHNOLOGY
Master's Thesis
Gothenburg, Sweden 2023

MASTER'S THESIS

Imperfection Sensitivity of the Shear Behaviour of Corrugated Web Beams

Master's Thesis in Structural Engineering and Building Technology

Shahriar Khalili

Department of Architecture and Civil Engineering
Division of Structural engineering
CHALMERS UNIVERSITY OF TECHNOLOGY
Göteborg, Sweden 2023

Imperfection Sensitivity of the Shear Behaviour of Corrugated Web Beams

Master's Thesis in Structural Engineering and Building Technology

Shahriar Khalili

© Shahriar Khalili, 2023.

Institutionen för arkitektur och samhällsbyggnadsteknik
Chalmers tekniska högskola, 2023

Examiner: Mozhdeh Amani, Department of Architecture and Civil Engineering, CHALMERS

Supervisors: Mozhdeh Amani, Mohammad Al-Emrani and Fatima Hlal, Department of Architecture and Civil Engineering, CHALMERS

Department of Architecture and Civil Engineering
Division of Structural Engineering
Chalmers University of Technology
SE-412 96 Göteborg
Sweden
Telephone: + 46 (0)31-772 1000

Cover:
Figures are collected from FEM analysis of model-1, Figure (a&b) indicate critical buckling mode for nonlinear analysis with initial imperfection magnitude equal to respectively a_{max}/200 and t_w, Figure (c&d) are respectively corresponding failure for Figure (a&b) and indicate out of plane deflection.

Department of Architecture and Civil Engineering
Göteborg, Sweden, 2023

Imperfection Sensitivity of the Shear Behaviour of Corrugated Web Beams

Master's thesis in Structural Engineering and Building Technology

Shahriar Khalili

Department of Architecture and Civil Engineering
Division of Structural Engineering
Chalmers University of Technology

ABSTRACT

This thesis investigates the imperfection sensitivity of the shear behavior of stainless steel beams with corrugated webs, with the main objective of verifying the shear resistance design equations in EN 1993-1-5. Firstly, a comprehensive literature study was conducted to acquire deeper knowledge on the subject and generate a database to verify the calculated reduction factor by the Eurocode equations. Afterward Finite Element Modeling analysis using ABAQUS was done to consider the imperfection sensitivity of the shear behavior of beams with different geometric parameters. 17 different parametric models of stainless steel corrugated web beams were considered to cover various slenderness ratios and simulations by using Python code were run. Nonlinear analysis for the mentioned models was performed while considering 20 buckling modes as patterns of the initial imperfection with different amplitudes of $a_{max}/200$ (a_{max} is the larger length between inclined and horizontal fold), t_w (web thickness), and $h_w/200$ (h_w is web height). Lastly, a discussion is conducted to evaluate the use of the Eurocode's design equations for stainless steel beams.

Key words: Corrugated web, Stainless steel, Imperfection sensitivity, Shear resistance, Buckling modes, Abaqus simulation, Nonlinear behaviour.

Känslighet för imperfektion i tvärkraftsbeteende hos balkar med vågformade nät

Examensarbete inom masterprogrammet Konstruktionsteknik och Byggnadsteknologi

Shahriar Khalili

Institutionen för arkitektur och samhällsbyggnadsteknik
Avdelningen för Byggnadsteknik
Chalmers tekniska högskola

SAMMANFATTNING

Denna avhandling undersöker känsligheten för ojämnhet i skjuvningen hos rostfria stålbalkar med vågformade tvärsnitt, med huvudsyftet att verifiera dimensioneringsformlerna för skjuvmotstånd enligt EN 1993-1-5. Först genomfördes en omfattande litteraturstudie för att förvärva djupare kunskap om ämnet och generera en databas för att verifiera den beräknade reduktionsfaktorn enligt Eurocode-formlerna. Därefter utfördes en analys med ändliga elementmetoden med hjälp av ABAQUS för att beakta känsligheten för ojämnhet i skjuvningen hos balkar med olika geometriska parametrar. 17 olika parametriska modeller av rostfria stålbalkar med vågformade tvärsnitt beaktades för att täcka olika slankhetsförhållanden, och simuleringar genomfördes med hjälp av Python-kod. Icke-linjär analys för dessa modeller utfördes samtidigt som 20 bucklingslägen beaktades som mönster för den initiala ojämnheten med olika amplituder av $a_{max}/200$ (där a_{max} är den längre längden mellan lutande och horisontellt veck), t_w (tvärsnittets tjocklek) och $h_w/200$ (där h_w är tvärsnittets höjd). Slutligen genomförs en diskussion för att utvärdera användningen av Eurocodes designformler för rostfria stålbalkar.

Nyckelord: Vågformade webbar, Rostfritt stål, Känslighet för imperfektioner, Skjuvstyrka, Buktningssätt, Abaqus-simulering, Icke-linjärt beteende

CONTENT

ABSTRACT **I**

SAMMANFATTNING **II**

Preface **VI**

List of figures **VII**

List of tables **XI**

Notations **XII**

1 Introduction **1**

1.1 Background *1*

1.2 Aim and objective *3*

1.3 Limitations *3*

2 Literature study **5**

2.1 Indication of different geometric parameters *5*

2.2 Elastic buckling modes *6*
2.2.1 Local buckling 6
2.2.2 Global buckling 7
2.2.3 Interactive buckling 7

2.3 Review of Eurocode 3 and Commentary to Eurocode *8*
2.3.1 Shear resistance 9
2.3.1.1 Review of commentary to Eurocode 1993-1-5 10

2.4 Database generated by literature review *13*

3 Verification of FEM method **17**

3.1 Simulation of specimen MI2 *17*
3.1.1 FE Modelling of MI2 specimen 17
3.1.2 Verification results for MI2 21

3.2 Simulation of specimen 1001 *24*
3.2.1 FE Modelling of 1001 specimen 24
3.2.2 Verification results for 1001 27

Conclusion for verification of FEM method **30**

Imperfection sensitivity studies **31**

Discussion and conclusion **41**

3.3 Verification of Eurocode equations *41*

4 References **48**

5 Appendix-A **50**

Preface

The present thesis commenced in December 2022 and was carried out until June 2023 as part of an ongoing research project aimed at the design of beams with corrugated webs, particularly those fabricated from stainless steel. Despite the criticality of this topic, information on the subject is scant. In this study, a database comprising of previous tests focused on shear failure has been created to investigate the validation of Eurocode design standards for shear resistance. Concurrently, an ABAQUS analysis was conducted to investigate imperfection sensitivity. The project was conducted at the Department of Structural Engineering, Chalmers University of Technology, Sweden.

The entire work in this thesis was closely monitored by the examiner, Mozhdeh Amani. I express my sincere gratitude to Mozhdeh for her invaluable support that was the essence part in achieving the intended objectives.

I am also thankful to Mohammad Al-Emrani and Fatima Hlal, supervisors of this project, for their indispensable contributions and irreplaceable support.

Finally, I owe a profound debt of gratitude to my wife, Azita Ahmadpour. She has been such a blessing in this period and finishing this project was not possible without her support and kindness.

Göteborg Jun 2023

Shahriar Khalili

List of figures

Figure 1-1 The figure shows different geometries developed by Herman [2] 2

Figure 1-2 Different types of girders used in bridges with usage of corrugated web [4] 3

Figure 2-1 Different shapes for corrugated webs. [5], [6] & [7] 6

Figure 2-2 Local buckling mode, which is from analysis of model 10 mode 16, geometries are presented in Chapter 4. 7

Figure 2-3 Local buckling mode, which is from analysis of model 2 mode 1, geometries are presented in Chapter 4. 7

Figure 2-4 Local interactive buckling mode, which is from analysis of model 10 mode 14, geometries are presented in Chapter 4. 8

Figure 2-5 Global interactive buckling mode, which is from analysis of model 16 mode 4, geometries are presented in Chapter 4. 8

Figure 2-6 Indication of notations. [2] 9

Figure 2-7 Vertical axis presents reduction factor for local buckling mode and horizontal axis indicates corresponding local slenderness ratio. [10]. 13

Figure 2-8 Vertical axis presents reduction factor for global buckling mode and horizontal axis indicates corresponding global slenderness ratio. [10] 13

Figure 3-1 Geometrical parameters of the corrugated web [15] 17

Figure 3-2 Configuration of MI2 in Abaqus. 18

Figure 3-3 Stress strain diagram for mild steel [24] 19

Figure 3-4 Diagram of corresponding eigenvalues for different mesh sizes on the eigenvalue. 20

Figure 3-5 The measured initial imperfection contour of the test specimen (MI2) [15] 20

Figure 3-6 The 28th buckling mode of the FE model MI2 21

Figure 3-7 Shear stress vs. vertical deflection of the middle of the bottom flange in the test beam (MI2) and FE model. 22

Figure 3-8 Deformed shape of test specimen after loading. [15] 23

Figure 3-9 The buckling deformation on maximum load increment. 23

Figure 3-10 The buckling deformation after the maximum loading step. 24

Figure 3-11 The configuration of corrugated web, stiffeners, and flat web panels in 1001 [23]. 25

Figure 3-12 The configuration of corrugated web, stiffeners, flat web panels, loads, and support locations 25

Figure 3-13 The sensitivity of the first eigenvalues to the mesh size in the FE model of 1001. 26

Figure 3-14 The DIC-measured initial imperfection of the corrugated web panel in 1001 [23]. 26

Figure 3-15 The third buckling mode in the FE model of 1001. 27

Figure 3-16 The total applied load vs. the vertical displacement in 1001. 27

Figure 3-17 The buckling deflection at the maximum load increment. 28

Figure 3-18 This contour represents von mises stress values corresponding to the ultimate load. 28

Figure 3-19 Deformed shape of the specimen 1001 after failure [23]. 29

Figure 3-20 Indication of χu extracted by FEM analysis versus calculated χl and χg by Eurocode equations for model-1. 33

Figure 3-21 Indication of χu extracted by FEM analysis versus calculated χl and χg by Eurocode equations for model-2. 34

Figure 3-22 Indication of χu extracted by FEM analysis versus calculated χl and χg by Eurocode equations for model-3. 34

Figure 3-23 Indication of χu extracted by FEM analysis versus calculated χl and χg by Eurocode equations for model-4. 34

Figure 3-24 Indication of χu extracted by FEM analysis versus calculated χl and χg by Eurocode equations for model-5. 35

Figure 3-25 Indication of χu extracted by FEM analysis versus calculated χl and χg by Eurocode equations for model-6. 35

Figure 3-26 Indication of χu extracted by FEM analysis versus calculated χl and χg by Eurocode equations for model-7. 35

Figure 3-27 Indication of χu extracted by FEM analysis versus calculated χl and χg by Eurocode equations for model-8. 36

Figure 3-28 Indication of $\mathcal{X}u$ extracted by FEM analysis versus calculated $\mathcal{X}l$ and $\mathcal{X}g$ by Eurocode equations for model-9. 36

Figure 3-29 Indication of $\mathcal{X}u$ extracted by FEM analysis versus calculated $\mathcal{X}l$ and $\mathcal{X}g$ by Eurocode equations for model-10. 36

Figure 3-30 Indication of $\mathcal{X}u$ extracted by FEM analysis versus calculated $\mathcal{X}l$ and $\mathcal{X}g$ by Eurocode equations for model-11. 37

Figure 3-31 Indication of $\mathcal{X}u$ extracted by FEM analysis versus calculated $\mathcal{X}l$ and $\mathcal{X}g$ by Eurocode equations for model-12. 37

Figure 3-32 Indication of $\mathcal{X}u$ extracted by FEM analysis versus calculated $\mathcal{X}l$ and $\mathcal{X}g$ by Eurocode equations for model-13. 37

Figure 3-33 Indication of $\mathcal{X}u$ extracted by FEM analysis versus calculated $\mathcal{X}l$ and $\mathcal{X}g$ by Eurocode equations for model-14. 38

Figure 3-34 Indication of $\mathcal{X}u$ extracted by FEM analysis versus calculated $\mathcal{X}l$ and $\mathcal{X}g$ by Eurocode equations for model-15. 38

Figure 3-35 Indication of $\mathcal{X}u$ extracted by FEM analysis versus calculated $\mathcal{X}l$ and $\mathcal{X}g$ by Eurocode equations for model-16. 38

Figure 3-36 Indication of $\mathcal{X}u$ extracted by FEM analysis versus calculated $\mathcal{X}l$ and $\mathcal{X}g$ by Eurocode equations for model-17. 39

Figure 3-37 Indication of shear design reduction factors for local buckling which are calculated by both Eurocode equations, extracted from generated database and reduction factors extracted from FEM analysis. 41

Figure 3-38 Indication of shear design reduction factors for global buckling which are calculated by both Eurocode equations, extracted from generated database and reduction factors extracted from FEM analysis. 42

Figure 3-39 Indication of ultimate reduction factors for analyzed models with initial imperfection equal to $amax/200$, recommended model for reduction factor and calculated reduction factor by Eurocode's equations for local buckling. 43

Figure 3-40 Indication of ultimate reduction factors for analyzed models with initial imperfection equal to $amax/200$, recommended model for reduction factor and calculated reduction factor by Eurocode's equations for global buckling. 43

Figure 3-41 Indication of ultimate reduction factors for analyzed models with initial imperfection equal to tw, recommended model for reduction factor and calculated reduction factor by Eurocode's equations for local buckling. 44

Figure 3-42 Indication of ultimate reduction factors for analyzed models with initial imperfection equal to tw, recommended model for reduction factor and calculated reduction factor by Eurocode's equations for global buckling. 45

Figure 3-43 Indication of ultimate reduction factors for analyzed models with initial imperfection equal to $hw/200$, recommended model for reduction factor and calculated reduction factor by Eurocode's equations for local buckling. 46

Figure 3-44 Indication of ultimate reduction factors for analyzed models with initial imperfection equal to $hw/200$, recommended model for reduction factor and calculated reduction factor by Eurocode's equations for global buckling. 46

List of tables

Table 2-1 Test results for 69 experiments, table is extracted from commentary on Eurocode. [10] 11

Table 2-2 Database of all the collected experimental that the author has collected during literature study. 13

Table 3-1 Profile of the test specimen, MI2 (all the dimensions are in mm). 17

Table 3-2 Mechanical properties of carbon steel database published in 2017.[24]. 18

Table 3-3 Mechanical properties of the MI2 FE model. 19

Table 3-4 The first buckling mode eigenvalues for different mesh sizes. 19

Table 3-5 Results of experimental test and analysis by Abaqus. 21

Table 3-6 Profile of the test specimen, 1001 (all the dimensions are in mm) 24

Table 3-7 The material properties that have been used in FE modeling of 1001. ... 25

Table 3-8 The mesh size sensitivity and convergence study in the FE modeling of 1001. 25

Table 3-9 Comparison of the failure load and corresponding vertical displacement in the test and the FEM. 29

Table 3-10 Dimensions of the parametric models in the current study (all the dimensions are in mm) 31

Table 3-11 The results of the nonlinear analyses in ABAQUS in the current parametric FE studies. 32

Table 3-12 Calculated slenderness ratios and reduction factors for both local and global buckling for the parametric models using the Eurocode equations and also indication of critical buckling modes.. 32

Notations

Roman upper-case letters

D_x	Bending stiffness per unit length about x axis
D_z	Bending stiffness per unit length about z axis
E	Young's modulus
I_z	Second moment of area of one corrugation of length w
L	Span of loaded beam (distance between supports)
V_u	Ultimate shear load
$V_{bw,Rd}$	Shear resistance
$V_{bw,Rd}$	Shear resistance
V_{R2}	Global shear resistance
V_{R1}	Local shear resistance

Roman lower-case letters

a_1, a	Flat panel length
a_2, c	Inclined panel width
a_3, d	Corrugation depth
a_4, b	Horizontal distance between flat panels
a_{max}	Greater value of a_1 and a_2
b_f	Flange width
f_{yw}	Yield strength of web
t_f	Flange thickness
t_w	Web tickness
s	Sum of a_1 and a_2
w	The length of one half wave

Greek letters

Θ and α	Corrugation angle
ε_T	Ultimate tensile strain strain
ε_{TT}	True ultimate tensile strain strain
$\lambda_{c,g}$,λ_2	Global buckling slenderness ratio
$\lambda_{c,l}$,λ_1	Local buckling slenderness ratio
σ_T	Ultimate tensile strength
σ_{TT}	Ultimate true tensile strength
σ_y	Yield strength
γ_{M1}	Partial factor
$\tau_{cr,g}$	Critical shear stress for global buckling
$\tau_{cr,l}$	Critical shear stress for local buckling

ν	Poisson's ratio
$\chi_{c,g}$	Reduction factor for global buckling
$\chi_{c,l}$	Reduction factor for local buckling
χ_c	Reduction factor which has lower value between local and global buckling
χ_u	Ultimate ratio between ultimate shear stress and yield shear stress
χ	Reduction factor

1 Introduction

In order to control high bending moments, it is often necessary to increase the height of beams to achieve a higher moment of inertia. However, this can result in a larger slenderness ratio, making the web of the beam more susceptible to buckling. To address this issue, transverse stiffeners have traditionally been used to strengthen flat webs, but this approach has its limitations. To achieve enhanced shear stability without the use of transverse stiffeners, new solutions have been developed for steel webs. One such solution is the use of corrugated webs, which provide significantly higher out-of-plane stiffness. It can be mentioned corrugated webs have exhibited the ability to retain approximately 50% of their maximum shear strength even after buckling occurs, this characteristic serves as a crucial reserve strength, enabling bridge structures to withstand unexpected collapses effectively [1]. Corrugated webs have been used in a wide range of engineering structures, from structural engineering to aerospace and marine engineering. Shear failure in a corrugated web beam may occur due to either local buckling within the corrugation folds or global buckling of the entire web panel or even interactive shear buckling mode might attribute to the interaction between global and local shear buckling modes and governs the shear buckling strength. Another crucial aspect that requires attention is the imperfection sensitivity, as the out-of-plane deflection can lead to a reduction in buckling resistance. This thesis focuses on investigating the imperfection sensitivity of the shear behaviour in corrugated web beams.

1.1 Background

The first idea for bending the web plate of a beam instead of using the regular form of beams with flat webs is developed in a patent by Herman Voshardt in Chicago, USA (1907), Figure 1.1 below presents sketches from the written article [2].

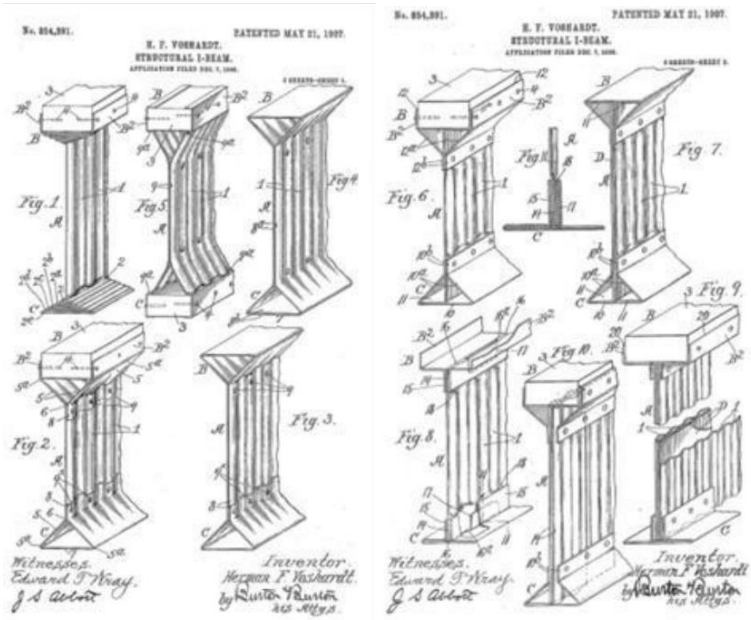

Figure 1-1 The figure shows different geometries developed by Herman [2]

In 1975, Campenon Bernard in Clichy France developed the idea of using corrugated steel webs instead of traditional beams with flat webs for box or I-girders. The first bridge with the use of corrugated steel webs in the girder was built in France (1986), the name of this bridge is Cognac. The girders of this bridge were designed with a combination of prestressed concrete and corrugated steel webs [3].

In Sweden, production of steel girders with a thin corrugated steel web for roof structures began in 1961. Ranaverken AB was a pioneer in this area. These elements were designed to carry light loads, and generally, for medium and small spans, they were suitable [2].

Over the past few years, box girders with corrugated steel webs have emerged as a formidable opponent to other types of girders for wide-span bridges as their manufacturing processes, production technology, and design theory have become more advanced. Many studies are performed on theoretical and practical aspects to develop knowledge in the area of shear buckling and deformation of beams with corrugated webs [3].

In Figure 1-2 Ezzeldin Yazeed Sayed-Ahmed has presented different shapes for girders that is built with usage of corrugated web in girders of bridges.

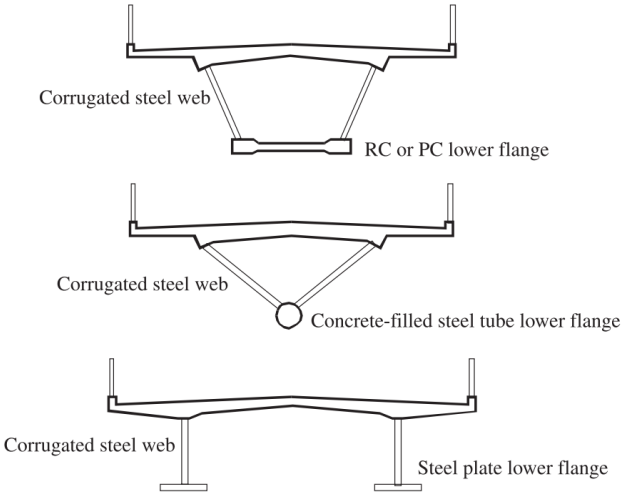

Figure 1-2 Different types of girders used in bridges with usage of corrugated web [4]

1.2 Aim and objective

The main objective of this thesis work is to gain a more comprehensive understanding of the shear imperfection sensitivity of corrugated web beams. Until now, many investigations by scientists have been done, resulting in the development of numerous design formulas. Conducting new tests with different imperfections, geometries, and especially slenderness ratios is necessary to obtain a reliable design standard for the shear resistance of corrugated webs and also to provide a standard for the limitations of production errors; however, this process can be costly. Alternatively, simulation of tests is an efficient solution, but it requires verification of the models to ensure reliable results. Before conducting the finite element simulations, two previously tested beams were simulated and analyzed in ABAQUS. The results showed a low level of error, thereby validating the current FE simulation procedure. In the next step, a parametric FEM analysis was run to simulate different slenderness ratios with varying imperfections. The target is to verify the calculated reduction factors for shear resistance using Eurocode equations, which can be found in EN 1993-1-5. Initially, the author conducted a review of various articles by different scientists to gain a deeper understanding of the subject. In addition, a database of tests conducted was generated to validate the equations.

1.3 Limitations

The main obstacle encountered during the analysis of additional models was the required computational time. As stated in the project scope, a larger volume of data would enable scientists to develop more precise, safer, and optimized design standards. Another limitation of this project was the lack of specific details regarding the conducted tests in the published articles, which made the verification process difficult. To model various geometries in ABAQUS, the author developed a Python code.

However, to model different geometries, the author still needed to create a geometry in ABAQUS and extract the code for use in the PYTHON code. A more efficient solution would be to create a more sophisticated code that allows users to input geometry directly into the code. The following limitation pertains to the literature review, where only four tests were identified specifically examining corrugated stainless steel webs. As a result, the primary database utilized in this thesis comprises test results conducted on carbon steel. In this thesis, the focus is on trapezoidal corrugated webs, but further investigations are necessary to validate the Eurocode design equations, particularly with regards to various types of corrugated webs.

2 Literature study

Over 60 scholarly articles were reviewed to obtain the necessary information to commence the present study. Emphasis was placed on articles that focused on either conducting tests or analyzing previous test results regarding the shear failure of corrugated trapezoidal webs. From the reviewed literature, 164 tests were selected and compiled into a database, which will be presented in Chapter 4 and used to validate the accuracy of Eurocode equations.

2.1 Indication of different geometric parameters

Various types of geometries have been proposed by scientists in the literature for the design of corrugated webs, but trapezoidal, sinusoidal, and triangular have been selected more to be used in load-carrying structures [5].

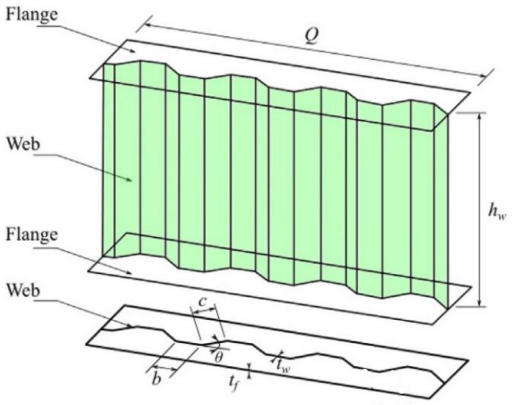

a) Trapezoidal corrugation. [5]

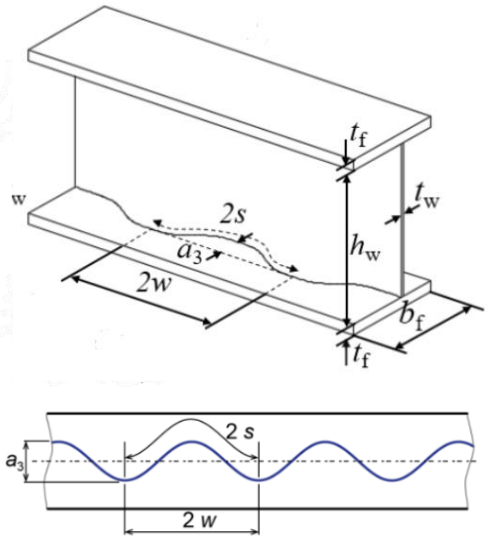

b) Sinusoidal corrugation. [6, 7]

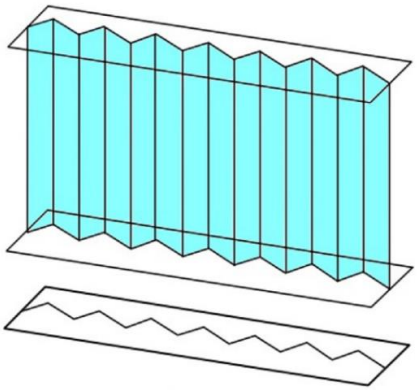

c) Triangular corrugation. [5]

Figure 2-1 Different shapes for corrugated webs. [5], [6] & [7]

2.2 Elastic buckling modes

Shear buckling of corrugated webs can occur in three different modes:

1) Local buckling
2) Global buckling
3) Interactive buckling

In the following discussion these three buckling modes are discussed.

2.2.1 Local buckling

Local buckling, illustrated in Figure 2.2, depends on the slenderness of a single fold. This phenomenon arises when a fold or flat sub-panel located between vertical edges has a high ratio between width and thickness. In such a case, the corrugated web behaves like an array of sub-panels made of flat plates, which are interdependent along their vertical sides and upheld by the flanges at their connected sides [8].

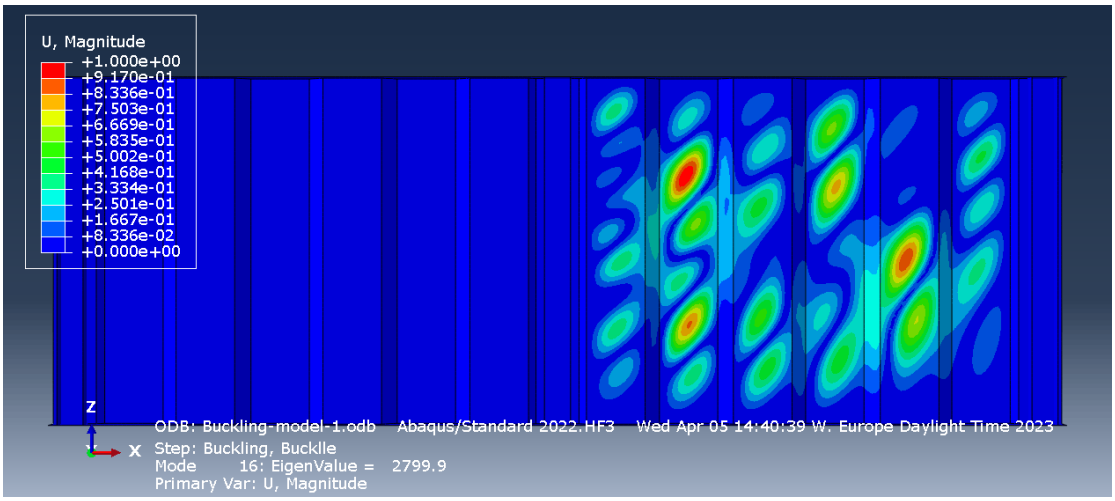

Figure 2-2 Local buckling mode, which is from analysis of model 10 mode 16, geometries are presented in Chapter 4.

2.2.2 Global buckling

The type of buckling referred to as "global" is recognized as a mode with several folds that are engaged in the deflected web panel and result in an inclined deflected area. Figure 2.3 indicates this buckling mode [9].

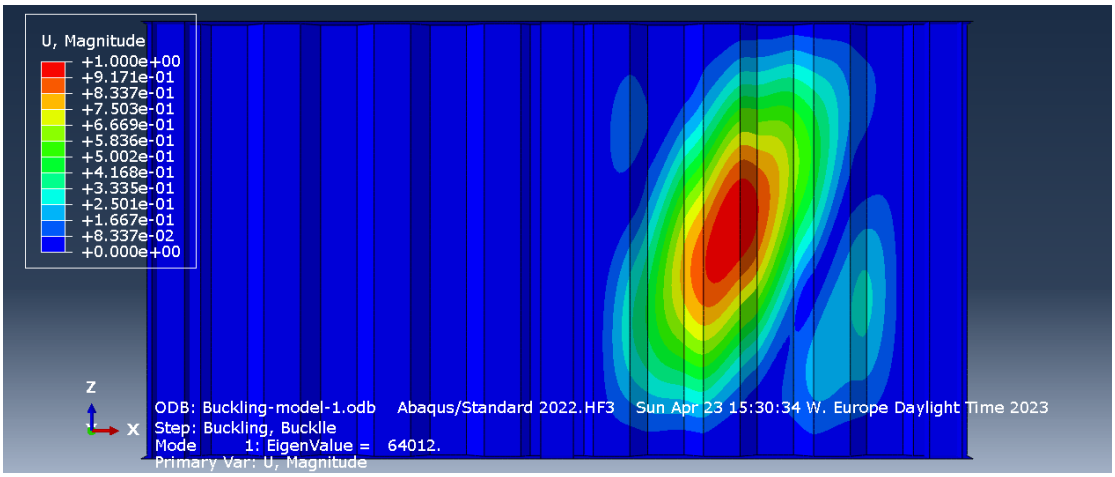

Figure 2-3 Local buckling mode, which is from analysis of model 2 mode 1, geometries are presented in Chapter 4.

2.2.3 Interactive buckling

In instances where buckling spreads across the sub-panels and exhibits features of both the local and global buckling modes, it is referred to as the interactive mode. [9] Figures 2.4 and 2.5, respectively, present a local and global interactive buckling mode. In this thesis, modes that are interactive and have more local characteristics are called local-

interactive, and those with more characteristics of global buckling are called global-interactive.

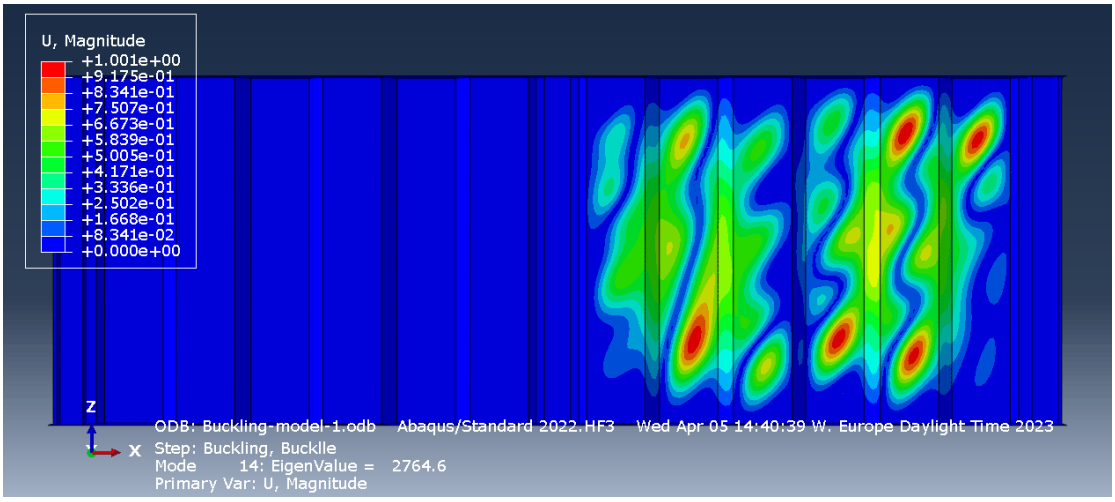

Figure 2-4 Local interactive buckling mode, which is from analysis of model 10 mode 14, geometries are presented in Chapter 4.

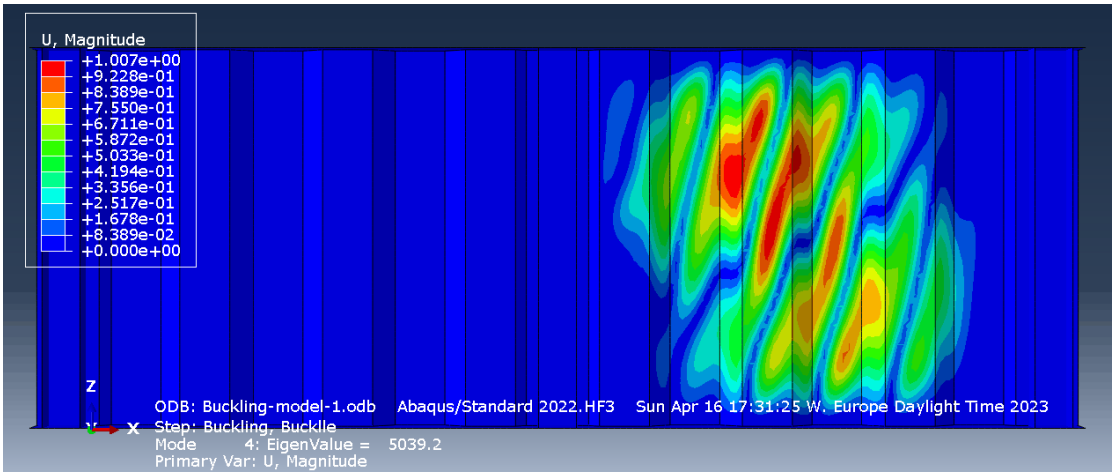

Figure 2-5 Global interactive buckling mode, which is from analysis of model 16 mode 4, geometries are presented in Chapter 4.

2.3 Review of Eurocode 3 and Commentary to Eurocode

To investigate the applicability of EN 1993-1-5 for the design of stainless steel girders with corrugated web in the subject of shear resistance, Eurocode 3 [2] and commentary to Eurocode [10] are reviewed. This revision will be the basis of the discussions in Chapter 4.

Figure 2.6 indicates the definition of notations in Eurocode. In the next chapters, different notations have been used but, the author has mentioned definitions there as well.

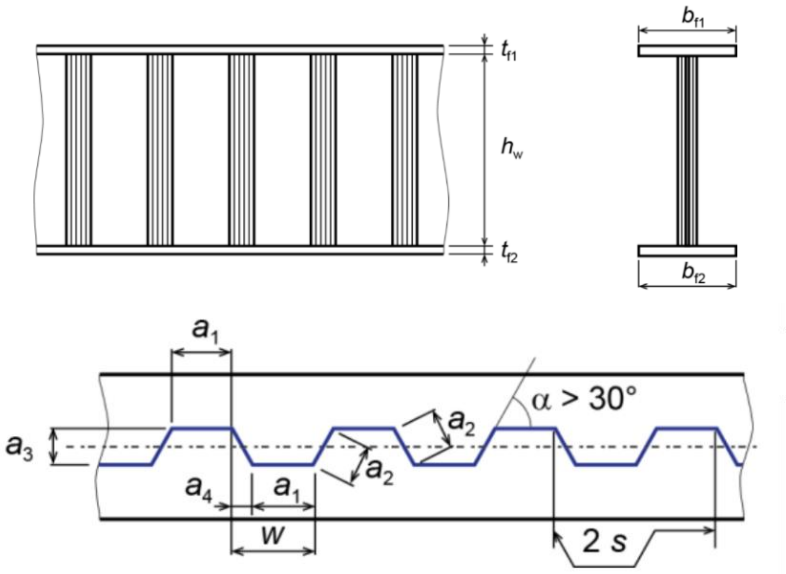

Figure 2-6 Indication of notations. [2]

2.3.1 Shear resistance

Shear resistance can be calculated from equation (2.1). [2]:

$$V_{bw,Rd} = \mathcal{X}_c \frac{f_{yw}}{\gamma_{M1}\sqrt{3}} h_w t_w \tag{2.1}$$

$\mathcal{X}_c$ is a reduction factor, and it can be calculated for both local and global buckling. The minimum value will be used in (2.1) equation. $\mathcal{X}_{c,l}$ is reduction factor for local buckling mode and $\mathcal{X}_{c,g}$ is reduction factor for global buckling mode. In Eurocode 3, interactive buckling mode is ignored, and only the global and local reduction factors are considered in the design shear resistance equation. From equations (2.2) and (2.5), local and global reduction factors can be calculated, and if, after calculation, the value is greater than 1, they need to be considered equal to 1.

$$\mathcal{X}_{c,l} = \frac{1.15}{0.9 + \lambda_{c,l}} \tag{2.2}$$

$$\lambda_{c,l} = \sqrt{\frac{f_{yw}}{\tau_{cr,l}\sqrt{3}}} \tag{2.3}$$

$$\tau_{cr,l} = 4.83\, E \left[\frac{t_w}{a_{max}}\right]^2 \tag{2.4}$$

$$\mathcal{X}_{c,g} = \frac{1.5}{0.5 + \lambda_{c,g}{}^2} \tag{2.5}$$

$$\lambda_{c,g} = \sqrt{\frac{f_{yw}}{\tau_{cr,g}\sqrt{3}}} \tag{2.6}$$

$$\tau_{cr,g} = \frac{32.4}{t_w {h_w}^2} \sqrt[4]{D_x {D_z}^3} \quad (2.7)$$

$$D_x = \frac{E {t_w}^2 w}{12(1-\nu^2)s} \quad (2.8)$$

$$D_z = \frac{EI_z}{w} \quad (2.9)$$

By using equations (2.2) to (2.9), reduction factors for both local and global modes can be calculated [2].
Equations (2.10) and (2.11) are used to calculate D_x and D_z.

$$D_x = \frac{E {t_w}^3}{12(1-\nu^2)} \left[\frac{a_1+a_4}{a_1+a_2}\right] \quad (2.10)$$

$$D_z = \frac{E t_w {a_3}^2}{12} \left[\frac{3a_1+a_2}{a_1+a_4}\right] \quad (2.11)$$

2.3.1.1 Review of commentary to Eurocode 1993-1-5

According to the commentary to EN 1993-1-5, the results of 69 collected tests, according to Table 2.1, are the basis for deriving the shear design equations in Eurocode. In Table 2.1, Eurocode equations are used to calculate V_{R1} and V_{R2}, V_{R1} is shear resistance that is calculated by corresponding reduction factor for local buckling and V_{R2} is shear resistance that is calculated by corresponding reduction factor for global buckling. V_u can be defined as measured shear resistance in a test. In order to compare reduction factors, χ_u is defined as the ratio of ultimate shear stress to yielding shear stress. $\frac{V_u}{V_{R1}} = \frac{\chi_u}{\chi_{c,l}}$ and $\frac{V_u}{V_{R2}} = \frac{\chi_u}{\chi_{c,g}}$, and the governing mode are specified in Table 2.1 by shading.

Table 2-1 Test results for 69 experiments, table is extracted from commentary on Eurocode. [10]

	Test		h_w	t_w	f_{yw}	α	a_1	a_3	V_u	χ_u	λ_1	λ_2	V_u/V_{R1}	V_u/V_{R2}
No	original	ref[9]	mm	mm	MPa		mm	mm	kN					
0	L1A	5	994	1,94	292	45	140	48	280	0,860	0,931	0,558	1,370	0,860
1	L1B	5	994	2,59	335	45	140	48	502	1,007	0,747	0,556	1,442	1,007
2	L2A	5	1445	1,94	282	45	140	50	337	0,737	0,915	0,774	1,164	0,737
3	L2B	5	1445	2,54	317	45	140	50	564	0,839	0,741	0,768	1,197	0,839
4	L3A	5	2005	2,01	280	45	140	48	450	0,690	0,880	1,092	1,068	0,778
5	L3B	5	2005	2,53	300	45	140	48	775	0,881	0,724	1,067	1,244	0,962
6	B1	10	600	2,1	341	45	140	50	208	0,837	0,929	0,347	1,332	0,837
7	B2	10	600	2,62	315	45	140	50	273	0,954	0,716	0,315	1,340	0,954
8	B3	10	600	2,62	317	45	140	50	246	0,854	0,718	0,316	1,202	0,854
9	B4b	10	600	2,11	364	45	140	50	217	0,815	0,956	0,358	1,315	0,815
10	M101	10	600	0,99	189	45	70	15	53	0,817	0,734	0,750	1,160	0,817
11	M102	10	800	0,99	190	45	70	15	79	0,908	0,736	1,003	1,292	0,912
12	M103	10	1000	0,95	213	45	70	15	84	0,718	0,812	1,342	1,069	1,101
13	M104	10	1200	0,99	189	45	70	15	101	0,778	0,734	1,501	1,106	1,428
14	L1	11	1000	2,1	410	30	106	50	380	0,764	0,772	0,616	1,110	0,764
15	L1	11	1000	3	450	30	106	50	610	0,782	0,566	0,590	0,996	0,782
16	L2	11	1498	2	376	30	106	50	600	0,921	0,776	0,894	1,343	0,921
17	L2	11	1498	3	402	30	106	50	905	0,867	0,535	0,836	1,081	0,867
18	1	12	850	2	355	33	102	56	275	0,788	0,731	0,459	1,118	0,788
19	2	12	850	2	349	38	91	56	265	0,773	0,642	0,466	1,036	0,773
20	V1/1	13	298	2,05	298	45	144	102	68	0,646	0,917	0,099	1,021	0,646
21	V1/2	13	298	2,1	283	45	144	102	70	0,684	0,872	0,096	1,054	0,684
22	V1/3	13	298	2	298	45	144	102	81	0,789	0,940	0,100	1,262	0,789
23	V2/3	13	600	3	279	45	144	102	235	0,810	0,606	0,175	1,060	0,810
24	CW3	8	440	3,26	284	45	250	45	171	0,726	0,976	0,218	1,184	0,726
25	CW4	8	440	2,97	222	45	250	45	154	0,918	0,947	0,198	1,475	0,918
26	CW5	8	440	2,97	222	45	250	63	141	0,841	0,947	0,156	1,350	0,841
27	I/5	14	1270	2	331	62	171	24	260	0,535	1,223	1,483	0,987	0,963
28	II/11	14	1270	2	225	62	171	24	220	0,666	0,974	1,267	1,085	0,935
29	121216A	15	305	0,64	676	45	38	25	50	0,656	1,165	0,583	1,177	0,656
30	121221A	15	305	0,63	665	55	42	33	46	0,623	1,298	0,501	1,190	0,623
31	121221B	15	305	0,78	665	55	42	33	73	0,798	1,048	0,475	1,352	0,798
32	121232A	15	305	0,64	665	63	50	51	41	0,546	1,741	0,391	1,255	0,546
33	121232B	15	305	0,78	641	63	50	51	61	0,692	1,403	0,365	1,386	0,692
34	121809A	15	305	0,71	572	50	20	14	63	0,880	0,509	0,829	1,078	0,880
35	121809C	15	305	0,63	669	50	20	14	55	0,740	0,620	0,924	0,978	0,740

36	121832B	15	305	0,92	562	63	50	51	53	0,581	1,113	0,328	1,018	0,581
37	122409A	15	305	0,71	586	50	20	14	58	0,791	0,515	0,839	0,973	0,791
38	122409C	15	305	0,66	621	50	20	14	58	0,803	0,570	0,880	1,026	0,803
39	122421A	15	305	0,68	621	55	42	33	43	0,578	1,162	0,475	1,036	0,578
40	122421B	15	305	0,78	638	55	42	33	61	0,695	1,027	0,466	1,165	0,695
41	122432B	15	305	0,78	634	63	50	51	49	0,562	1,395	0,363	1,122	0,562
42	181209A	15	457	0,56	689	50	20	14	81	0,795	0,708	1,446	1,111	1,373
43	181209C	15	457	0,61	592	50	20	14	89	0,933	0,602	1,312	1,219	1,382
44	181216C	15	457	0,76	679	45	38	25	119	0,873	0,984	0,839	1,430	0,873
45	181221A	15	457	0,61	578	55	42	33	62	0,666	1,250	0,706	1,244	0,666
46	181221B	15	457	0,76	606	55	42	33	98	0,806	1,027	0,684	1,350	0,806
47	181232A	15	457	0,6	552	63	50	51	52	0,594	1,692	0,542	1,340	0,594
48	181232B	15	457	0,75	602	63	50	51	80	0,671	1,414	0,535	1,349	0,671
49	181809A	15	457	0,61	618	50	20	14	82	0,823	0,615	1,341	1,085	1,262
50	181809C	15	457	0,62	559	50	20	14	78	0,852	0,576	1,270	1,093	1,200
51	181816A	15	457	0,63	592	45	38	25	75	0,761	1,108	0,821	1,329	0,761
52	181816C	15	457	0,74	614	45	38	25	96	0,800	0,961	0,803	1,294	0,800
53	181821A	15	457	0,63	552	55	42	33	56	0,610	1,182	0,684	1,104	0,610
54	181821B	15	457	0,74	596	55	42	33	93	0,798	1,046	0,683	1,351	0,798
55	181832A	15	457	0,61	689	63	50	51	53	0,477	1,859	0,603	1,145	0,477
56	181832B	15	457	0,75	580	63	50	51	79	0,687	1,388	0,525	1,368	0,687
57	241209A	15	610	0,62	606	50	20	14	71	0,536	0,599	1,765	0,699	1,292
58	241209C	15	610	0,63	621	50	20	14	79	0,573	0,597	1,780	0,746	1,400
59	241216A	15	610	0,63	592	45	38	25	76	0,578	1,108	1,096	1,009	0,656
60	241216B	15	610	0,79	587	45	38	25	133	0,813	0,880	1,032	1,259	0,848
61	241221A	15	610	0,61	610	55	42	33	77	0,587	1,284	0,968	1,114	0,587
62	241221B	15	610	0,76	639	55	42	33	127	0,742	1,055	0,938	1,261	0,742
63	241232A	15	610	0,62	673	63	50	51	69	0,469	1,808	0,792	1,104	0,469
64	241232B	15	610	0,76	584	63	50	51	101	0,645	1,374	0,701	1,276	0,645
65	Gauche	16	460	2	254	30,5	0	126	139	1,029	1,494	0,121	2,142	1,029
66	Droit	16	550	2	254	30,5	0	126	109	0,675	1,494	0,145	1,405	0,675
67	Sin 1	17	1502	2,1	225	2w=155		40	370	0,902	0,433	1,108	1,046	1,038
68	Sin 2	17	1501	2,1	225	2w=155		40	365	0,890	0,433	1,108	1,032	1,025
69	Sin 3	17	1505	2,1	225	2w=155		40	353	0,859	0,433	1,108	0,996	0,989

In Figures 2.7 and 2.8, data from Table 2.1 is compared with the calculated reduction factor by Eurocode's equations, and these figures show that the calculated reduction factor by Eurocode's equations has a good estimation of the lower boundary and is conservative. The minimum and maximum local slenderness ratios in Figure 2.7, respectively, are 0.509 and 1.859, and the minimum and maximum global slenderness ratios in Figure 2.8, respectively, are 1.108 and 1.78.

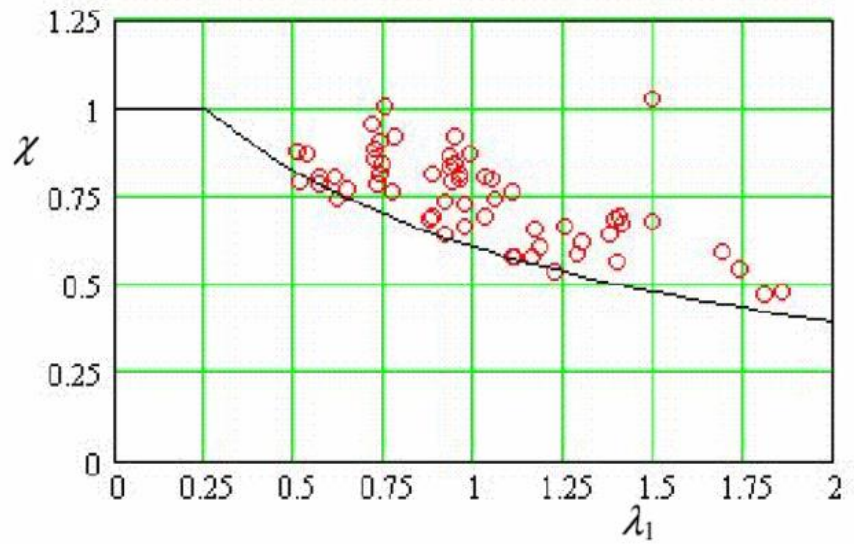

Figure 2-7 Vertical axis presents reduction factor for local buckling mode and horizontal axis indicates corresponding local slenderness ratio. [10]

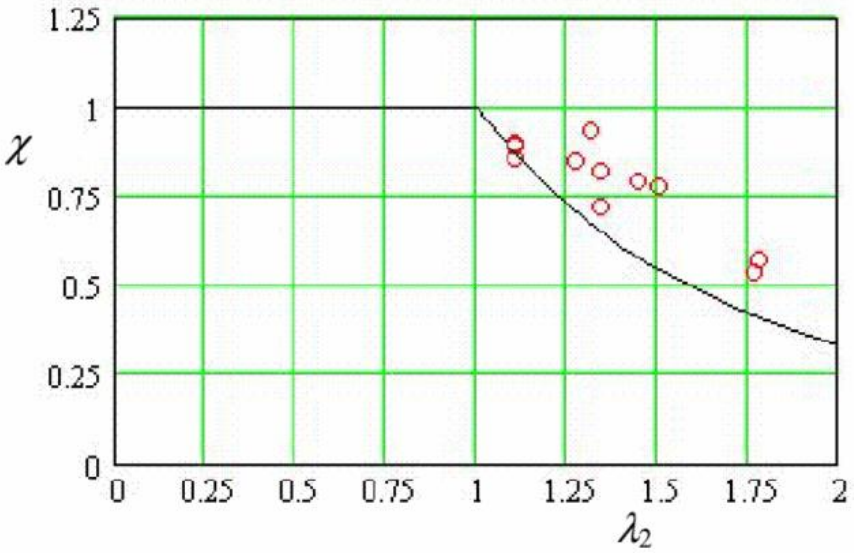

Figure 2-8 Vertical axis presents reduction factor for global buckling mode and horizontal axis indicates corresponding global slenderness ratio. [10]

2.4 Database generated by literature review

Earlier in Chapter 1, it was mentioned that a database of 164 shear tests is collected by the author in literature review stage, ref. Table 2.2.

Table 2-2 Database of all the collected experimental that the author has collected during literature study.

No.	Name	a	b	d	θ	h_w	t_w	λ_l	λ_g	f_{yw}	χ_u	Reference number
1	SP-1	100	80.0	60.0	36.9	381.0	1.9	0.78	0.22	225	0.77	[11]
2	SP-2	100	80.0	60.0	36.9	418.0	1.9	0.76	0.24	205	0.83	[11]

3	SP-3	100	80.0	60.0	36.9	419.0	3.0	0.52	0.23	234	0.82	[11]
4	CWB1	170	80.0	80.0	45.0	351.0	4.0	0.61	0.13	205	0.92	[12]
5	CWB2	170	80.0	80.0	45.0	351.0	4.0	0.61	0.13	205	0.86	[12]
6	UCW1	130	70.0	70.0	45.0	380.0	2.4	0.69	0.15	159	1.04	[12]
7	UCW2	130	70.0	70.0	45.0	380.0	2.1	0.78	0.16	159	1.05	[12]
8	UCW5	130	70.0	70.0	45.0	380.0	2.1	0.78	0.16	159	0.93	[12]
9	UCW6	130	70.0	70.0	45.0	380.0	1.9	0.87	0.16	159	1.11	[12]
10	TS 600-3	170	80.0	80.0	45.0	600.0	3.0	0.82	0.23	205	0.77	[12]
11	TS 800-2	170	80.0	80.0	45.0	800.0	2.0	1.22	0.34	205	0.52	[12]
12	TS 1300-2	170	80.0	80.0	45.0	1300.0	2.0	1.08	0.49	159	0.67	[12]
13	TS 1300-3	170	80.0	80.0	45.0	1300.0	3.0	0.72	0.45	159	1.05	[12]
14	TS 800-8	170	80.0	80.0	45.0	800.0	8.0	0.31	0.24	205	1.14	[12]
15	L1	450	300.0	200.0	33.7	1500.0	4.8	1.12	0.22	144	0.72	[13]
16	L2	550	300.0	188.8	32.2	1500.0	4.8	1.37	0.23	144	0.60	[13]
17	L3	450	300.0	49.6	9.4	1500.0	4.8	1.12	0.64	144	0.51	[13]
18	L4	550	300.0	55.9	10.6	1500.0	4.8	1.37	0.57	144	0.46	[13]
19	G2	160	50.0	33.0	33.4	2000.0	3.8	0.50	1.16	144	0.83	[13]
20	G3	160	100.0	26.9	15.1	2000.0	3.8	0.50	1.41	144	0.85	[13]
21	I1	320	100.0	44.6	24.0	2000.0	4.8	0.80	0.87	144	0.95	[13]
22	I2	350	100.0	28.6	16.0	2000.0	3.8	1.10	1.28	144	0.52	[13]
23	G1	200	180.0	45.4	14.2	2000.0	4.8	0.50	0.93	144	0.79	[13]
24	S1-2	20	16.0	12.0	37.0	460.0	0.9	0.33	1.09	223	0.73	[14]
25	S1-3	20	16.0	12.0	37.0	660.0	0.9	0.33	1.56	223	0.61	[14]
26	S1-4	20	16.0	12.0	37.0	760.0	0.9	0.33	1.80	223	0.52	[14]
27	S1-5	20	16.0	12.0	37.0	860.0	0.9	0.33	2.03	223	0.48	[14]
28	S2-1	80	64.0	48.0	37.0	260.0	0.9	1.33	0.22	223	0.48	[14]
29	S2-2	80	64.0	48.0	37.0	360.0	0.9	1.33	0.30	223	0.55	[14]
30	S2-3	80	64.0	48.0	37.0	460.0	0.9	1.33	0.38	223	0.74	[14]
31	MI2	250	220.0	60.0	15.3	2000.0	4.0	0.81	0.86	171	0.64	[15]
32	MI3	220	180.0	60.0	18.4	2000.0	4.0	0.71	0.85	171	0.62	[15]
33	MI4	220	180.0	75.0	22.6	2000.0	4.0	0.71	0.72	171	0.77	[15]
34	A12-305-30	40	34.6	20.0	30.0	305.0	1.2	0.39	0.36	133	1.02	[16]
35	A12-305-45	40	28.3	28.3	45.0	305.0	1.2	0.39	0.27	133	1.11	[16]
36	A12-410-30	40	34.6	20.0	30.0	410.0	1.2	0.39	0.49	133	1.01	[16]
37	A12-410-45	40	28.3	28.3	45.0	410.0	1.2	0.39	0.37	133	1.13	[16]
38	A12-505-30	40	34.6	20.0	30.0	505.0	1.2	0.39	0.60	133	0.89	[16]
39	A12-505-45	40	28.3	28.3	45.0	505.0	1.2	0.39	0.45	133	1.11	[16]
40	B12-305-30	40	34.6	20.0	30.0	305.0	1.2	0.39	0.36	133	1.10	[16]
41	B12-305-45	40	28.3	28.3	45.0	305.0	1.2	0.39	0.27	133	1.07	[16]
42	B12-410-30	40	34.6	20.0	30.0	410.0	1.2	0.39	0.49	133	1.01	[16]
43	B12-410-45	40	28.3	28.3	45.0	410.0	1.2	0.39	0.37	133	1.12	[16]
44	B12-505-30	40	34.6	20.0	30.0	505.0	1.2	0.39	0.60	133	1.01	[16]
45	B12-505-45	40	28.3	28.3	45.0	505.0	1.2	0.39	0.45	133	1.09	[16]
46	A20-410-30-N	40	34.6	20.0	30.0	410.0	2.0	0.26	0.48	167	0.91	[16]
47	A20-410-45-N	40	28.3	28.3	45.0	410.0	2.0	0.26	0.36	167	0.85	[16]
48	A20-505-30-N	40	34.6	20.0	30.0	505.0	2.0	0.26	0.59	167	0.91	[16]
49	A20-505-45-N	40	28.3	28.3	45.0	505.0	2.0	0.26	0.45	167	0.90	[16]
50	B20-505-45-N	40	28.3	28.3	45.0	505.0	2.0	0.26	0.45	167	0.89	[16]
51	TP20-300-30	60	34.6	20.0	30.0	305.0	2.0	0.39	0.35	167	0.83	[16]
52	B20-305-30	40	34.6	20.0	30.0	305.0	2.0	0.40	0.55	393	0.97	[16]
53	B20-305-45	40	28.3	28.3	45.0	305.0	2.0	0.40	0.41	393	1.05	[16]
54	B20-505-45	40	28.3	28.3	45.0	505.0	2.0	0.40	0.68	393	0.83	[16]
55	CG240-2	76.3	73.7	20.0	15.2	799.5	3.2	0.31	0.84	174	0.87	[16]
56	CG240-4	80.3	69.7	40.0	29.9	798.8	3.3	0.32	0.49	174	0.95	[16]
57	CG240-6	87	63.0	60.0	43.6	799.4	3.2	0.35	0.36	174	0.99	[16]
58	G7A	300	200.0	150.0	36.9	1500.0	6.0	0.83	0.37	269	0.90	[17]
59	G8A	300	200.0	150.0	36.9	1500.0	6.0	0.83	0.36	268	0.85	[17]
60	SC1	300	200.0	150.0	36.9	1500.0	6.3	0.78	0.35	268	0.80	[18]
61	SP2-8-800 1	170	80.0	80.0	45.0	800.0	8.0	0.26	0.21	156	1.31	[17]
62	SP2-8-800 2	170	80.0	80.0	45.0	800.0	8.0	0.26	0.21	156	1.38	[17]
63	V-PILOTA	38.1	25.4	25.4	45.0	304.8	0.8	0.91	0.53	358	0.97	[17]
64	V-PILOTB	38.1	25.4	25.4	45.0	304.8	0.8	0.92	0.53	368	0.81	[17]
65	V121216A	38.1	25.4	25.4	45.0	304.8	0.6	1.17	0.58	390	0.66	[17]
66	V121216B	38.1	25.4	25.4	45.0	304.8	0.8	0.97	0.55	384	0.98	[17]

67	V181216B	38.1	25.4	25.4	45.0	457.2	0.6	1.17	0.84	357	0.94	[17]
68	V181216C	38.1	25.4	25.4	45.0	457.2	0.8	0.99	0.83	392	0.88	[17]
69	V181816A	38.1	25.4	25.4	45.0	457.2	0.6	1.10	0.81	342	0.75	[17]
70	V181816B	38.1	25.4	25.4	45.0	457.2	0.7	0.97	0.79	354	0.81	[17]
71	V241216A	38.1	25.4	25.4	45.0	609.6	0.6	1.10	1.08	342	0.57	[17]
72	V241216B	38.1	25.4	25.4	45.0	609.6	0.8	0.88	1.02	339	0.82	[17]
73	V121221A	41.9	23.4	33.3	55.0	304.8	0.6	1.29	0.46	384	0.63	[17]
74	V121221B	41.9	23.4	33.3	55.0	304.8	0.8	1.04	0.44	384	0.79	[17]
75	V122421A	41.9	23.4	33.3	55.0	304.8	0.7	1.17	0.44	358	0.59	[17]
76	V122421B	41.9	23.4	33.3	55.0	304.8	0.8	1.02	0.43	368	0.70	[17]
77	V181221A	41.9	23.4	33.3	55.0	457.2	0.6	1.25	0.65	334	0.67	[17]
78	V181221B	41.9	23.4	33.3	55.0	457.2	0.8	1.02	0.63	350	0.80	[17]
79	V181821A	41.9	23.4	33.3	55.0	457.2	0.6	1.17	0.63	318	0.61	[17]
80	V181821B	41.9	23.4	33.3	55.0	457.2	0.7	1.05	0.63	344	0.81	[17]
81	V241221A	41.9	23.4	33.3	55.0	609.6	0.6	1.28	0.89	352	0.59	[17]
82	V241221B	41.9	23.4	33.3	55.0	609.6	0.8	1.05	0.86	369	0.74	[17]
83	V121232A	49.8	26.4	50.8	62.5	304.8	0.6	1.74	0.33	384	0.55	[17]
84	V121232B	49.8	26.4	50.8	62.5	304.8	0.8	1.40	0.31	370	0.70	[17]
85	V121832A	49.8	26.4	50.8	62.5	304.8	0.6	1.79	0.34	406	0.44	[17]
86	V121832B	49.8	26.4	50.8	62.5	304.8	0.9	1.11	0.28	324	0.59	[17]
87	V122432A	49.8	26.4	50.8	62.5	304.8	0.6	1.80	0.34	412	0.39	[17]
88	V122432B	49.8	26.4	50.8	62.5	304.8	0.8	1.40	0.31	366	0.56	[17]
89	V181232A	49.8	26.4	50.8	62.5	457.2	0.6	1.70	0.46	318	0.59	[17]
90	V181232B	49.8	26.4	50.8	62.5	457.2	0.7	1.42	0.45	348	0.67	[17]
91	V181832A	49.8	26.4	50.8	62.5	457.2	0.6	1.86	0.51	398	0.48	[17]
92	V181832B	49.8	26.4	50.8	62.5	457.2	0.7	1.39	0.45	335	0.69	[17]
93	V241232A	49.8	26.4	50.8	62.5	609.6	0.6	1.80	0.67	389	0.47	[17]
94	V241232B	49.8	26.4	50.8	62.5	609.6	0.8	1.37	0.59	337	0.65	[17]
95	V121809A	19.8	11.9	14.2	50.0	304.8	0.7	0.51	0.79	330	0.89	[17]
96	V121809C	19.8	11.9	14.2	50.0	304.8	0.6	0.61	0.88	386	0.74	[17]
97	V122409A	19.8	11.9	14.2	50.0	304.8	0.7	0.51	0.80	338	0.79	[17]
98	V122409C	19.8	11.9	14.2	50.0	304.8	0.7	0.56	0.84	358	0.80	[17]
99	V181209A	19.8	11.9	14.2	50.0	457.2	0.6	0.70	1.38	398	0.80	[17]
100	V181209C	19.8	11.9	14.2	50.0	457.2	0.6	0.60	1.25	342	0.93	[17]
101	V181809A	19.8	11.9	14.2	50.0	457.2	0.6	0.61	1.28	357	0.83	[17]
102	V181809C	19.8	11.9	14.2	50.0	457.2	0.6	0.57	1.21	323	0.85	[17]
103	V241209A	19.8	11.9	14.2	50.0	609.6	0.6	0.59	1.68	350	0.53	[17]
104	V241209C	19.8	11.9	14.2	50.0	609.6	0.6	0.59	1.69	358	0.57	[17]
105	L1A	140	50.0	50.0	45.0	994.0	1.9	0.93	0.54	169	0.86	[17]
106	L1B	140	50.0	50.0	45.0	994.0	2.6	0.75	0.54	193	1.01	[17]
107	L2A	140	50.0	50.0	45.0	1445.0	1.9	0.91	0.77	163	0.74	[17]
108	L2B	140	50.0	50.0	45.0	1445.0	2.5	0.74	0.77	183	0.84	[17]
109	L3A	140	50.0	50.0	45.0	2005.0	2.0	0.88	1.06	162	0.69	[17]
110	L3B	140	50.0	50.0	45.0	2005.0	2.5	0.72	1.04	173	0.88	[17]
111	B1	140	50.0	50.0	45.0	600.0	2.1	0.93	0.35	197	0.84	[17]
112	B4	140	50.0	50.0	45.0	600.0	2.1	0.95	0.36	210	0.69	[17]
113	B4b	140	50.0	50.0	45.0	600.0	2.1	0.95	0.36	210	0.82	[17]
114	B3	140	50.0	50.0	45.0	600.0	2.6	0.72	0.32	183	0.86	[17]
115	B2	140	50.0	50.0	45.0	600.0	2.6	0.72	0.32	182	1.00	[17]
116	M101	70	15.0	15.0	45.0	600.0	1.0	0.73	0.75	109	0.82	[17]
117	M102	70	15.0	15.0	45.0	800.0	1.0	0.74	1.00	110	0.91	[17]
117	M103	70	15.0	15.0	45.0	1000.0	1.0	0.81	1.34	123	0.72	[17]
119	M104	70	15.0	15.0	45.0	1200.0	1.0	0.73	1.50	109	0.80	[17]
120	L1-2.1	106	86.6	50.0	30.0	1000.0	2.1	0.77	0.67	237	0.76	[17]
121	L1-3	106	86.6	50.0	30.0	1000.0	3.0	0.57	0.64	260	0.78	[17]
122	L2-2	106	86.6	50.0	30.0	1498.0	2.0	0.78	0.98	217	0.92	[17]
123	L2-3	106	86.6	50.0	30.0	1498.0	3.0	0.53	0.91	232	0.87	[17]
124	No. 1	102	85.5	55.5	33.0	850.0	2.0	0.73	0.50	205	0.79	[17]
125	No. 2	91	71.5	56.3	38.2	850.0	2.0	0.64	0.49	201	0.77	[17]
126	V1/1	144	102.0	102.0	45.0	298.0	2.1	0.92	0.10	172	0.65	[17]
127	V1/2	144	102.0	102.0	45.0	298.0	2.1	0.87	0.10	163	0.69	[17]
128	V1/3	144	102.0	102.0	45.0	298.0	2.0	0.94	0.10	172	0.79	[17]
129	V2/3	144	102.0	102.0	45.0	600.0	3.0	0.61	0.18	161	0.81	[17]
130	SP1	146	104.0	104.0	45.0	800.0	2.0	0.97	0.27	177	0.80	[17]

131	SP2	170	80.0	80.0	45.0	800.0	2.0	1.11	0.31	172	0.78	[17]
132	SP3	185	65.0	65.0	45.0	800.0	2.0	1.19	0.35	168	0.78	[17]
133	SP4	117	83.0	83.0	45.0	800.0	2.0	0.76	0.31	172	0.84	[17]
134	SP5	136	64.0	64.0	45.0	800.0	2.0	0.88	0.36	168	0.82	[17]
135	SP6	148	52.0	52.0	45.0	800.0	2.0	0.96	0.42	169	0.81	[17]
136	SP2-2-400 1	170	80.0	80.0	45.0	400.0	2.0	1.04	0.15	152	0.66	[17]
137	SP2-2-400 2	170	80.0	80.0	45.0	400.0	2.0	1.04	0.15	152	0.73	[17]
138	SP2-2-800 1	170	80.0	80.0	45.0	800.0	2.0	1.06	0.30	157	0.71	[17]
139	SP2-2-800 2	170	80.0	80.0	45.0	800.0	2.0	1.06	0.30	157	0.71	[17]
140	SP2-3-600 1	170	80.0	80.0	45.0	600.0	3.0	0.73	0.21	170	0.99	[17]
141	SP2-3-600 2	170	80.0	80.0	45.0	600.0	3.0	0.73	0.21	170	1.01	[17]
142	SP2-3-1200 1	170	80.0	80.0	45.0	1200.0	3.0	0.73	0.42	170	1.00	[17]
143	SP2-3-1200 2	170	80.0	80.0	45.0	1200.0	3.0	0.73	0.42	170	1.02	[17]
144	SP2-4-800 1	170	80.0	80.0	45.0	800.0	4.0	0.58	0.27	188	1.00	[17]
145	SP2-4-800 2	170	80.0	80.0	45.0	800.0	4.0	0.58	0.27	188	1.00	[17]
146	SP2-4-1600 1	170	80.0	80.0	45.0	1600.0	4.0	0.58	0.55	189	1.00	[17]
147	SP2-4-1600 2	170	80.0	80.0	45.0	1600.0	4.0	0.58	0.55	189	1.01	[17]
148	V1b	30	47.0	40.0	40.4	500.0	2.5	0.31	0.32	156	1.00	[19]
149	3PCW350	350	100.0	100.0	45.0	384.0	2.8	1.70	0.12	188	0.52	[19]
150	4PCW275	275	100.0	100.0	45.0	384.0	3.0	1.31	0.12	206	0.62	[19]
151	3PCW200	200	100.0	100.0	45.0	384.0	2.8	0.97	0.12	188	0.58	[19]
152	CW1	180	45.0	45.0	45.0	440.4	3.1	0.79	0.24	185	0.83	[19]
153	CW2	180	45.0	45.0	45.0	437.9	3.3	0.73	0.23	180	0.87	[19]
154	CW3	250	45.0	45.0	45.0	437.2	3.3	0.98	0.22	164	0.72	[19]
155	S1	430	370.0	220.0	30.7	1500.0	8.0	0.83	0.24	233	0.82	[20]
156	S2	480	420.0	240.0	29.7	1500.0	8.0	0.96	0.23	252	0.79	[20]
157	S3	480	420.0	240.0	29.7	1500.0	8.0	0.92	0.22	230	0.84	[20]
158	L-1	60	30.0	30.0	45.0	400.0	1.0	0.72	0.36	138	0.80	[21]
159	G-2	30	10.0	10.0	45.0	400.0	2.0	0.22	0.81	202	0.90	[21]
160	TS 400-2	170	80.0	80.0	45.0	400.0	2.0	1.22	0.17	205	0.81	[22]
161	CW4	250	45.0	45.0	45.0	440.0	3.0	0.95	0.20	128	0.92	[22]
162	CW5	250	63.0	63.0	45.0	440.0	3.0	0.95	0.16	128	0.84	[22]
163	I/5	171	12.8	24.0	61.9	1270.0	2.0	1.17	1.20	191	0.54	[22]
164	II/11	171	12.8	24.0	61.9	1270.0	2.0	0.96	0.99	129	0.67	[22]

3 Verification of FEM method

Two previously conducted experimental tests are selected to be simulated by ABAQUS software in order to verify the finite element modeling procedure. The first experimental study was conducted by Jiho Moon, Jongwon Yi, Byung H.Choi and Hak-Eun Lee in July 2008, and the specimen is labeled MI2. [15] The second experimental study was conducted by Mozhdeh Amani, Mohammad Al-Emrani, and Mathias Flansbje in September 2022, and the specimen is labeled 1001 [23].

3.1 Simulation of specimen MI2

The main reason for the selection of the specimen MI2 in the current FEM verification study was the availability of needed data about the initial imperfections in the relevant literature. This allowed for a better understanding of the impact of imperfections on the shear failure behavior, particularly with respect to the magnitude of the maximum imperfection observed in the specimen.

3.1.1 FE Modelling of MI2 specimen

The geometrical properties of MI2 have been chosen according to the dimensions mentioned in the article, and the fabrication errors have been neglected. The detailed geometry is presented in Table 3.1, and Figure 3.1 shows the definition of each symbol. In table 3.1, h_w is web height, t_w is web thickness, b_f is flange width, t_f is thickness of flange, and L is length of span, which is distance between supports.

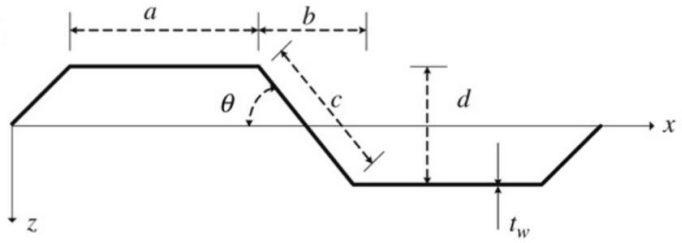

Figure 3-1 Geometrical parameters of the corrugated web [15]

Table 3-1 Profile of the test specimen, MI2 (all the dimensions are in mm).

Label	a	b	d	h_w	t_w	b_f	t_f	L
MI2	250	220	60	2000	4	300	30	5820

In the middle of the beam, a flat web panel is used with a higher thickness than the corrugated web. Two vertical stiffeners are attached to the ends of this flat web panel. In addition, two more stiffeners are attached to the web at the support locations to avoid any failure under point loads during testing. It can be mentioned that the width and

thickness of the flat web are 400 mm and 15 mm, respectively. The thickness of the stiffeners is 25 mm. the test setup is one-point loading, so in the model, load is distributed on one of the middle stiffeners. The reason behind this is to control the location of the shear buckling. The beam is simply supported, and in the middle, stiffeners are set to resist against lateral movements. Figure 3.2 shows the location of stiffeners, the flat web panel, the applied load, and end supports in the FE model of MI2.

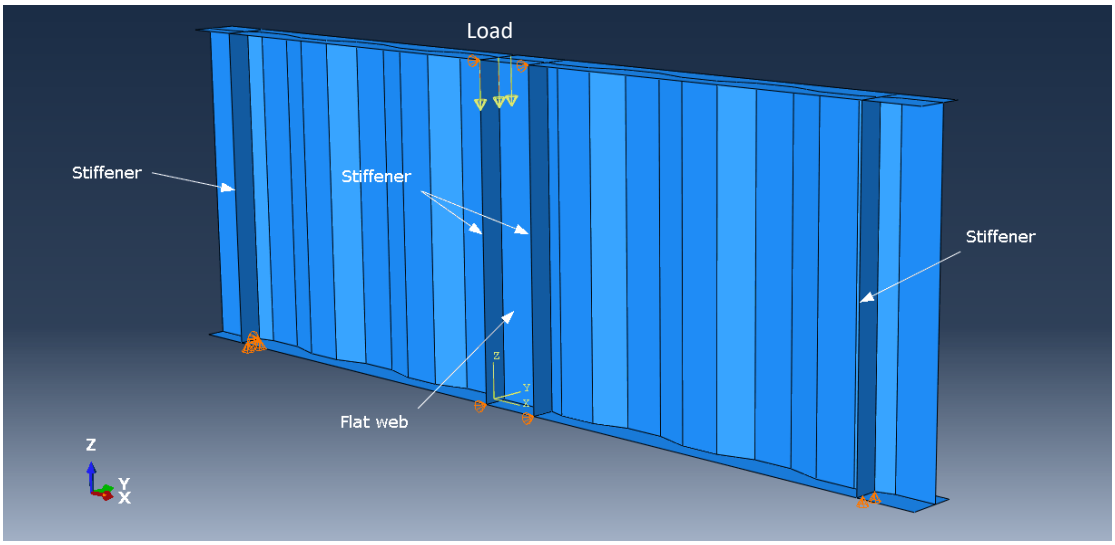

Figure 3-2 Configuration of MI2 in Abaqus.

The only information given regarding the material properties of tested specimens in the article is the yield stress of the corrugated web, which is 296 MPa. Other properties like modulus of elasticity and Poisson's ratio have been selected directly according to Table 3.2, which is estimated from a published database. The ultimate tensile stress and ultimate tensile strain have been estimated by considering Figure 3.3.

Table 3-2 Mechanical properties of carbon steel database published in 2017.[24]

Temp. (°C)	Grade A				
	E (GPa)	σ_Y (MPa)	σ_T (MPa)	ε_F	ν
20	199.6	299.3	464.9	0.423	0.3
	196.1	298.9	464.6	0.427	0.3
	186.3	300.8	462.4	0.426	0.3
Mean	194.0	299.6	463.9	0.425	0.3
-20	212.2	310.7	485.5	0.425	0.3
	208.6	323.8	512.6	0.439	0.3
	206.5	326.3	506.4	0.410	0.3
Mean	209.1	320.3	501.5	0.424	0.3
-60	181.2	345.0	512.5	0.458	0.3
	173.8	349.6	514.2	0.436	0.3
	189.8	345.4	509.2	0.448	0.3
Mean	181.6	346.7	512.0	0.447	0.3

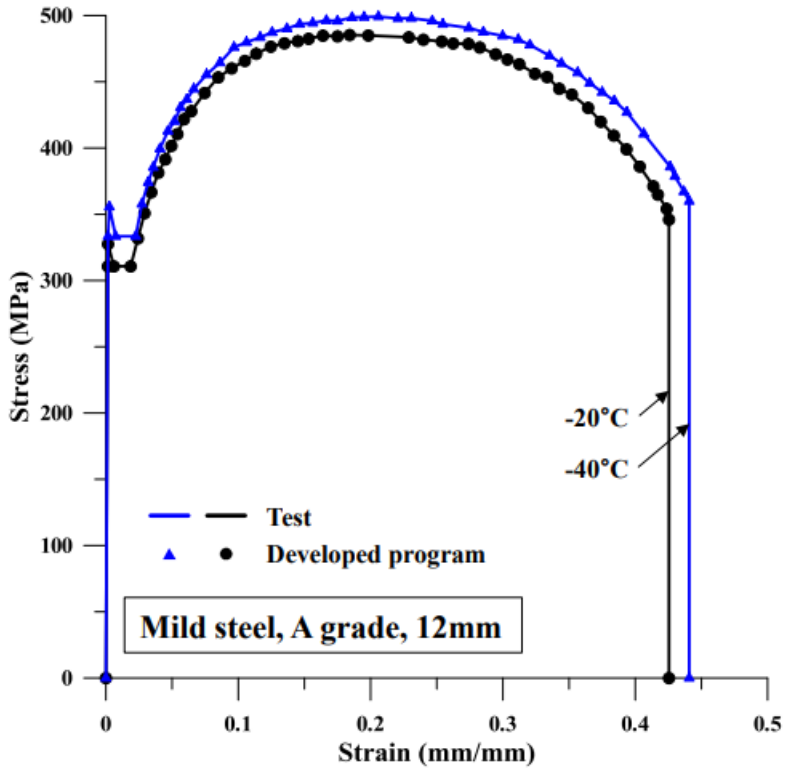

Figure 3-3 Stress strain diagram for mild steel [24]

The selected material properties for the MI2 FE modeling are described in Table 3.3:

Table 3-3 Mechanical properties of the MI2 FE model.

E(MPa)	σ_y(MPa)	σ_T(MPa) Engineering ultimate tensile stress	σ_{TT}(MPa) True ultimate tensile stress	ε_T Engineering ultimate tensile strain	ε_{TT} True ultimate tensile strain	ν
196000	296	486	575	0.1846	0.1664	0.3

The S4R shell element is used in this analysis. A convergence study on the first mode of buckling has been done in order to select a suitable mesh size. A percentage difference for each mesh size is calculated in comparison with the Eigenvalue for one grade of finer mesh. Table 3.4 and Figure 3.4 present the results of the convergence study, and based on them, a mesh size of 25 mm is chosen.

Table 3-4 The first buckling mode eigenvalues for different mesh sizes.

Mesh size	Eigenvalue	Error (%)
100	10526	
75	9235	13.9
50	8403	9.9
25	7935	5.8
18	7872	0.8
12	7829	0.5

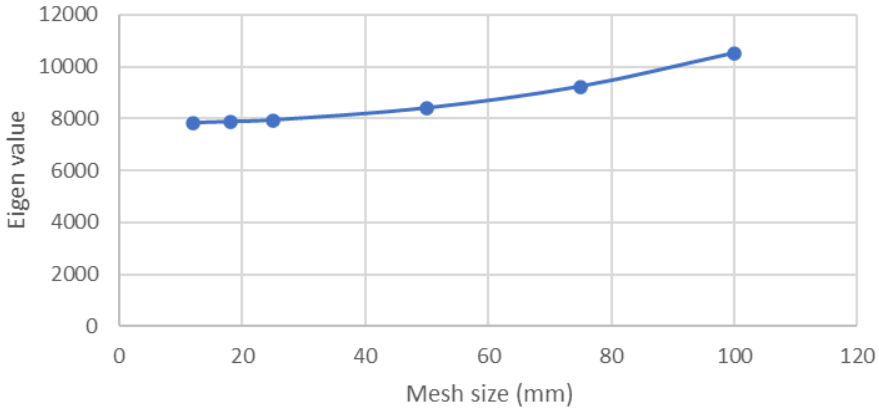

Figure 3-4 Diagram of corresponding eigenvalues for different mesh sizes on the eigenvalue.

In the main reference, the initial imperfection for one side of the beam has been measured, and the results are shown in Figure 3.5. In a search among the eigen modes, it was found that the 28th buckling mode of the MI2 specimen, as shown in Figure 3.6, is nearest to the pattern of the measured initial imperfections since the location of the maximum imperfection is near the right side of the upper flange. In the main reference, it was mentioned that the maximum amplitude of the imperfection is 17.9 mm. However, in the current study, this amplitude is not applied in the verification study since it includes not only the out-of-plane deflections of the web but also the production errors and out-of-straightness deflections of the entire beam. Also, it is mentioned in the main reference that there was a relatively huge production error in the depth of the corrugation (d), which definitely affects the magnitude of the out-of-plane deflection of the web. Therefore, based on an estimation of the production and out-of-straightness errors by taking the average value of imperfection as 11.65 mm, the relative out-of-plane deflection of the web panel in the FE validation study is estimated to be in the range of 5-7 mm.

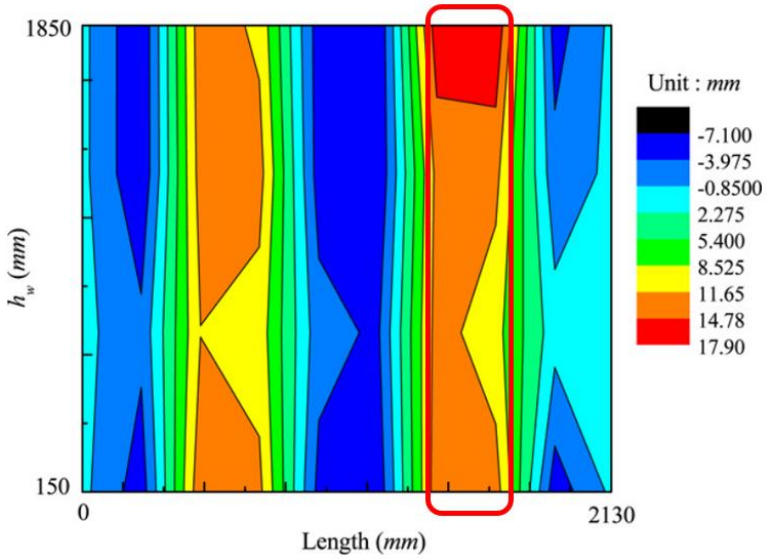

Figure 3-5 The measured initial imperfection contour of the test specimen (MI2) [15]

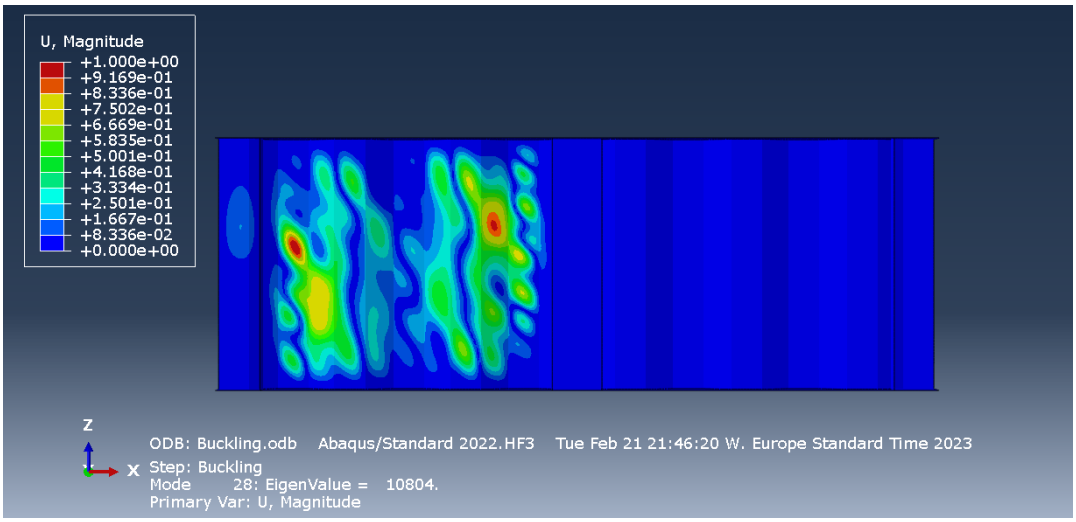

Figure 3-6 The 28th buckling mode of the FE model MI2.

3.1.2 Verification results for MI2

Table 3.5 shows the results of both the experimental test and the nonlinear FE analysis in the current study. It should be mentioned that buckling mode 28 with a maximum amplitude of 5mm is used as the initial imperfection.

Table 3-5 Results of experimental test and analysis by Abaqus.

Maximum shear stress in the test (MPa)	Maximum shear stress in FEM (MPa)	Percentage difference (%)	The maximum vertical displacement in the test (mm)	The maximum vertical displacement in FEM (mm)	Percentage difference (%)
109.19	109.62	0.39	6.8	5.7	16

It is observed that the difference between the ultimate shear capacity of the tested beam and the FEM is negligible. However, the difference between the ultimate vertical deflections is considerable. Figure 3.7 shows the vertical displacement at the middle of the bottom flange vs. the shear stress. This relatively large difference in the vertical deflection can be attributed to the lower elastic stiffness of the test beam in comparison to the FE model, which can originate from:

1. There is a lack of information about the mechanical properties of the material, including the modulus of elasticity.
2. The measured dimensions of the beam, including the effective distance between the supports and the span length, can be different from what has been reported as the dimensions of the beam according to Table 3.1 since production errors are neglected.
3. The deflection in the test may include the deflections of the supports, and the relative maximum deflection can be less.

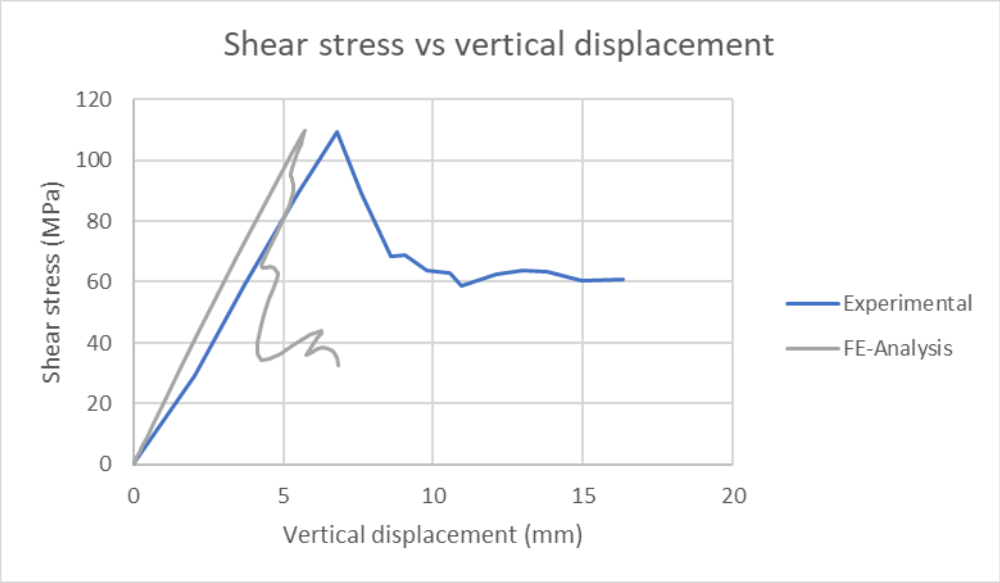

Figure 3-7 Shear stress vs. vertical deflection of the middle of the bottom flange in the test beam (MI2) and FE model.

Figure 3.8 shows the failure and buckling of the test specimen, and Figure 3.9 illustrates the area where buckling started. Figure 3.10 shows the buckling deformation after the maximum load increment. The buckling location in the analyses shows similarities to the observed behaviour in the experiment. The 28th buckling mode has been selected as the pattern for the initial imperfection due to its similarity to the contour of the specimen's initial imperfection. As the location of buckling coincides with the conducted test, a significant effect of initial imperfections in determining the failure mode of corrugated web beams can be observed. The next understanding from the analyses is the importance of a comprehensive level of detail in the modeling process to achieve more realistic results. The development of buckling after reaching the maximum load increment also corresponds to the experimental observations, particularly in the development of buckling after the maximum load increment. This type of buckling can be categorized as local buckling, as evidenced both in the experiment (Figure 3.8) and the 28th buckling mode (Figure 3.6).

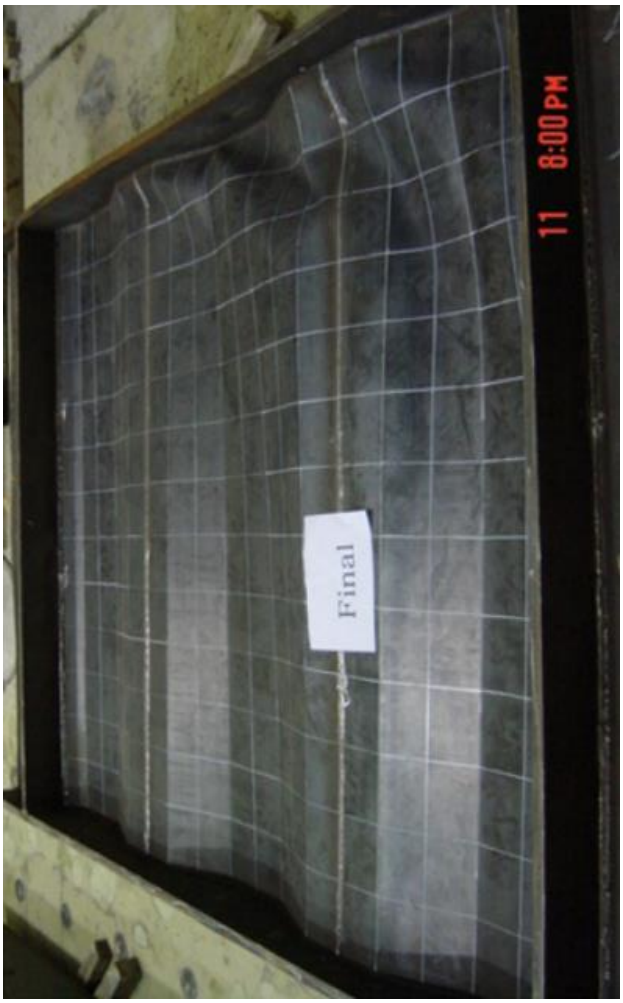

Figure 3-8 Deformed shape of test specimen after loading. [15]

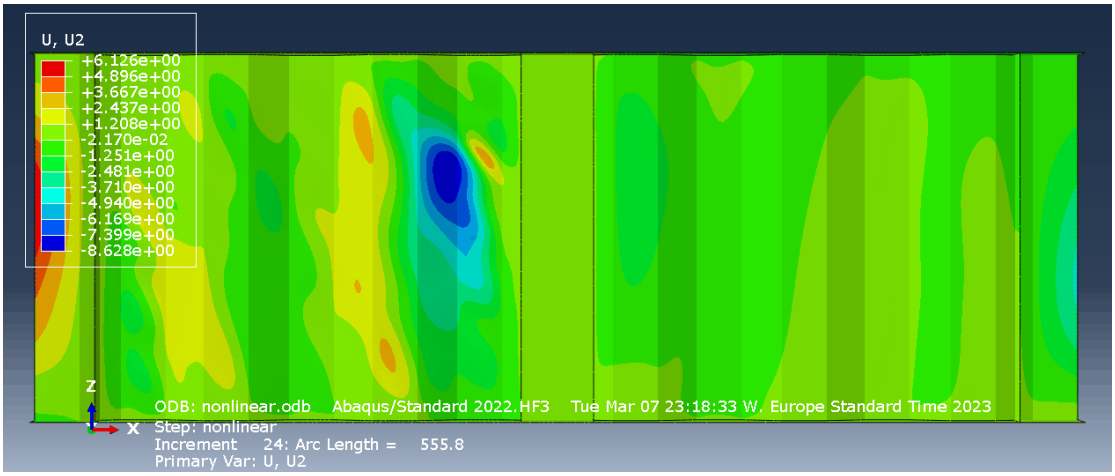

Figure 3-9 The buckling deformation on maximum load increment.

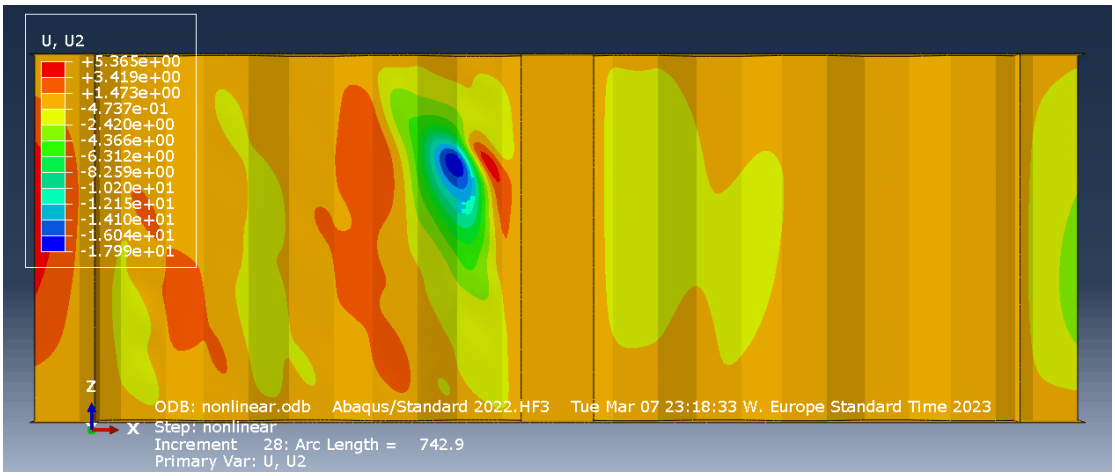

Figure 3-10 The buckling deformation after the maximum loading step.

3.2 Simulation of specimen 1001

This test has been selected to be simulated for the following reasons:

1. The test beams are made of stainless steel, which is very relevant to the current study.
2. Testing conditions and material properties are well described in the main reference.
3. The web panel has been scanned before conducting the test, and the data about the initial geometric imperfections is available.

3.2.1 FE Modelling of 1001 specimen

Specimen 1001 has been tested in order to investigate the shear behavior of a stainless steel beam (steel type: LDX 2101/EN 1.4162). Vertical stiffeners are used under the point load in the middle of the beam as well as at the supports in order to prevent local failure under concentrated forces. In 1001, flat web panels are used at the location of the end supports as well as the middle of the beam. The thickness of the flat web panels is 10 mm. Other dimensions of the beam are presented in Table 3.6, and the configuration of the FEM model of specimen 1001 is indicated in Figures 3.10 and 3.11. The test setup is two-point loading, so in the model, load is distributed on both middle stiffeners. The beam is simply supported, and in the middle, stiffeners are set to resist against lateral movements. The thickness of the corrugated web on the left side of load t_{w1} and the right side t_{w2} is different to control the location of failure.

Table 3-6 Profile of the test specimen, 1001 (all the dimensions are in mm)

Label	a	b	d	h_w	t_{w1}	t_{w2}	b_f	t_f	L
1001	170	85.7	60	1400	4	6	250	25	3818.4

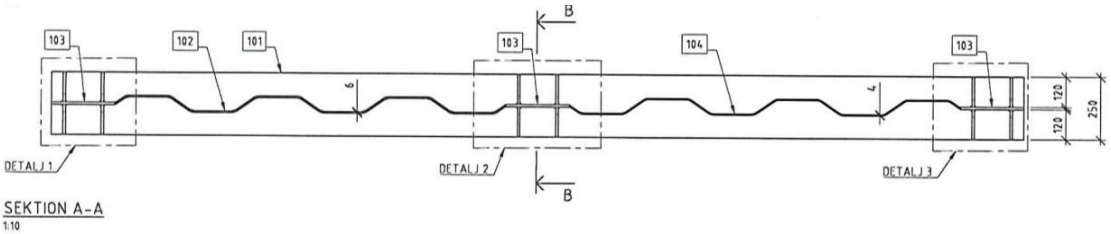

Figure 3-11 The configuration of corrugated web, stiffeners, and flat web panels in 1001 [23].

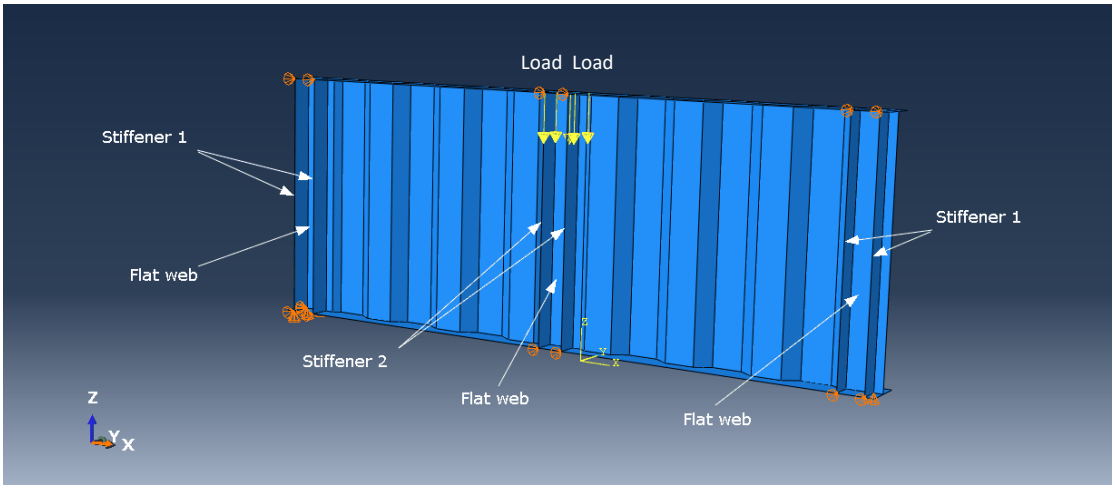

Figure 3-12 The configuration of corrugated web, stiffeners, flat web panels, loads, and support locations

The material properties have been chosen from tensile test data on samples of the tested specimen. Stresses and strains were engineering values and were converted into true values before being introduced in ABAQUS. Table 3.7 indicates the material properties that have been used as input for nonlinear analysis in Abaqus.

Table 3-7 The material properties that have been used in FE modeling of 1001.

E(MPa)	ν	σ_{TT}(MPa)	σ_{T1}(MPa)	σ_{T2}(MPa)	σ_{T3}(MPa)	σ_{T4}(MPa)
195000	0.3	442.8	500	700.1	850	973.87
		ε_{TT}	ε_{T1}	ε_{T2}	ε_{T3}	ε_{T4}
		0	0.000125055	0.017400241	0.096145032	0.244291589

The S4R shell element is used in this analysis. A convergence study on the first eigenvalue was done in order to select a suitable mesh size. Table 3.8 and Figure 3.13 present the results of this study. Accordingly, a mesh size equal to 10 mm is chosen; 25 mm could also be picked, but the author selected 10 mm to compare results with the main reference.

Table 3-8 The mesh size sensitivity and convergence study in the FE modeling of 1001.

Mesh size	Eigenvalue	Error (%)
100	12827	
75	12700	1

50	9308	36.44
25	7405	2.5
18	7238	2.3
12	7092.5	2.05
10	7058.4	0.48
5	6963.2	1.36

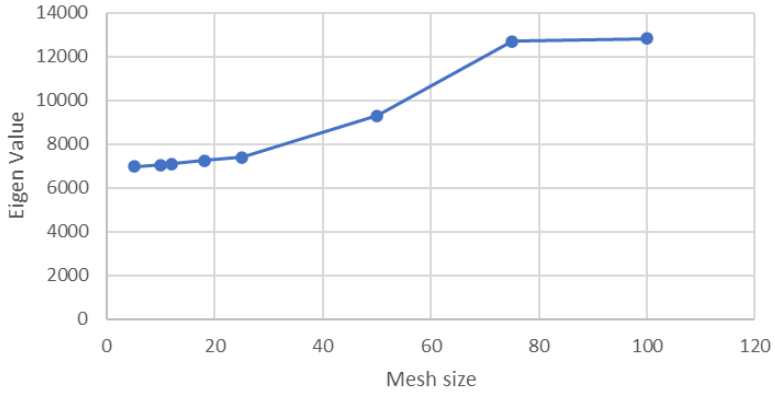

Figure 3-13 The sensitivity of the first eigenvalues to the mesh size in the FE model of 1001.

According to the main reference, the third buckling mode with a maximum relative amplitude of 1 mm was chosen as the initial imperfections in Abaqus. According to the measured imperfection in Fig. 3-14, the magnitude of the imperfections is highest close to the point load, and this corresponds to the 3rd mode. Figure 3.14 shows the DIC-measured initial imperfections of the beam 1001, and Figure 3.15 shows the third buckling mode shape in the FE model.

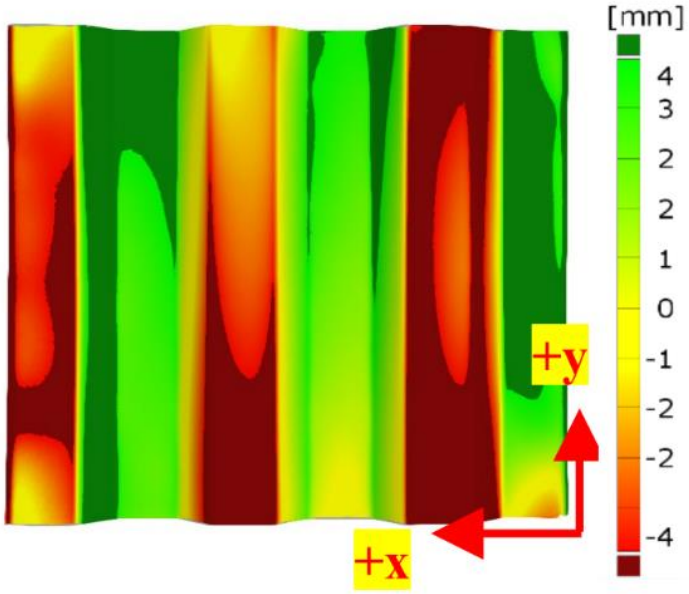

Figure 3-14 The DIC-measured initial imperfection of the corrugated web panel in 1001 [23].

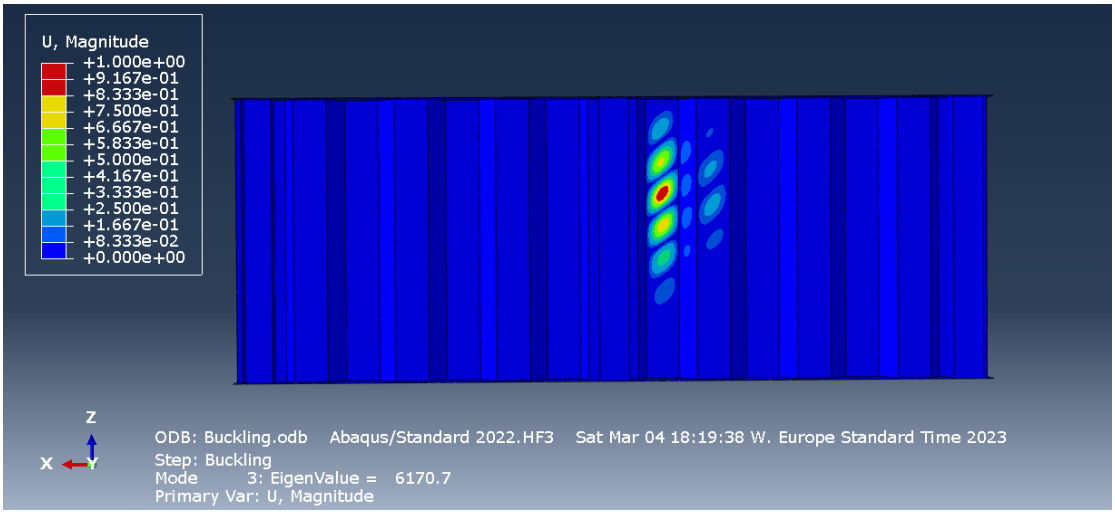

Figure 3-15 The third buckling mode in the FE model of 1001.

3.2.2 Verification results for 1001

Figure 3.16 shows the vertical displacement of the beam vs. the total applied load in both the test and the non-linear FE analysis. Figure 3.17 shows buckling deflection at the maximum load increment. Figure 3.18 shows the distribution of the Von Mises stresses in the FE model at the ultimate load. Figure 3.19 represents the deformed shape of the specimen after failure.

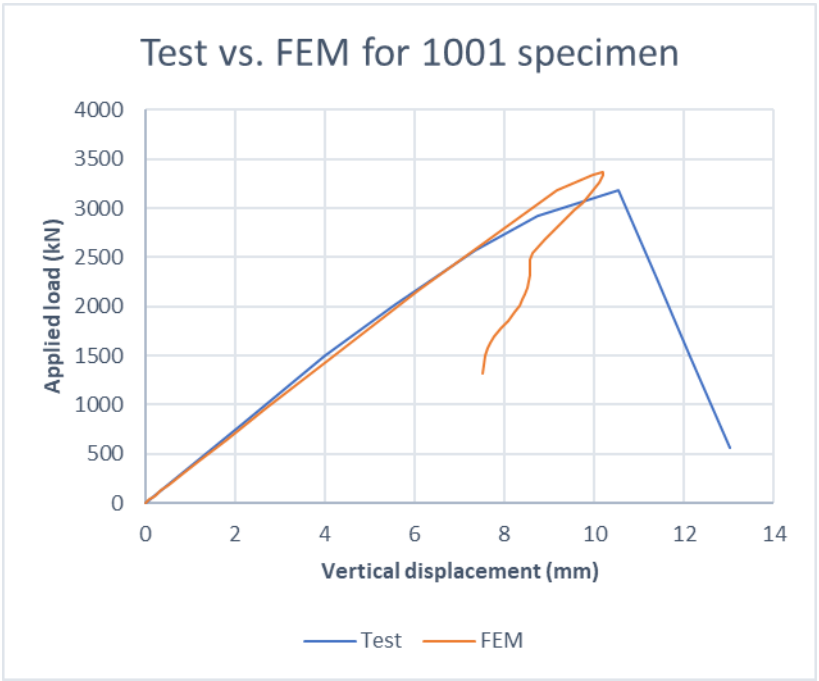

Figure 3-16 The total applied load vs. the vertical displacement in 1001.

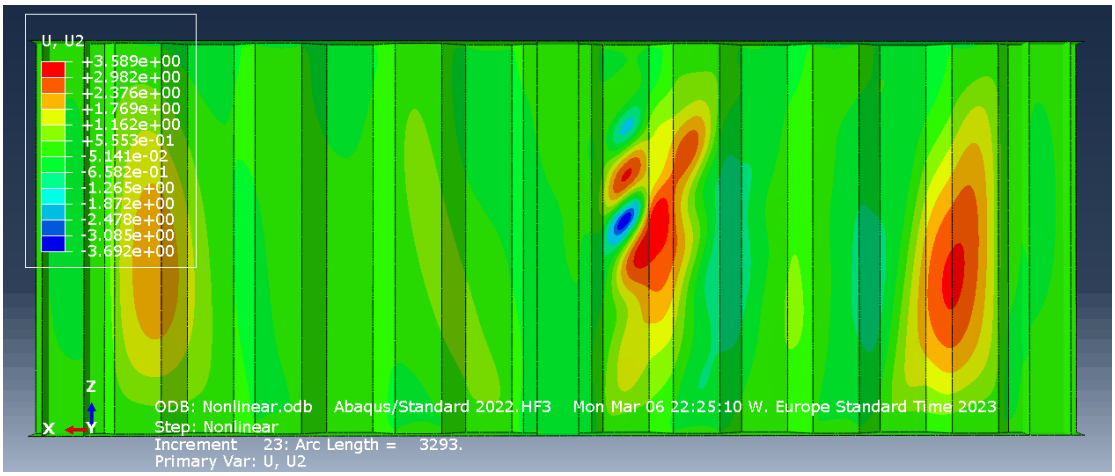

Figure 3-17 The buckling deflection at the maximum load increment.

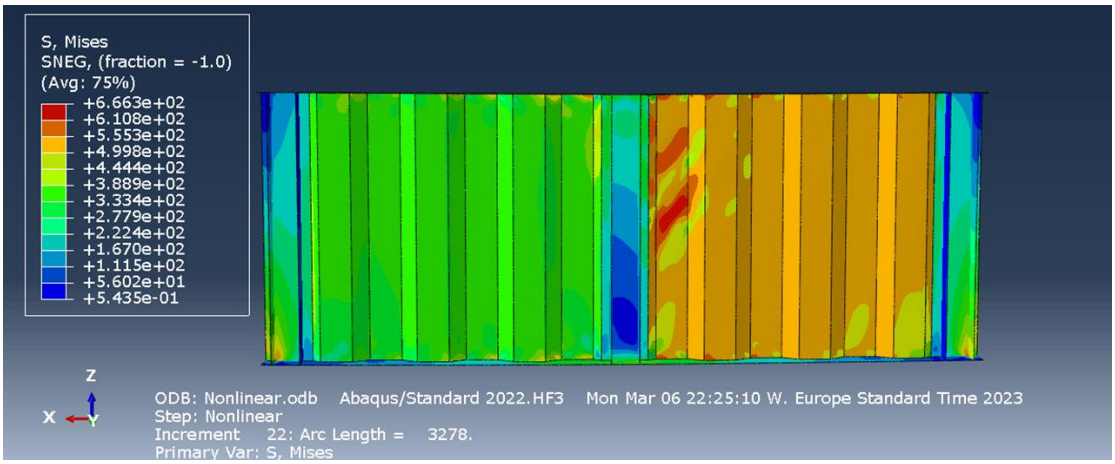

Figure 3-18 This contour represents von mises stress values corresponding to the ultimate load.

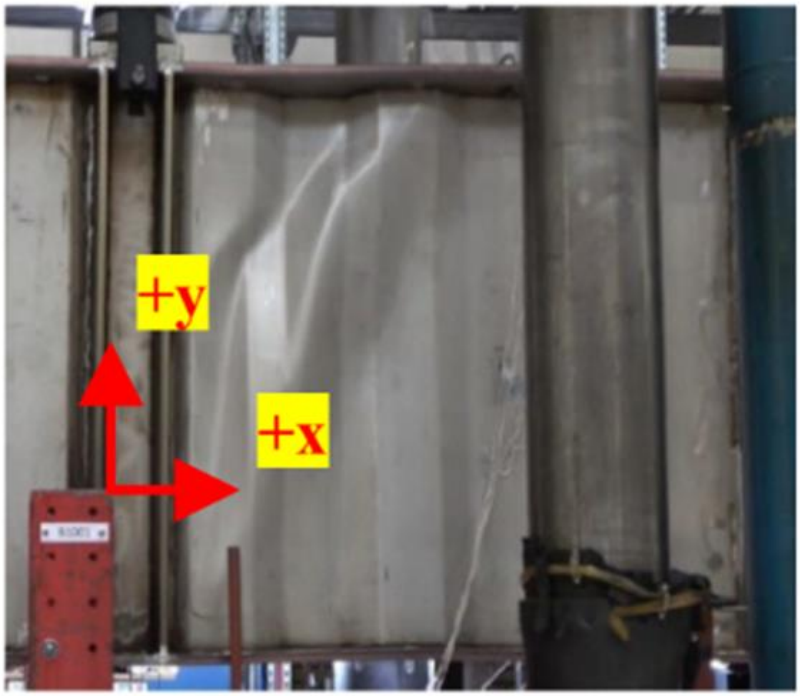

Figure 3-19 Deformed shape of the specimen 1001 after failure [23].

Table 3.9 compares the results of the test and the FEM. It is observed that the difference in both the ultimate load and the vertical deflection is negligible.

Table 3-9 Comparison of the failure load and corresponding vertical displacement in the test and the FEM.

	Failure load (kN)	Vertical displacemet (mm)
Test	3189	10.54
FEM	3370	10.18
Error (%)	5.3	3.4

Conclusion for verification of FEM method

In this chapter, two distinct models, namely specimen MI2 and 1001, have been carefully chosen from published experimental results to validate the Finite Element Method (FEM). The findings presented in tables 3.5 and 3.9, along with the locations where buckling initiates as illustrated in figures 3.9, 3.10, 3.17, and 3.18, serve as a confirmation of the effectiveness of the FEM approach. This validated method will be applied in the subsequent chapter to investigate the reliability of buckling factors outlined in Eurocode 3.

The outcomes of the FEM analysis for specimen MI2 indicate 0.4% error for maximum shear stress and 16% error for maximum vertical displacement. A thorough discussion regarding the rationale behind the higher error in vertical displacement has been previously addressed in this chapter. Similarly, the FEM analysis for specimen 1001 reveals a 5.3% error in failure load and a 3.4% error in maximum vertical displacement. The identification of the initiation points for buckling, coupled with acceptable variances between vertical displacement and failure load, affirms the verification of the FEM approach for the purpose of parametric studies. This validated approach will be further employed in the ensuing chapter to investigate the reliability of the established standards for the shear behavior of corrugated web stainless steel girders.

Imperfection sensitivity studies

After verification of the FEM procedure in the current study, 17 parametric models were designed and modeled in ABAQUS in order to analyze the sensitivity of the shear behaviour to the pattern and amplitudes of initial imperfections in corrugated web beams with a wide range of slenderness ratios. In the process, an eigenbuckling analysis is done first. The first 20 buckling models with three different amplitudes of $\frac{a_{max}}{200}$, t_w and $\frac{h_w}{200}$ are considered as the initial imperfections in all the parametric models. The aim is to study the sensitivity of the ultimate shear capacity to the pattern and amplitude of the initial imperfections. Afterward, a fraction of the maximum buckling deflection was included in a nonlinear Riks analysis as the initial imperfection. It can be mentioned that Riks analysis is performed in order to investigate the nonlinear behaviour of corrugated webs due to buckling and material nonlinearities. Python code is used in order to run analysis for different geometries to decrease modeling time in ABAQUS, but more advanced code can help further investigations. The author later in this Chapter mentioned which subjects need more attention to reach an optimized design solution.
a_{max} is the larger value between the flat panel length and inclined panel width, t_w is the thickness of the web, and h_w is the web height. The thickness of the corrugated web on the left side of the load, t_{w1}, and the right side, t_{w2}, is different to control the location of the failure.
The dimensions of all the considered parametric models are presented in Table 3.10. The material properties, configuration of the loading point, location of stiffeners, and flat web panels are like the test on the 1001 specimen as described in the previous chapter.

Table 3-10 Dimensions of the parametric models in the current study (all the dimensions are in mm)

Name	a	d	θ	h_w	t_{w1}	t_{w2}	b_f	t_f	Span support to support
Model-1	170	60	35	1500	12	16	250	75	5218
Model-2	170	60	35	2000	12	28	250	90	5218
Model-3	170	60	35	2500	12	32	250	90	5218
Model-4	170	60	35	3000	12	38	250	100	5218
Model-5	170	60	35	1500	4	6	250	25	5218
Model-6	170	60	35	3000	4	12	250	40	5218
Model-7	340	60	35	1500	6	8	250	50	7258
Model-8	340	60	35	2000	6	8	250	50	7258
Model-9	340	60	35	3000	6	10	250	50	7258
Model-10	340	60	35	2000	4	6	250	25	7258
Model-11	340	60	35	3000	4	8	250	40	7258
Model-12	340	60	35	1500	8	16	250	70	7258
Model-13	340	60	35	3000	8	16	250	70	7258
Model-14	220	60	35	1500	4	6	250	30	5816
Model-15	220	60	35	3000	4	6	250	70	5816
Model-16	200	60	35	1500	4	6	250	25	5578

Model-17	200	60	35	1500	5	8	250	45	5578

Table 3.11 indicates the result of the nonlinear analysis of parametric models in ABAQUS. Table 3.12 illustrates the calculated slenderness ratio and reduction factors that are calculated by the Eurocode equations that are presented in Chapter 2. The critical mode number is the number of buckling modes that have been used for patterns of initial imperfection with the mentioned magnitude in nonlinear analysis and result in the minimum failure load. χ_u is the ratio between the ultimate shear capacity and the shear yield capacity.

Table 3-11 The results of the nonlinear analyses in ABAQUS in the current parametric FE studies.

Label	Imperf-ection $\frac{a_{max}}{200}$ (mm)	Critical mode number	χ_u	Imperf-ection t_{w1} (mm)	Critical mode number	χ_u	Imperf-ection $\frac{h_w}{200}$ (mm)	Critical mode number	χ_u
Model-1	1	1	1.46	12	4	1.23	7.5	1	1.31
Model-2	1	1	1.42	12	13	1.17	10	13	1.24
Model-3	1	20	1.33	12	-	-	12.5	7	1.08
Model-4	1	2	1.27	12	2	1.09	15	2	1.03
Model-5	1	14	1.11	4	15	0.9	7.5	2	0.79
Model-6	1	19	1.00	4	11	0.89	15	11	0.45
Model-7	1.7	1	0.89	6	1	0.69	7.5	1	0.65
Model-8	1.7	1	0.88	6	5	0.72	10	1	0.54
Model-9	1.7	5	0.75	6	5	0.54	15	5	0.29
Model-10	1.7	5	0.54	4	5	0.48	10	5	0.37
Model-11	1.7	7	0.48	4	7	0.37	15	7	0.17
Model-12	1.7	1	1.09	8	4	0.78	7.5	-	-
Model-13	1.7	16	0.98	8	6	0.66	15	6	0.48
Model-14	1.1	2	0.96	4	2	0.75	7.5	2	0.58
Model-15	1.1	1	0.94	4	1	0.74	15	1	0.36
Model-16	1	4	1.01	4	4	0.77	7.5	4	0.54
Model-17	1	1	1.19	5	3	0.95	7.5	3	0.83

Table 3-12 Calculated slenderness ratios and reduction factors for both local and global buckling for the parametric models using the Eurocode equations and also indication of critical buckling modes.

Name	FEM buckling critical mode-Imperfection: a_{max}/200	FEM buckling critical mode-Imperfection: t_w	FEM buckling critical mode-Imperfection: h_w/200	$\lambda_{c,l}$	$\lambda_{c,g}$	χ_l	χ_g
Model-1	Global	Local interactive	Global	0.23	0.57	1	1
Model-2	Global	Global interactive	Global interactive	0.23	0.76	1	1
Model-3	Local interactive	-	Local interactive	0.23	0.96	1	1
Model-4	Global	Global	Global	0.23	1.15	1	0.82
Model-5	Local	Local interactive	Local interactive	0.7	0.77	0.72	1
Model-6	Global interactive	Local interactive	Local interactive	0.7	1.55	0.72	0.52

Model-7	Global interactive	Global interactive	Global interactive	0.94	0.66	0.63	1
Model-8	Global interactive	Local interactive	Global interactive	0.94	0.88	0.63	1
Model-9	Global interactive	Global interactive	Global interactive	0.94	1.34	0.63	0.65
Model-10	Local interactive	Local interactive	Local interactive	1.41	0.99	0.5	1
Model-11	Global interactive	Global interactive	Global interactive	1.41	1.49	0.5	0.55
Model-12	Global	Local interactive	-	0.7	0.60	0.72	1
Model-13	Local interactive	Global interactive	Global interactive	0.70	1.24	0.72	0.74
Model-14	Local interactive	Local interactive	Local interactive	0.91	0.75	0.63	1
Model-15	Local interactive	Local interactive	Local interactive	0.91	1.50	0.63	0.54
Model-16	Global interactive	Global interactive	Global interactive	0.83	0.76	0.67	1
Model-17	Global interactive	Global interactive	Global interactive	0.66	0.71	0.74	1

Figures 3.20 to 3.36 indicate:

1) FEM reduction factors for the models with different imperfection values and different imperfection patterns.
2) The calculated reduction factor based on the Eurocode equations.

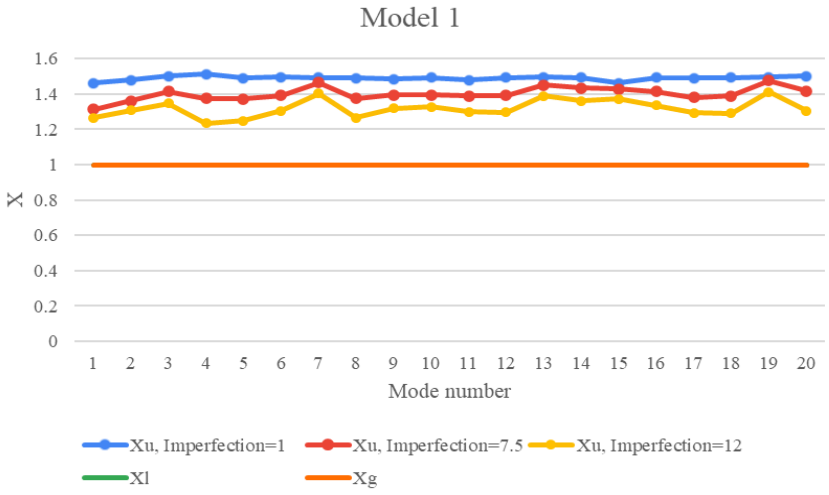

Figure 3-20 Indication of χ_u extracted by FEM analysis versus calculated χ_l and χ_g by Eurocode equations for model-1.

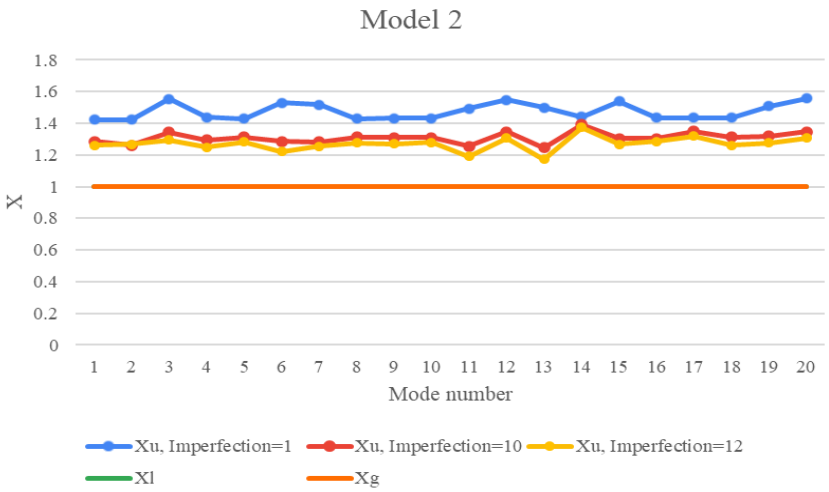

Figure 3-21 Indication of χ_u extracted by FEM analysis versus calculated χ_l and χ_g by Eurocode equations for model-2.

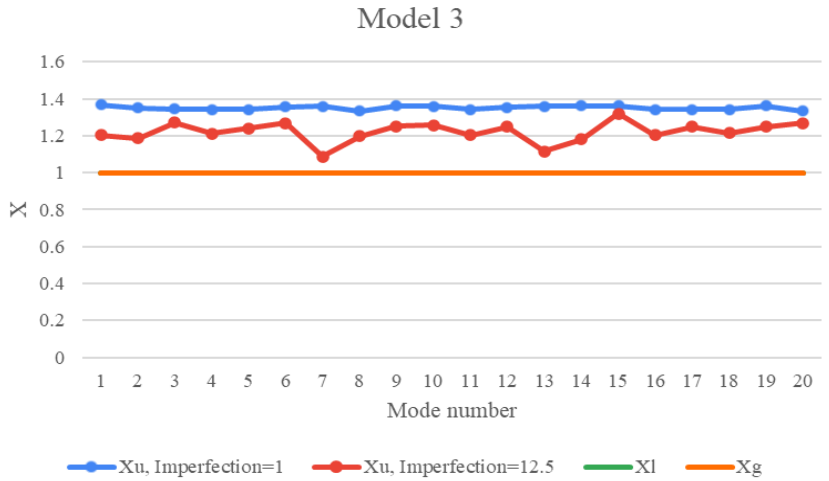

Figure 3-22 Indication of χ_u extracted by FEM analysis versus calculated χ_l and χ_g by Eurocode equations for model-3.

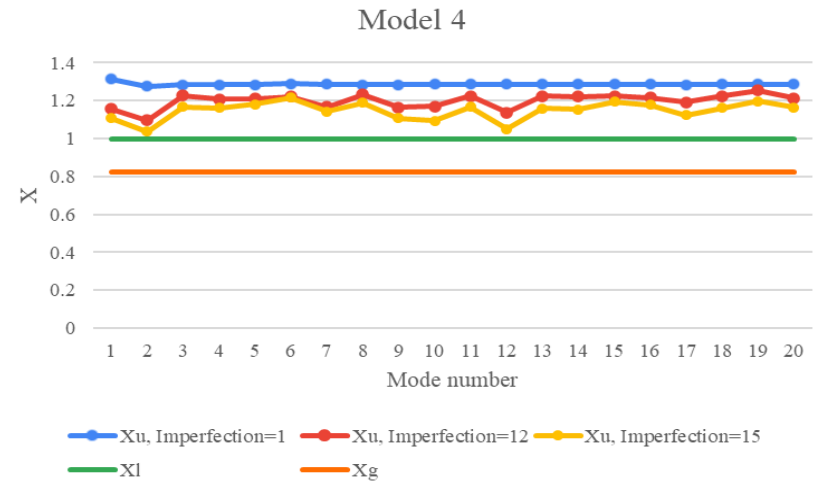

Figure 3-23 Indication of χ_u extracted by FEM analysis versus calculated χ_l and χ_g by Eurocode equations for model-4.

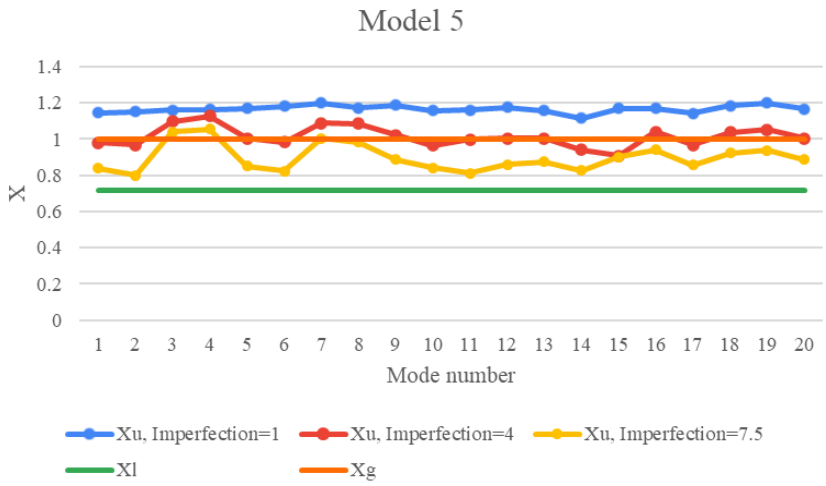

Figure 3-24 Indication of X_u extracted by FEM analysis versus calculated X_l and X_g by Eurocode equations for model-5.

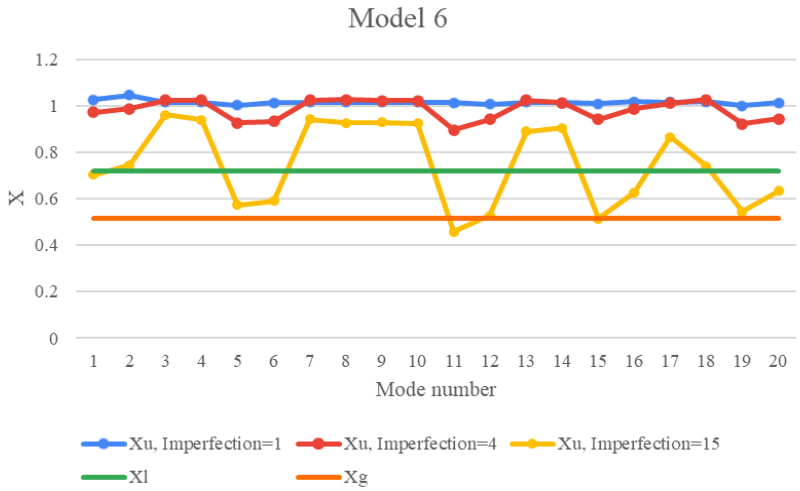

Figure 3-25 Indication of X_u extracted by FEM analysis versus calculated X_l and X_g by Eurocode equations for model-6.

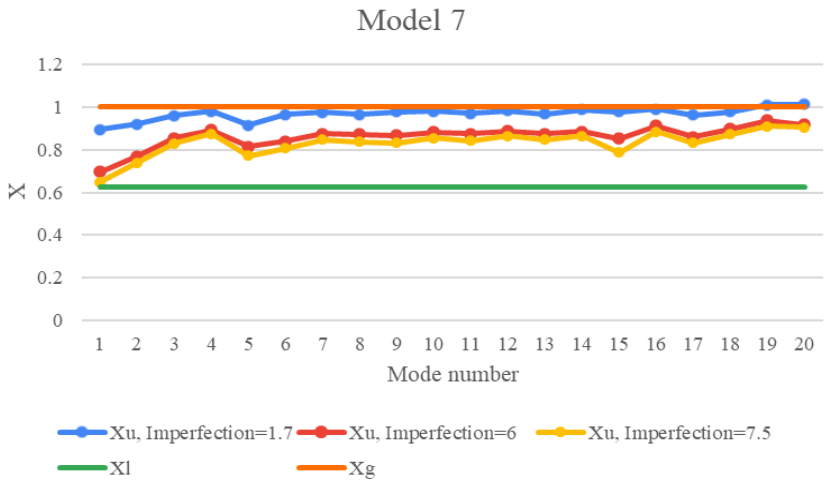

Figure 3-26 Indication of X_u extracted by FEM analysis versus calculated X_l and X_g by Eurocode equations for model-7.

Figure 3-27 Indication of $\mathcal{X}_u$ extracted by FEM analysis versus calculated $\mathcal{X}_l$ and $\mathcal{X}_g$ by Eurocode equations for model-8.

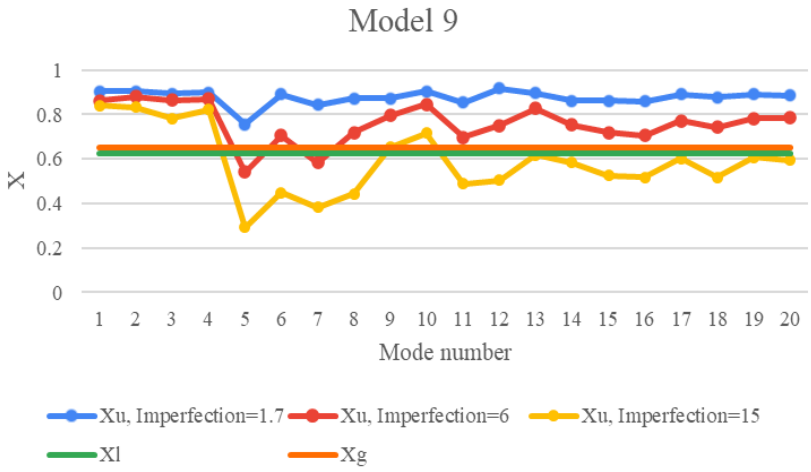

Figure 3-28 Indication of $\mathcal{X}_u$ extracted by FEM analysis versus calculated $\mathcal{X}_l$ and $\mathcal{X}_g$ by Eurocode equations for model-9.

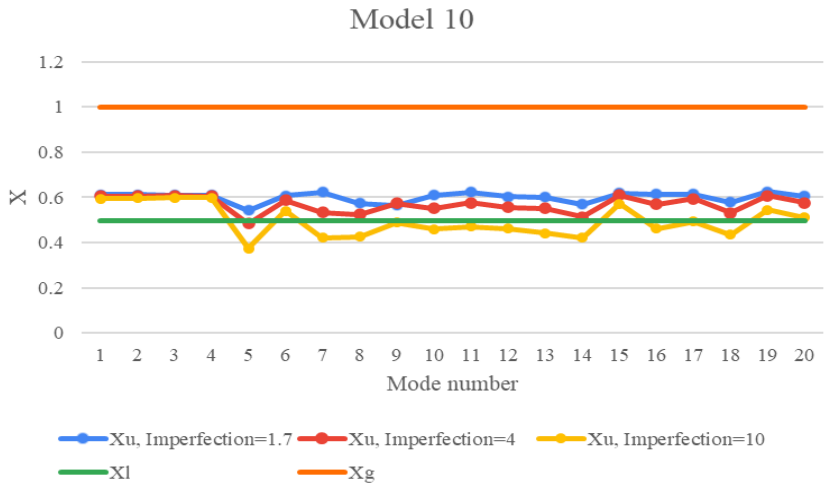

Figure 3-29 Indication of $\mathcal{X}_u$ extracted by FEM analysis versus calculated $\mathcal{X}_l$ and $\mathcal{X}_g$ by Eurocode equations for model-10.

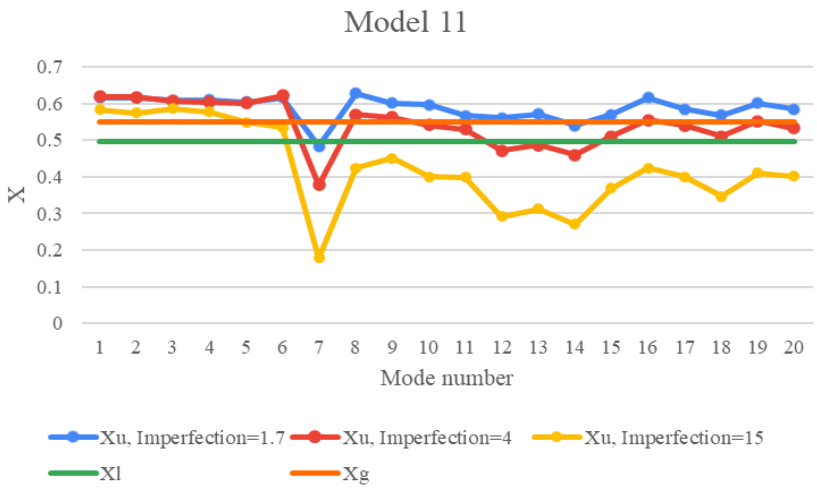

Figure 3-30 Indication of X_u extracted by FEM analysis versus calculated X_l and X_g by Eurocode equations for model-11.

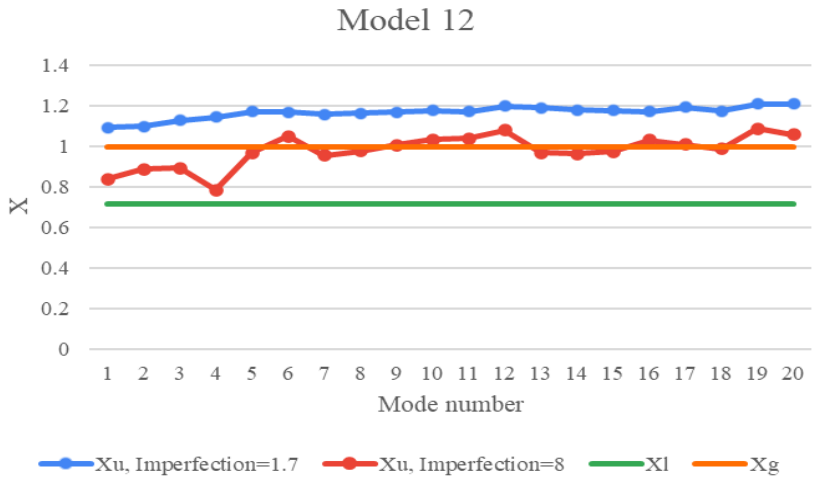

Figure 3-31 Indication of X_u extracted by FEM analysis versus calculated X_l and X_g by Eurocode equations for model-12.

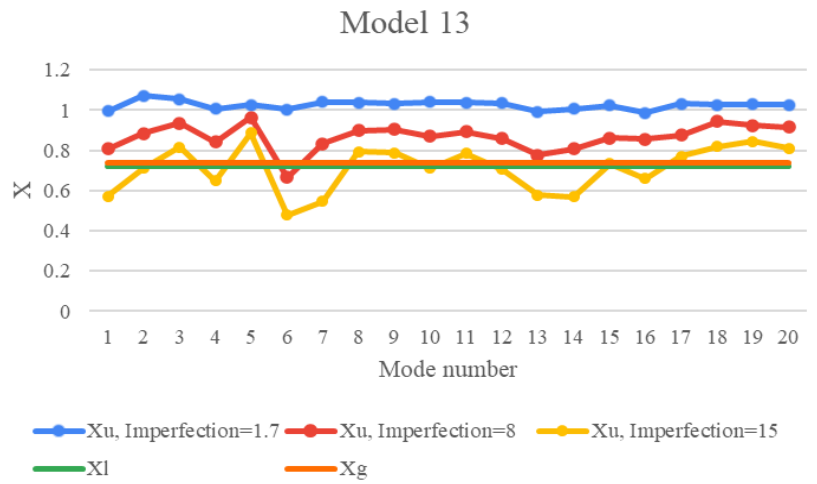

Figure 3-32 Indication of X_u extracted by FEM analysis versus calculated X_l and X_g by Eurocode equations for model-13.

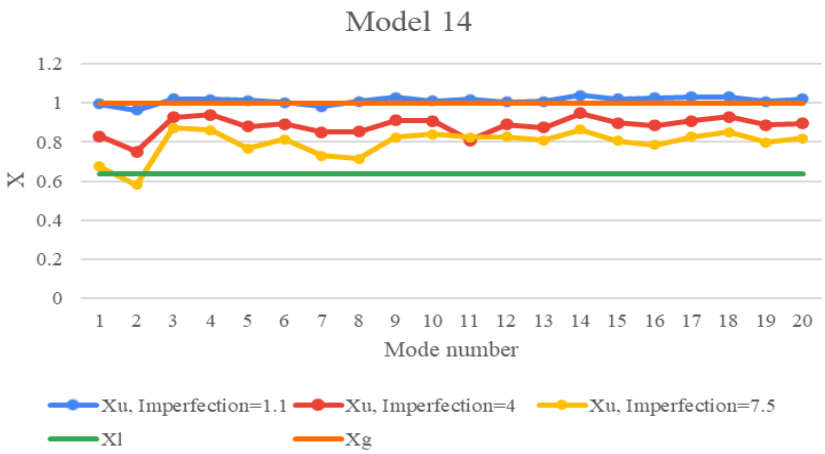

Figure 3-33 *Indication of $\mathcal{X}_u$ extracted by FEM analysis versus calculated $\mathcal{X}_l$ and $\mathcal{X}_g$ by Eurocode equations for model-14.*

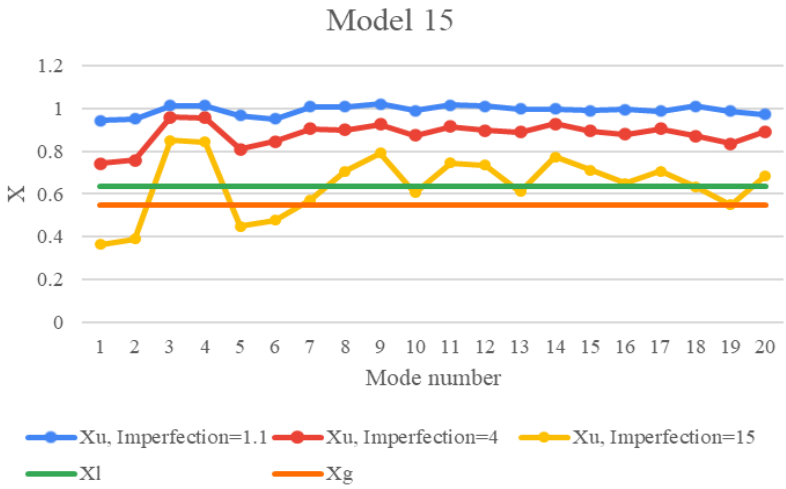

Figure 3-34 *Indication of $\mathcal{X}_u$ extracted by FEM analysis versus calculated $\mathcal{X}_l$ and $\mathcal{X}_g$ by Eurocode equations for model-15.*

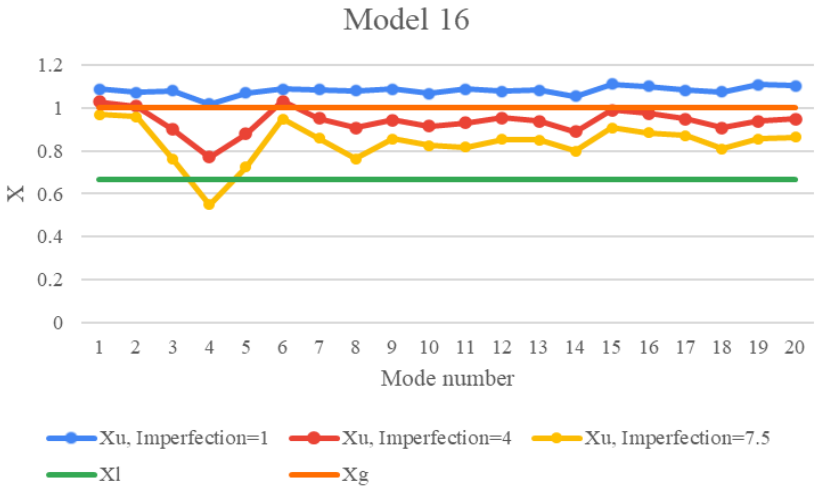

Figure 3-35 *Indication of $\mathcal{X}_u$ extracted by FEM analysis versus calculated $\mathcal{X}_l$ and $\mathcal{X}_g$ by Eurocode equations for model-16.*

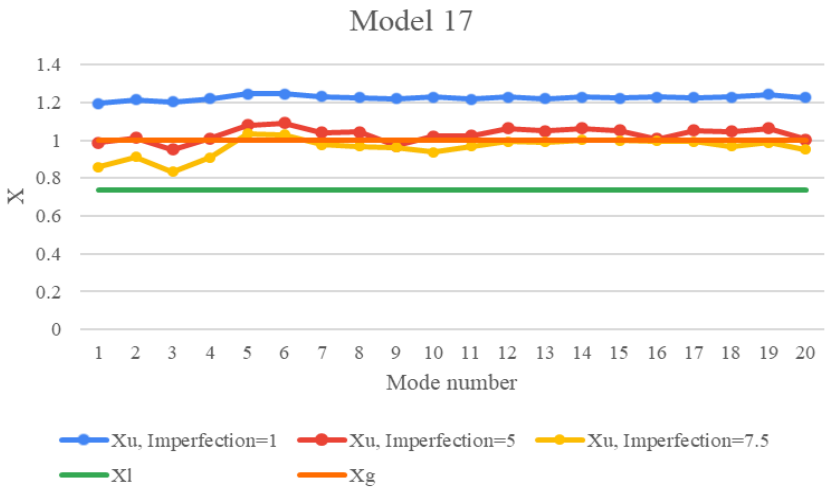

Figure 3-36 Indication of $\mathcal{X}_u$ extracted by FEM analysis versus calculated $\mathcal{X}_l$ and $\mathcal{X}_g$ by Eurocode equations for model-17.

The critical buckling modes for different imperfection values, the deflections, and Von Misses stress distribution at the point of shear failure for the FE models are depicted in Figure 5.1 to 5.125.

According to Table 3.12, 73% of critical modes are interactive. Models 1-4, all with a very low local slenderness ratio (0.23) and a global slenderness not above 1 (except model 4), show an ultimate shear capacity greater than the shear yield strength, according to χ_u values in Table. 3-11. According to the reported critical buckling modes in Table 3-12, all the critical modes on such models that attain the full yield capacity are global or interactive. The reason for this is discussed in [23], as in cases where the yielding in shear precedes the shear buckling, those buckling modes that are more extended over the web panel cause a larger degradation of the ultimate capacity.
Model 5, with a medium local slenderness (0.7) and not a high global slenderness, still has the potential to reach the full shear yield capacity for low amplitudes of imperfection. However, for higher values of imperfection, the ultimate shear capacity gets lower than the shear yield capacity. Again, with the same reasoning as discussed about models 1-4, it is expected that those mode shapes that are more extended over the web panel cause a larger degradation of the ultimate capacity.
In model 6, the global slenderness is much higher than the local slenderness, but still, the critical buckling mode is interactive. Again, for a small amplitude of imperfection, the beam reaches the shear yield capacity. However, the ultimate shear load is reduced for the higher values of imperfection, like model 5.
In models 7 and 8, the local and global slenderness ratios are both under 1, and the critical buckling mode shapes are interactive. It is observed in Figs. 3.26 and 3.27 that for all the considered imperfection amplitudes and patterns, the ultimate shear capacity is less than the yield strength.
In model 9, the local slenderness ratio is approximately 1, and the global slenderness ratio is more than 1. The critical buckling modes, as shown in Figs. 5.62 to 5.68, are global. However, Eurocode's local and global buckling reduction factors are approximately the same. According to Fig. 3.28, the ultimate shear resistance for a wide range of imperfection magnitudes and patterns is less than the shear yield strength. On the other hand, it is observed that for the highest imperfection magnitude and buckling modes 5 to 9, the ultimate shear strength is lower than what is predicted based on Eurocode's equations.

In model 10, the local slenderness ratio is larger than the global slenderness ratio. However, since the global slenderness ratio is near 1, the critical buckling mode is interactive rather than pure local. It is observed in Fig. 3.29 that the ultimate shear strength in a wide range of imperfections is less than the shear yield strength. However, for the low and medium imperfection amplitudes, the Eurocode's predicted shear strength is conservative. But, for the highest imperfection amplitude, the Eurocode's predicted shear strength can be nonconservative for the critical buckling models.
In model 11, the local and global slenderness ratios as well as the local and global buckling reduction factors are approximately the same, and the critical buckling modes, as shown in Figs. 5.76 to 5.82, are global or interactive. Thus, like what is observed in the case of model 10, the ultimate shear strength is less than the shear yield strength, and Eurocode's predicted shear strength can be non-conservative for all the imperfection amplitudes if the critical buckling mode shape (mode 7) is considered.
In model 12, the local and global slenderness ratios are less than 1. The critical buckling mode shapes are global or interactive. It is observed in Fig. 4.12 that for the minimum imperfection amplitude, the ultimate shear strength can reach the shear yield strength. However, when the amplitude of the imperfection increases, then the ultimate capacity is less than the yield strength. It seems that the reason for the low local buckling reduction factor calculated based on Eurocode is this high imperfection sensitivity.
In model 13, the local slenderness ratio is less than 1, and the global slenderness ratio is greater than 1. However, Eurocode's calculated local and global buckling reduction factors are approximately the same. The critical buckling modes, as shown in Figs. 5.89 to 5.96, are interactive. According to Fig. 3.32, the ultimate shear resistance for a wide range of imperfection magnitudes and patterns is less than the shear yield strength. On the other hand, it is observed that for the highest imperfection magnitude and buckling modes 6, 7, 13, and 14, the ultimate shear strength is lower than what is predicted based on Eurocode's equations. However, it is observed that for the lowest imperfection amplitude, the ultimate shear strength can reach the shear yield strength.
In model 14, with a local slenderness ratio close to 1 and a global slenderness ratio less than 1, the critical buckling modes, as shown in Figs. 5.97 to 5.103, are interactive. For low amplitudes of imperfections, there is still potential to reach the shear yield strength. However, for higher values of imperfection, the ultimate shear capacity gets lower than the shear yield capacity.
In model 16, with a local and global slenderness ratio less than 1 and close to 0.8, according to Fig. 3.35, for the low imperfection amplitude, the shear yield strength is attainable. However, for higher imperfections, the shear capacity is less than the shear yield strength, and in some cases, for the critical buckling mode shapes, Eurocode's predicted buckling reduction factors can be non-conservative.
In model 17, in which both the local and global slenderness ratios are less than 1 and close to 0.7 for the low and medium imperfection amplitudes, the ultimate shear resistance is observed to reach the shear yield strength in a wide range of imperfection mode shapes. On the other hand, Eurocode's buckling reduction factors are conservative in a wide range of imperfections. According to Figs. 3.20 to 3.36, in most of the cases, the critical buckling mode shapes are different from the first buckling mode. However, in models 15, 8, and 7 the critical buckling mode is the first buckling mode. In model 15, it is observed that for the first buckling mode and the imperfection amplitudes of low and medium values, Eurocode's predicted buckling reduction factors are safe. However, for the highest imperfection amplitude, Eurocode gives non-conservative reduction factors.

Discussion and conclusion

3.3 Verification of Eurocode equations

The data from Table 3.11 and from the 17 models that have been analyzed in ABAQUS have been presented in Figures 3.37 and 3.38 in order to compare the reduction factors with the calculated reduction factors based on Eurocode. According to these figures, for local buckling, almost 14% of the reduction factors of conducted tests are less than the calculated buckling factor by Eurocode equations, and for global buckling, this number is almost 13%. It shows that the recommended equation for the calculation of the reduction factor is non-conservative and needs to be revised for stainless steel. Investigation on imperfection sensitivity shows that the recommended buckling reduction factor by Eurocode is safe for imperfection equal to $\frac{a_{max}}{200}$ but not for imperfection amplitudes of t_w and $\frac{h_w}{200}$.

In order to investigate the applicability of the first buckling mode as the initial imperfection pattern for non-linear analysis, it can be mentioned that for imperfection magnitude equal to $\frac{a_{max}}{200}$, only 7 from 17 models, for imperfection magnitude equal to t_w, only 2 from 17 models, and for imperfection magnitude equal to $\frac{h_w}{200}$, only 4 from 17 models are observed with first buckling mode as critical buckling mode.

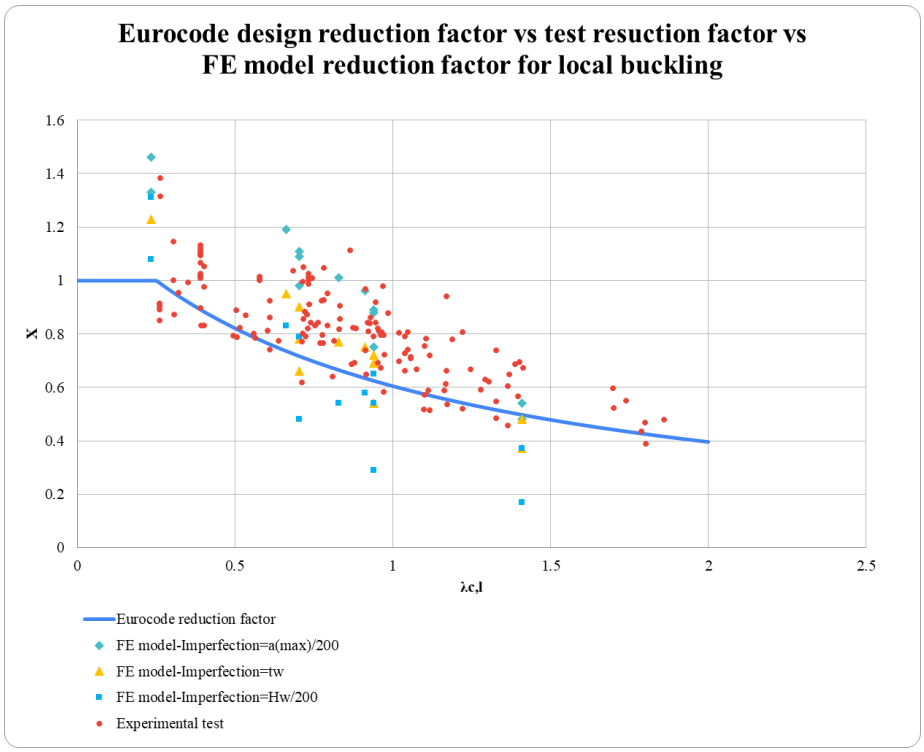

Figure 3-37 Indication of shear design reduction factors for local buckling which are calculated by both Eurocode equations, extracted from generated database and reduction factors extracted from FEM analysis.

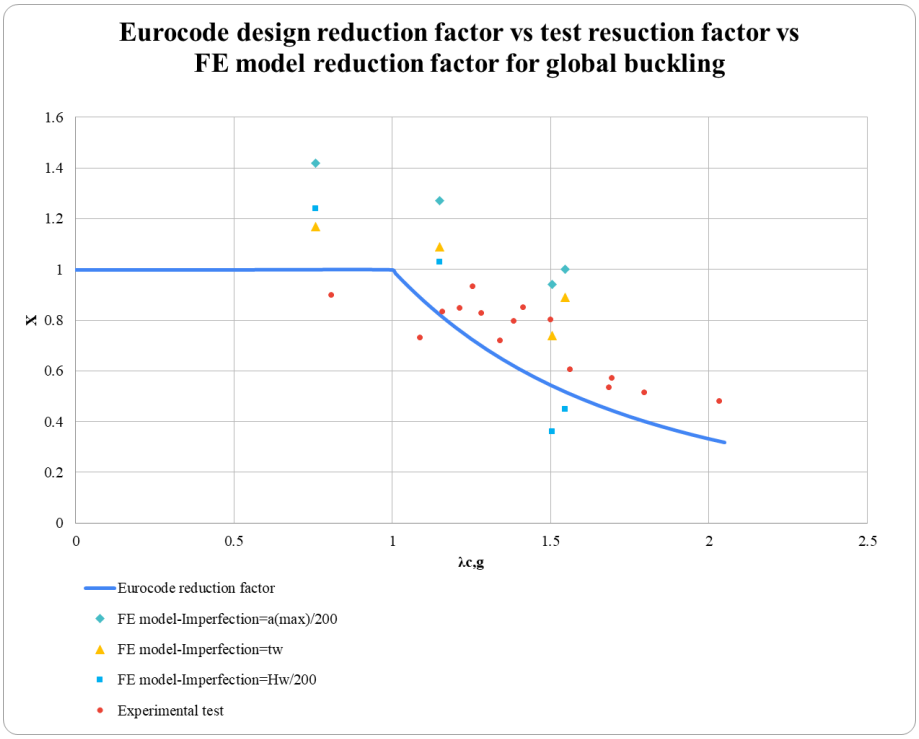

Figure 3-38 Indication of shear design reduction factors for global buckling which are calculated by both Eurocode equations, extracted from generated database and reduction factors extracted from FEM analysis.

The author suggests new equations considering imperfection limitations for design; this limit can be expected from the manufacturer's company of corrugated web to be considered a required standard to produce girders. The mentioned equations are created by small changes to the Eurocode model and are proposed with limited data from FEM analysis, so these equations need to be revised with more data in the future and are the basis for further investigations. Another reason for questioning the reliability of the developed equations is that for the same slenderness ratios, different ultimate reduction factors can be found. Indicated slenderness ratios are calculated according to the mentioned equations from Eurocode in Chapter 2. Figures 3.39 and 3.40 show both reduction factors calculated by Eurocode's equations and the recommended model for an initial imperfection magnitude equal to $a_{max}/200$. From Figure 3.39, in local buckling, Eurocode standard is conservative for slenderness ratios smaller than 1.15. The recommended model in Figure 3.40 for global buckling is not as accurate as the recommended model for local buckling, as less data is available in this case, but the Eurocode reduction factor is conservative. Figures 3.41 and 3.42 show the recommended model for local and global buckling, with considering t_w as initial imperfection magnitude. From Figure 3.41, using the Eurocode reduction factor is not safe for local buckling, but for global buckling in Figure 3.42, it is conservative. However, when the initial imperfection magnitude has a value equal to $h_w/200$ according to Figures 3.43 and 3.44, the Eurocode standard is not safe to use. Equations 3.1 to 3.6 are presented by the author for the calculation of the buckling reduction factors with limited initial imperfection magnitude.

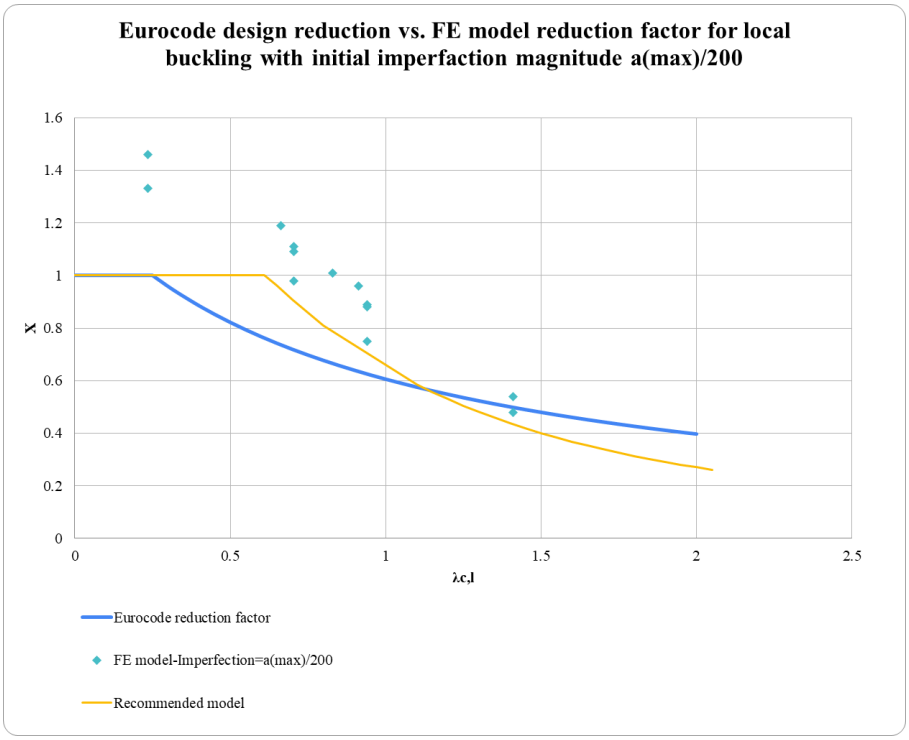

Figure 3-39 *Indication of ultimate reduction factors for analyzed models with initial imperfection equal to $a_{max}/200$, recommended model for reduction factor and calculated reduction factor by Eurocode's equations for local buckling.*

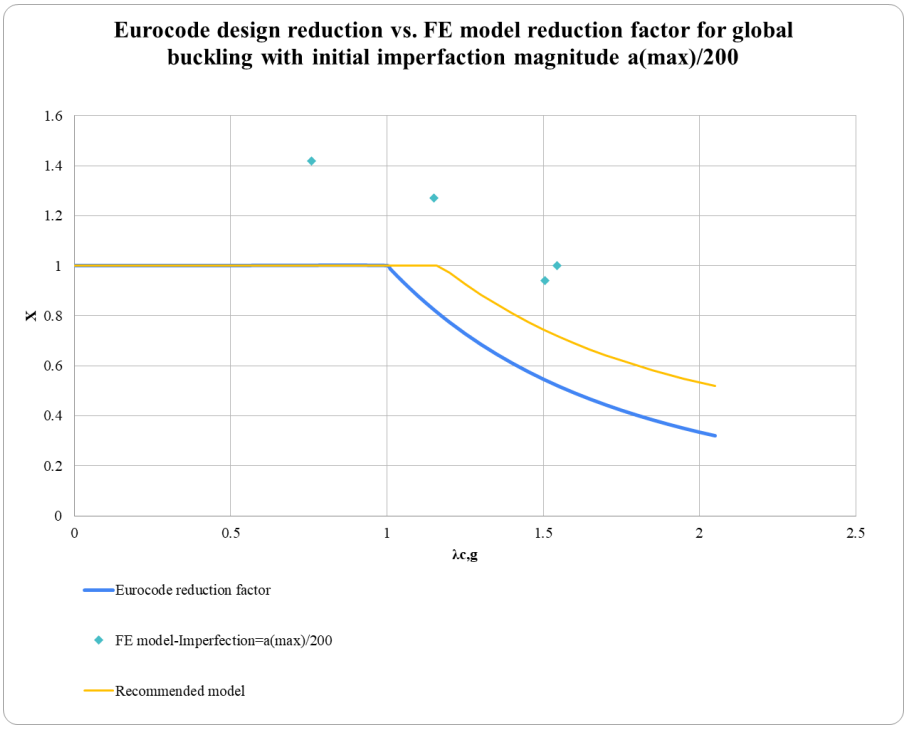

Figure 4-40 *Indication of ultimate reduction factors for analyzed models with initial imperfection equal to $a_{max}/200$, recommended model for reduction factor and calculated reduction factor by Eurocode's equations for global buckling.*

$$\chi_{c,l} = \left[\frac{1.3}{0.6+\lambda_{c,l}{}^{1.7}}\right] \times 0.8 \qquad \chi_{c,l} < 1 \qquad \text{Max imperfection}=a_{max}/200 \quad (3.1)$$

$$\chi_{c,g} = \left[\frac{1.5}{0.5+\lambda_{c,g}{}^{2}}\right] + 0.2 \qquad \chi_{c,g} < 1 \qquad \text{Max imperfection}=a_{max}/200 \quad (3.2)$$

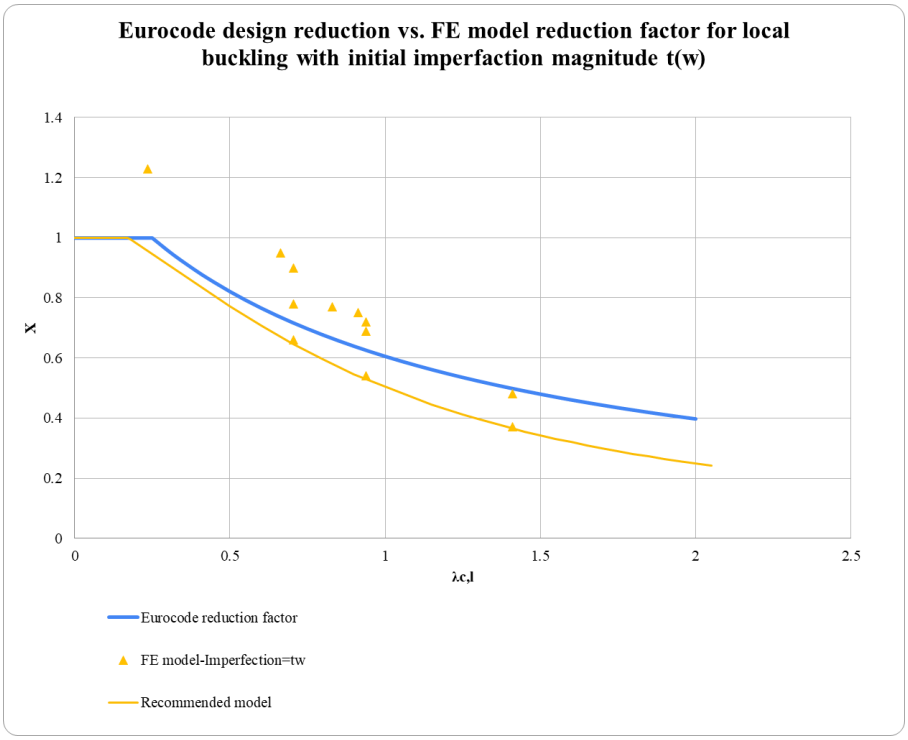

Figure 3-41 Indication of ultimate reduction factors for analyzed models with initial imperfection equal to t_w, recommended model for reduction factor and calculated reduction factor by Eurocode's equations for local buckling.

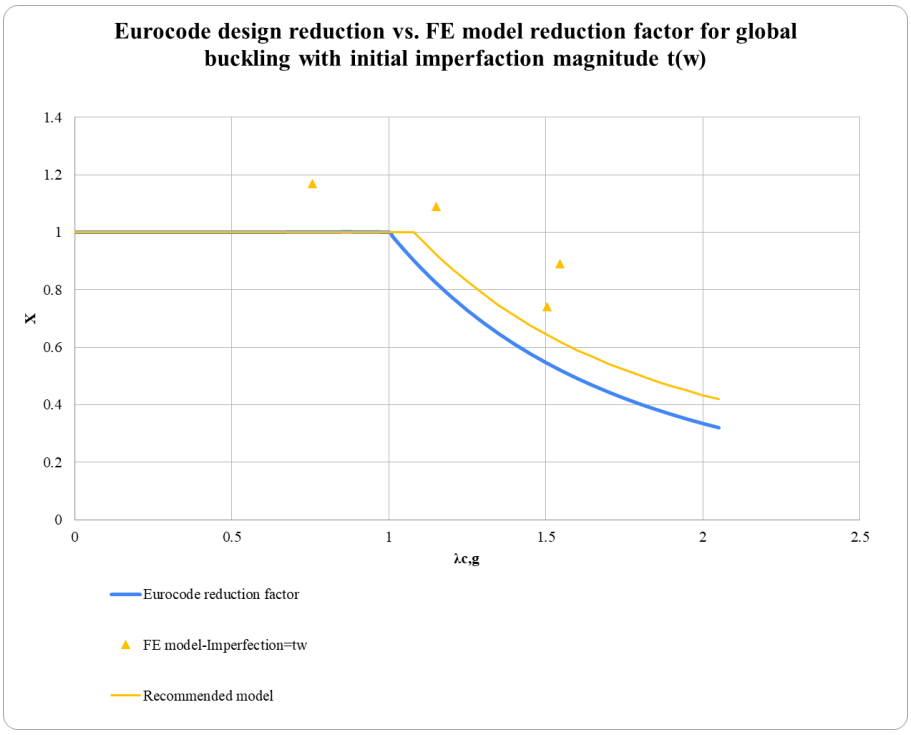

Figure 3-42 Indication of ultimate reduction factors for analyzed models with initial imperfection equal to t_w, recommended model for reduction factor and calculated reduction factor by Eurocode's equations for global buckling.

$$\chi_{c,l} = \left[\frac{1.35}{0.88+ \lambda_{c,l}{}^{1.55}}\right] \times 0.7 \qquad \chi_{c,l} < 1 \qquad \text{Max imperfection=}t_w \qquad (3.3)$$

$$\chi_{c,g} = \left[\frac{1.5}{0.5+\lambda_{c,g}{}^{2}}\right] + 0.1 \qquad \chi_{c,g} < 1 \qquad \text{Max imperfection=}t_w \qquad (3.4)$$

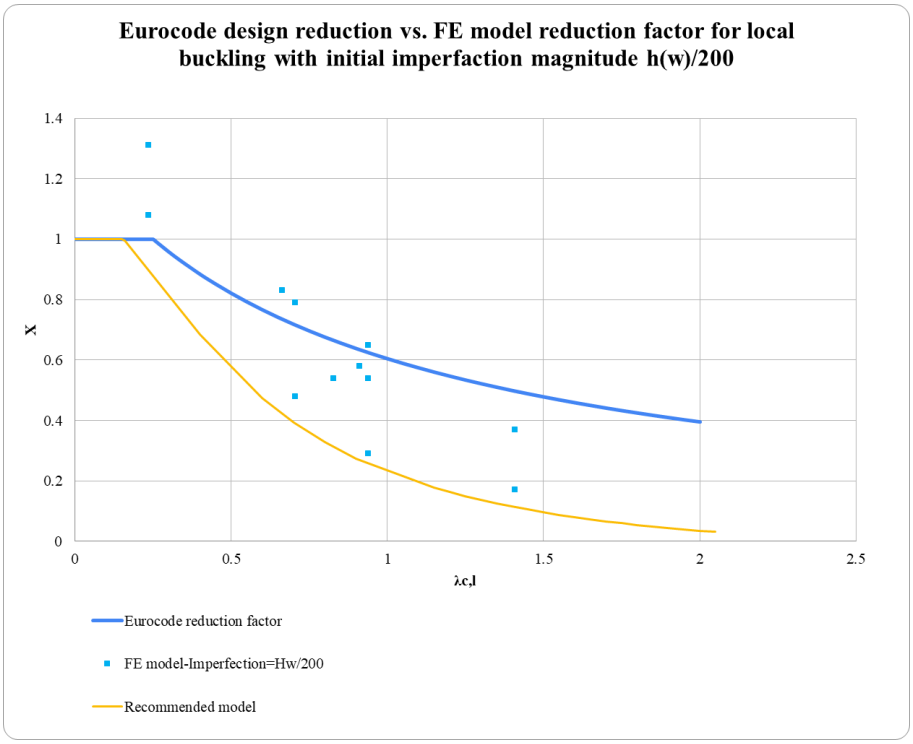

Figure 3-43 *Indication of ultimate reduction factors for analyzed models with initial imperfection equal to $h_w/200$, recommended model for reduction factor and calculated reduction factor by Eurocode's equations for local buckling.*

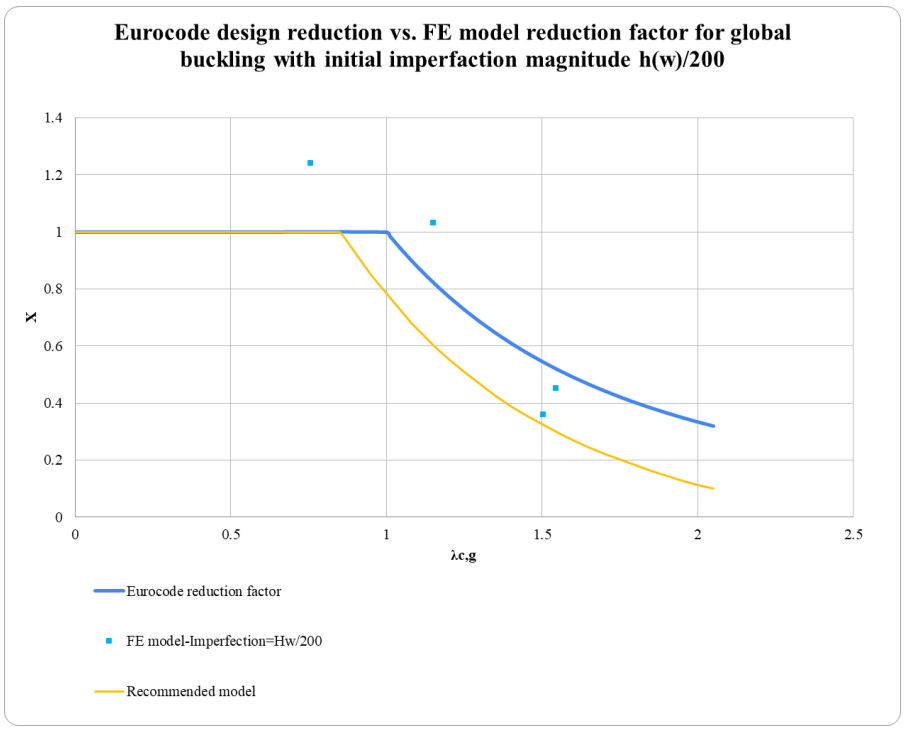

Figure 3-44 *Indication of ultimate reduction factors for analyzed models with initial imperfection equal to $h_w/200$, recommended model for reduction factor and calculated reduction factor by Eurocode's equations for global buckling.*

$$\chi_{c,l} = \left[\frac{0.6}{0.34+ \lambda_{c,l}{}^{1.8}}\right] \times 0.67 - 0.07,\ \chi_{c,l} < 1 \quad \text{Max imperfection=} h_w/200 \quad (3.5)$$

$$\chi_{c,g} = \left[\frac{1.5}{0.5+\lambda_{c,g}{}^{2}}\right] - 0.22 \qquad \chi_{c,g} < 1 \quad \text{Max imperfection=} h_w/200 \quad (3.6)$$

As a concluding remark for this master thesis, Chapter 3 has successfully verified the Finite Element Method (FEM) to facilitate parametric studies. These studies involved generating models with varying dimensions, which were then coupled with the database derived from a literature review, as outlined in Table 2.2. The objective was to assess the conservatism of reduction factors calculated by the equations presented in Eurocode 3. The results, depicted in Figures 3.37 and 3.38, reveal that, for local buckling, 14% and for global buckling, 13% exhibit lower reduction factors than those calculated by Eurocode 3. Consequently, it is evident that the equations from Eurocode 3 do not result in conservative reduction factors and may not be entirely suitable for safe application for the case of stainless steel corrugated web girders.

Furthermore, the FEM analysis elucidated that the effectiveness of reduction factors is not solely contingent upon imperfection magnitude but is also influenced by imperfection distribution. Buckling modes are used for the application of different patterns of imperfection. This intricate relationship is comprehensively illustrated in Figures 3.20 to 3.36. Unlike prior investigations where imperfection patterns were inadequately documented, this study, employing generated models, facilitated the development of new equations. These equations account for the maximum imperfection magnitude in generating buckling factors.

The author underscores the imperative for manufacturers of beams with corrugated webs to consider limitations on imperfection magnitude to meet standard requirements. While time constraints hindered the generation of additional models for further investigation and more precise equation derivation, the author recommends that future research should delve deeper. This involves generating models with diverse dimensions, slenderness ratios, and imperfection magnitudes to formulate equations that not only ensure a safe design but also mitigate the risk of overdesign.

4 References

[1] Leblouba, M., Tabsh, S., Barakat, S. (2020): Reliability-based design of corrugated web steel girders in shear as per AASHTO LRFD. *Journal of Constructional Steel Research*, Vol. 169, March 2020.

[2] Abdel-Basset Ibrahim, S. (2015): Steel Plate Girders with Corrugated Webs, Past Present and Future. ResearchGate.net, April 2015.

[3] Zhou, M., Zhang, J., Zhong, J., Zhao, Y. (2016): Shear Stress Calculation and Distribution in Variable Cross Sections of Box Girders with Corrugated Steel Webs. *Journal of Structural Engineering*, Vol. 142, Issue. 6, Jun 2016.

[4] Sayed-Ahmed, E. (2001): Behavior of steel and (or) composite girders with corrugated steel webs. *Canadian Journal of Civil Engineering*, Vol. 28, August 2001.

[5] Leblouba, M., Barakat, S., Al-Saadon, Z. (2018): Shear behavior of corrugated web panels and sensitivity analysis. *Journal of Structural Engineering*, Vol. 151, Dec 2018.

[6] Kollár, D., Kövesdi, B. (2018): Effect of imperfection and residual stress on the shear buckling strength of corrugated web girders. *Eighth International Conference on Thin-walled structures*, July 2018.

[7] CEN. Eurocode 3: Design of steel structures - Part 1-5: Plated structural elements, upcoming draft, November 2019.

[8] Hassanein, M.F., Kharoob, O.F. (2013): Behavior of bridge girders with corrugated webs: (I) Real boundary condition at the juncture of the web and flanges. *Journal of Structural Engineering*, Vol. 57, Dec 2013.

[9] Hassanein, M.F., Elkawas, A.A., El Hadidy, A.M., Elchalakani, M. (2017): Shear analysis and design of high-strength steel corrugated web girders for bridge design. *Journal of Structural Engineering*, Vol. 146, September 2017.

[10] Johansson, B., Maquoi, R., Sedlacek, G., Müller, C., Beg, D. (2007): *COMMENTARY AND WORKED EXAMPLES TO EN 1993-1-5 "PLATED STRUCTURAL ELEMENTS"*

[11] Deng, H., Shao, Y., Hassanein, M.F. (2021): Experimental shear testing of small-scale corrugated web girders used in conventional buildings. *Journal of Structural Engineering*, Vol. 189, September 2021.

[12] Usman, F. (2014): Shear Resistance of Trapezoidal Corrugated Web in Local Bucling. *Applied Mechanics and Materials*, Vol. 554, Jun 2014.

[13] Gil, H., Lee, H. (2005): Shear Buckling Strength of Trapezoidally Corrugated Steel Webs for Bridges. *Transportation Research Record Journal of the Transportation Research Boar,*. January 2005.

[14] Nie, J., Zhu, L., Tao, M., Tang, L. (2013): Shear strength of trapezoidal corrugated steel webs. *Journal of Structural Engineering*, Vol. 85, Jun 2013.

[15] Moon, J., Yi, J., Choi, B., Lee, H. (2008): Shear strength and design of trapezoidally corrugated steel webs. *Journal of Structural Engineering*, Vol. 65, Issue. 5, May 2009.

[16] Leblouba, M., Barakat, S., Altoubat, S., Junaid, T., Maalej, M. (2017): Normalized shear strength of trapezoidal corrugated steel webs. *Journal of Structural Engineering*, Vol. 136, May 2017.

[17] Sause, R., Abbas, H., Wassef, W., Driver, R., Elgaaly, M. (2003): *Corrugated web girder shape and strength criteria*. Lehigh Preserve Institutional Repository, Bethlehem, September 2003.

[18] Wang, T., Ma, J., Wang, Y. (2021): Normalized shear strength of trapezoidal corrugated steel web dominated by local buckling. *Engineering structures*, Vol. 233, January 2021.

[19] Elamary, A., Taha, I.B.M. (2021): Determining the Shear Capacity of Steel Beams with Corrugated Webs by Using Optimised Regression Learner Techniques, May 2021.

[20] Wang, S., Zhang, K., Zhang, Y., Liu, Y. (2022): Shear failure mechanism of local buckling-dominated large-scale corrugated steel web. *Thin-walled structures*, Vol. 182, January 2023.

[21] Wang, T., Ma, J. (2022): Shear buckling stress and normalized shear strength of trapezoidal corrugated steel web. *Journal of Building Engineering*, Vol. 57, Jun 2022.

[22] Wang, T., Ma, J., Wang, Y. (2021): Normalized shear strength of trapezoidal corrugated steel web dominated by local buckling. *Engineering Structures*. Vol. 233, January 2021.

[23] Amani, M., Al-Emrani, M., Flansbjer, M. (2022): Shear Behavior of Stainless Steel Girders with Corrugated Webs. *Stainless Steel in Structures – Sixth International Experts Seminar*. London, UK, Sep 2022.

[24] Paik, J., Kim, KJ., Lee, JH., Jung, BJ., Kim, SJ. (2017): Test database of the mechanical properties of mild, high-tensile and stainless steel and aluminium alloy associated with cold temperatures and strain rates.

5 Appendix-A

In order to provide material for future investigation, in following figures indicate critical buckling modes for each imperfection magnitude, as well out of plane deflection and Von Mises stresses in maximum load increment.

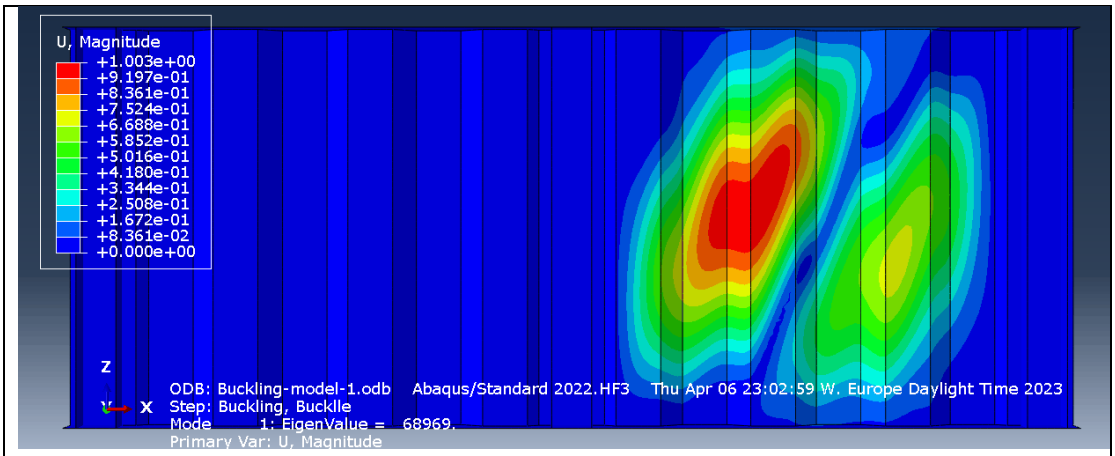

Figure 5.1 Buckling mode 1 for model-1 which is critical for failure with imperfection equal to $\frac{a_{max}}{200}$ *and* $\frac{h_w}{200}$.

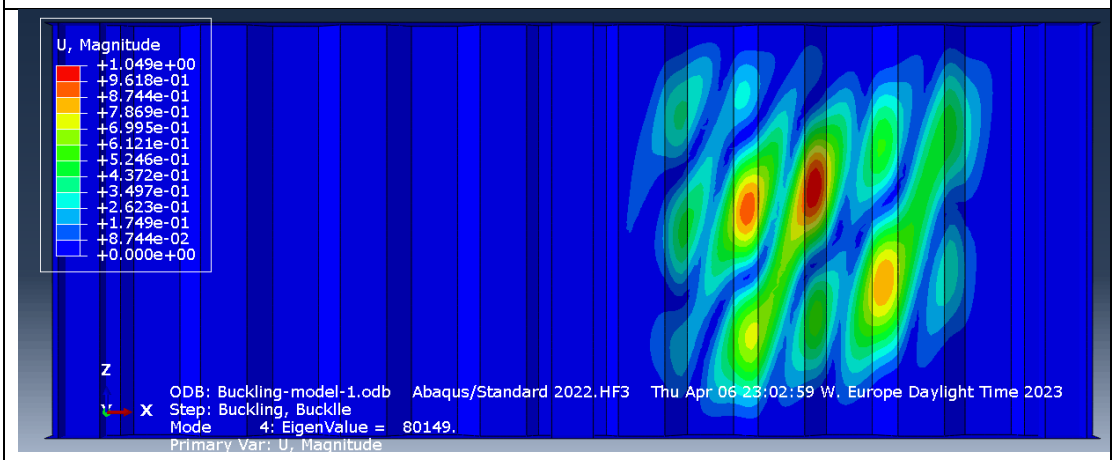

Figure 5.2 Buckling mode 4 for model-1 which is critical for failure with imperfection equal to t_{w1}.

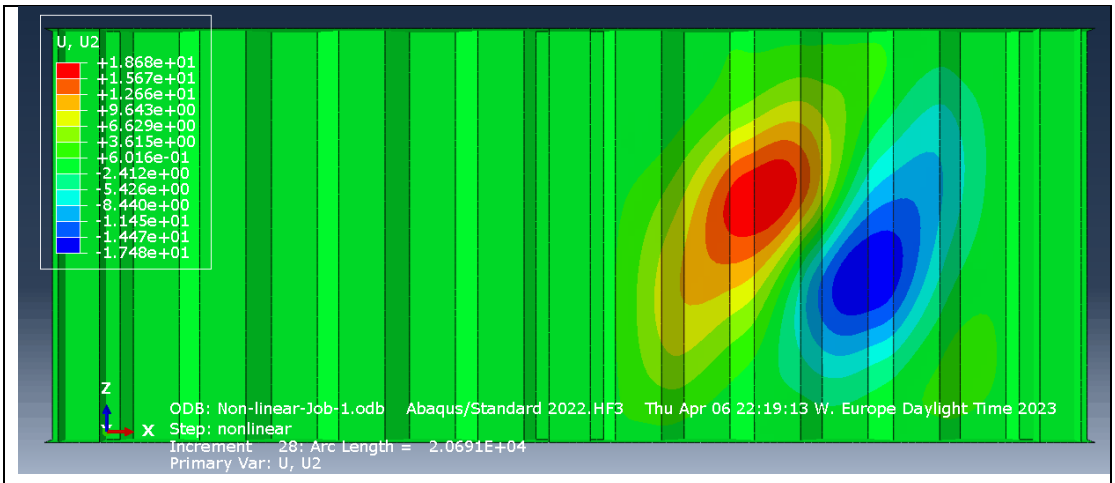

Figure 5.3 *Out of plane deflection for model-1 in failure increment with imperfection equal to* $\frac{a_{max}}{200}$.

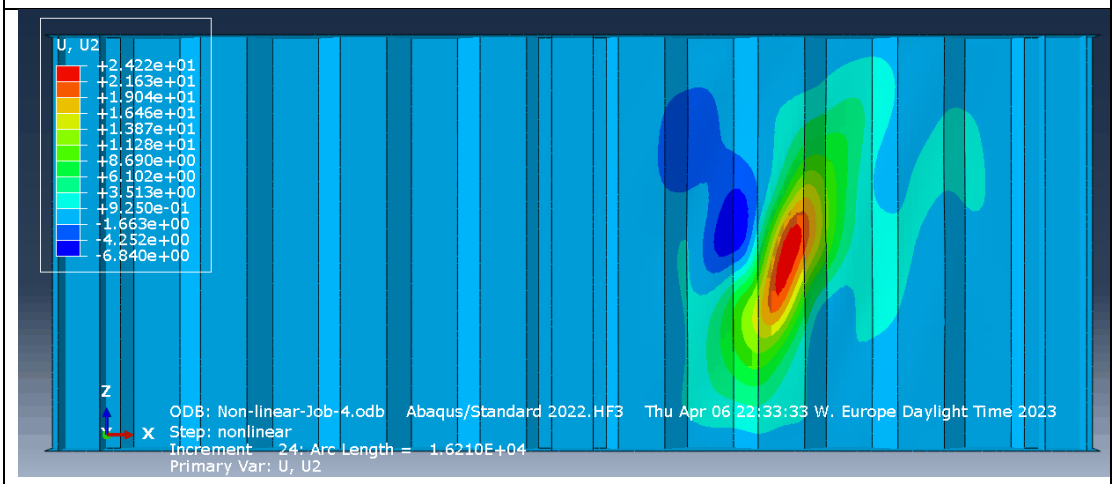

Figure 5.4 *Out of plane deflection for model-1 in failure increment with imperfection equal to* t_{w1}.

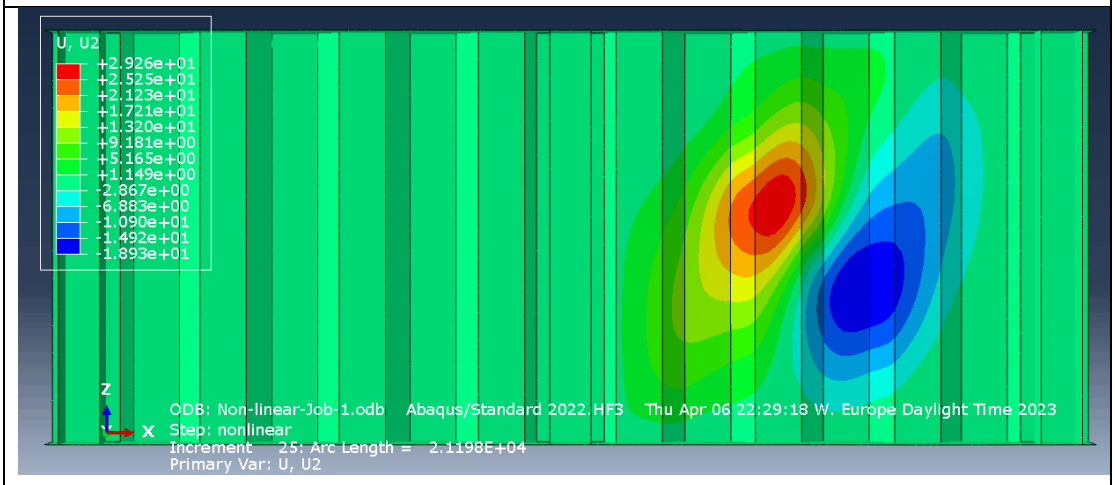

Figure 5.5 *Out of plane deflection for model-1 in failure increment with imperfection equal to* $\frac{h_w}{200}$.

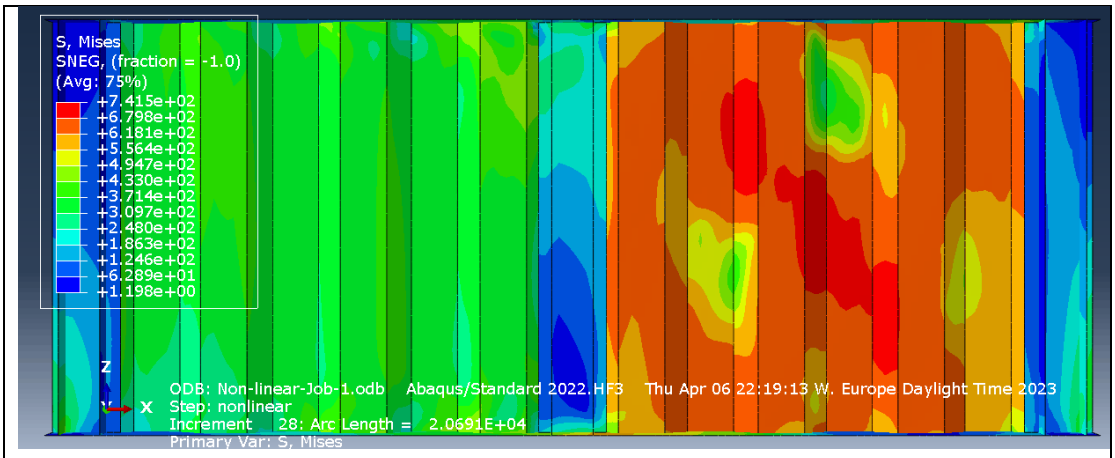

Figure 5.6 Maximum load increment for model-1 with imperfection equal to $\frac{a_{max}}{200}$.

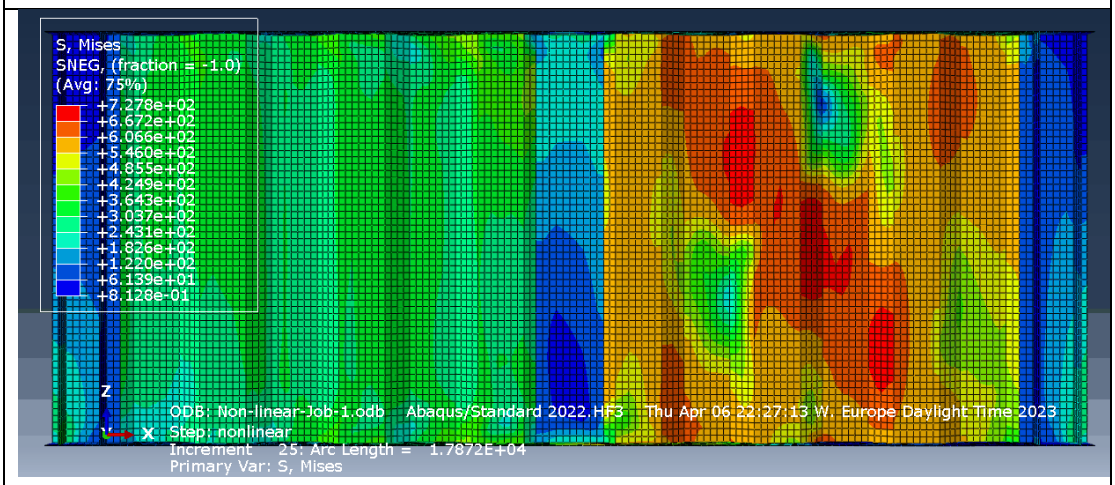

Figure 5.7 Maximum load increment for model-1 with imperfection equal to $\frac{h_w}{200}$.

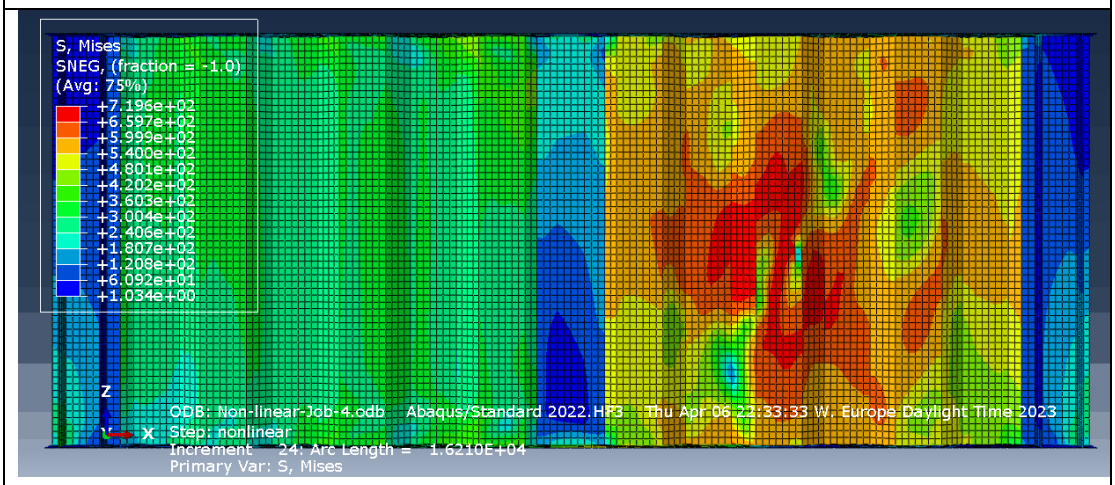

Figure 5.8 Maximum load increment for model-1 with imperfection equal to t_{w1}.

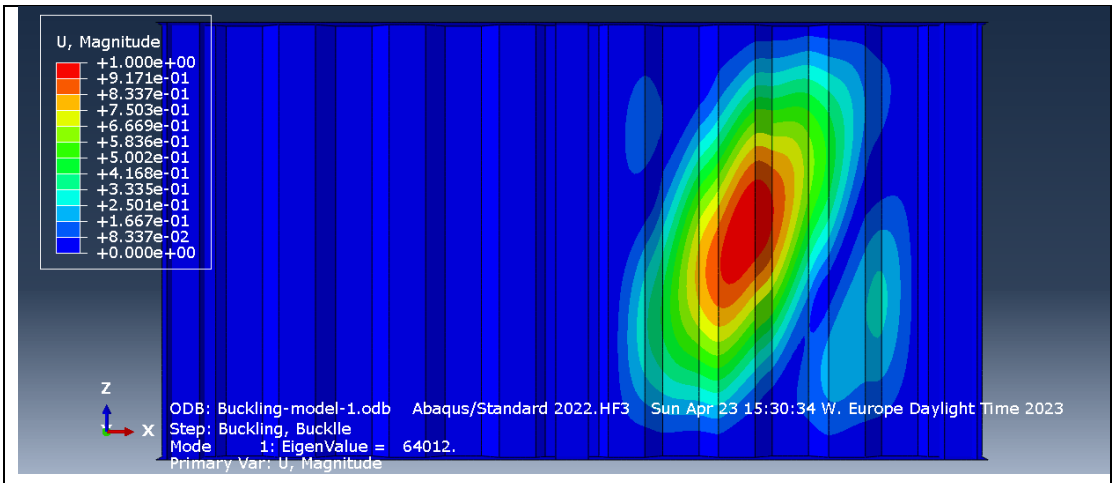

Figure 5.9 *Buckling mode 1 for model-2 which is critical for failure with imperfection equal to* $\frac{a_{max}}{200}$.

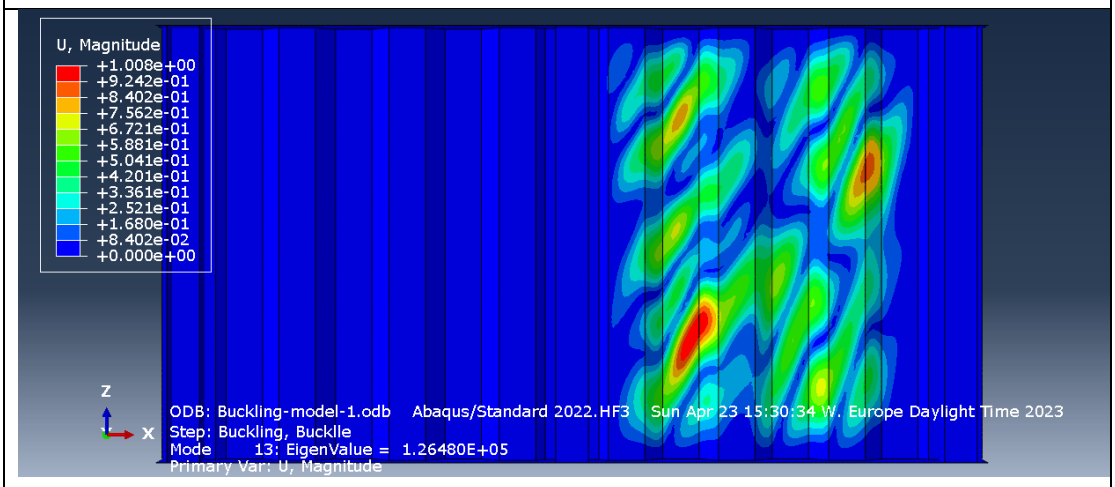

Figure 5.10 *Buckling mode 13 for model-2 which is critical for failure with imperfection equal to* t_{w1} *and* $\frac{h_w}{200}$.

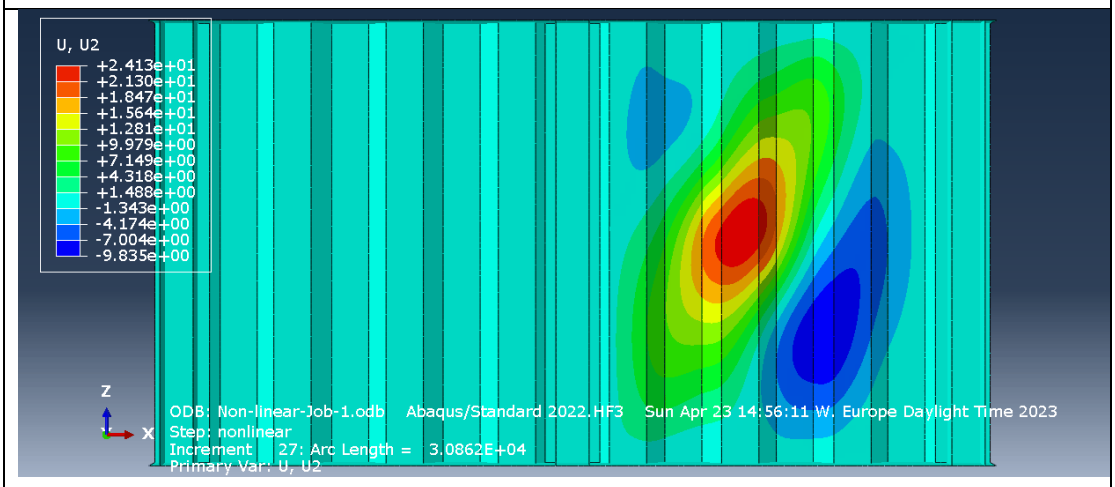

Figure 5.11 *Out of plane deflection for model-2 in failure increment with imperfection equal to* $\frac{a_{max}}{200}$.

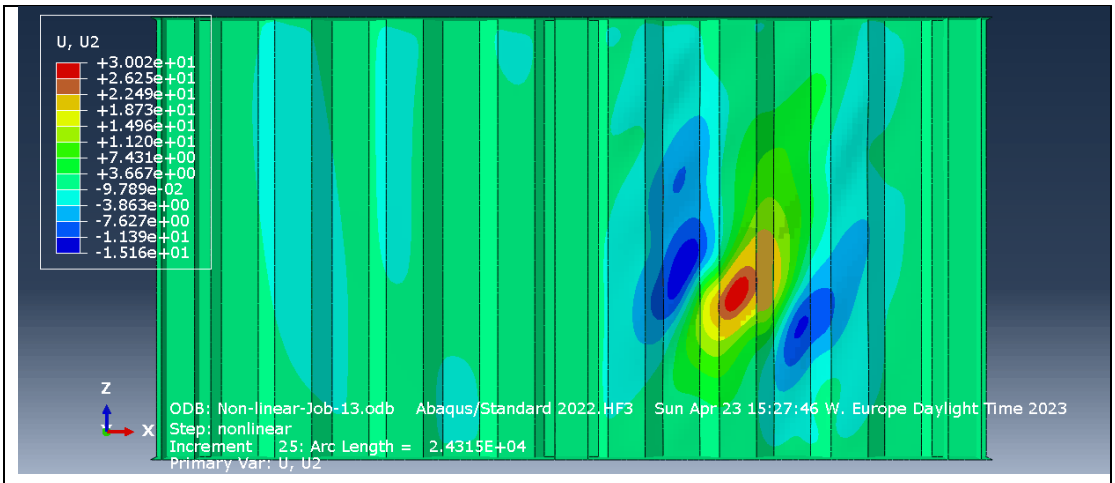

Figure 5.12 *Out of plane deflection for model-2 in failure increment with imperfection equal to* t_{w1}.

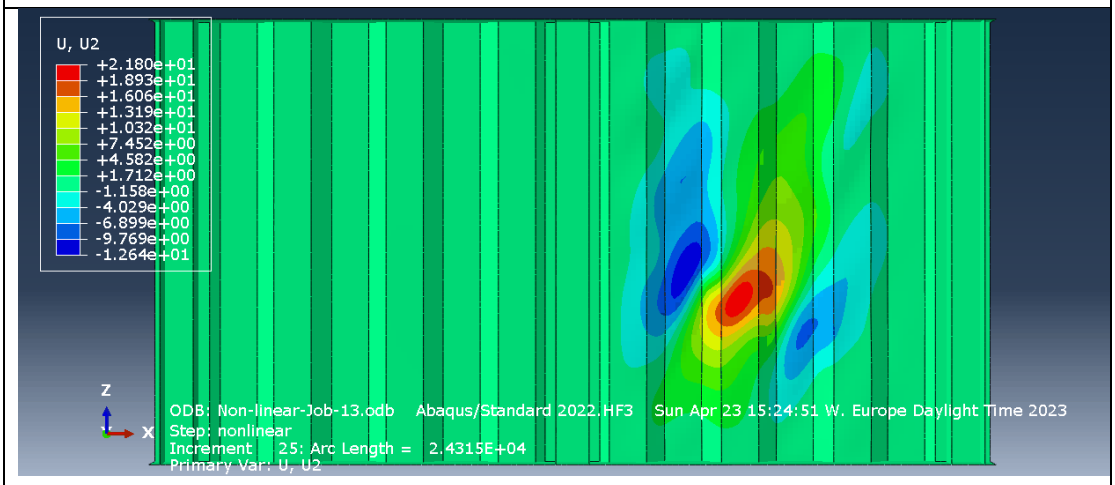

Figure 5.13 *Out of plane deflection for model-2 in failure increment with imperfection equal to* $\frac{h_w}{200}$.

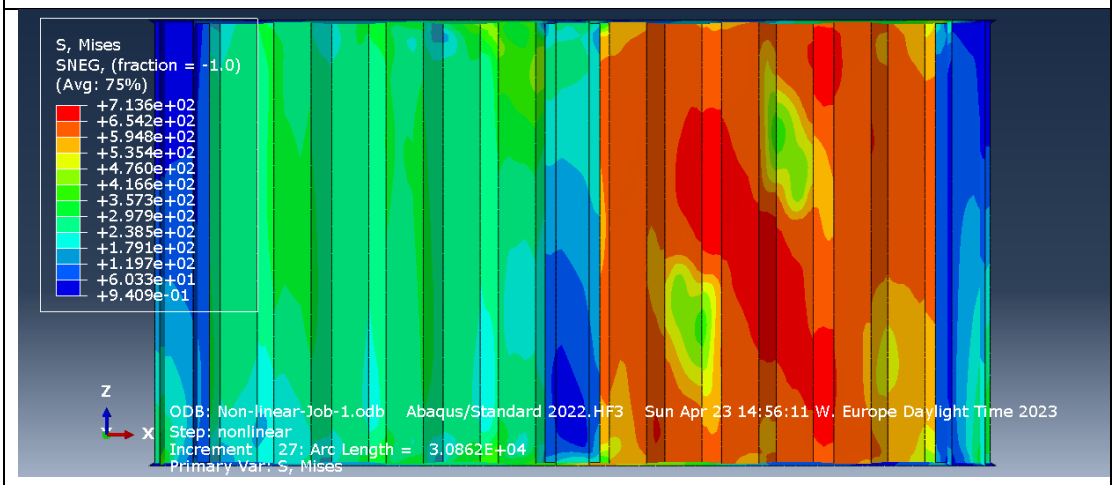

Figure 5.14 *Maximum load increment for model-2 with imperfection equal to* $\frac{a_{max}}{200}$.

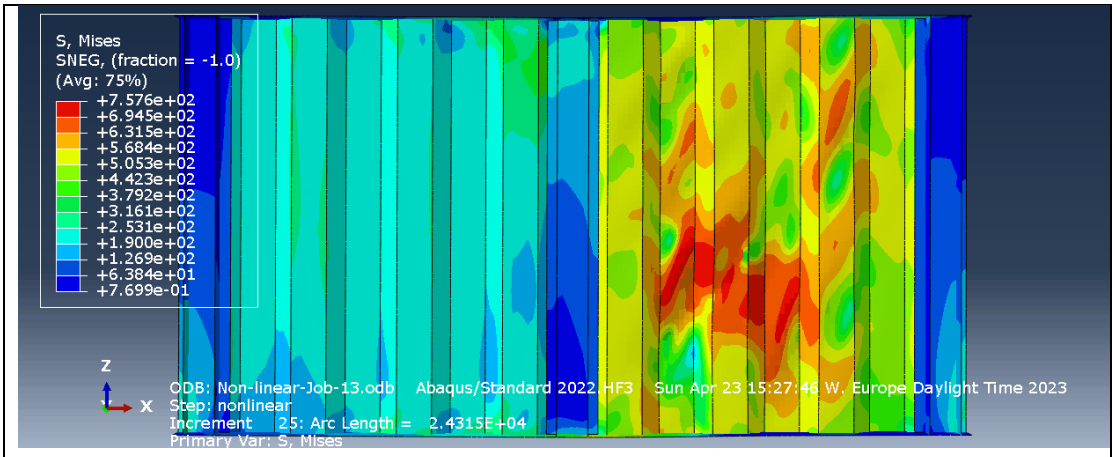

Figure 5.15 Maximum load increment for model-2 with imperfection equal to t_{w1}.

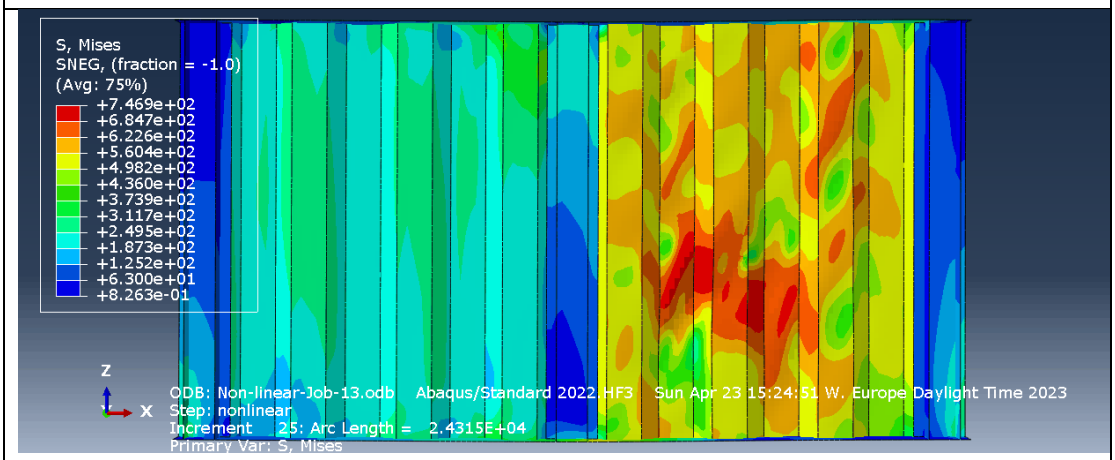

Figure 5.16 Maximum load increment for model-2 with imperfection equal to $\frac{h_w}{200}$.

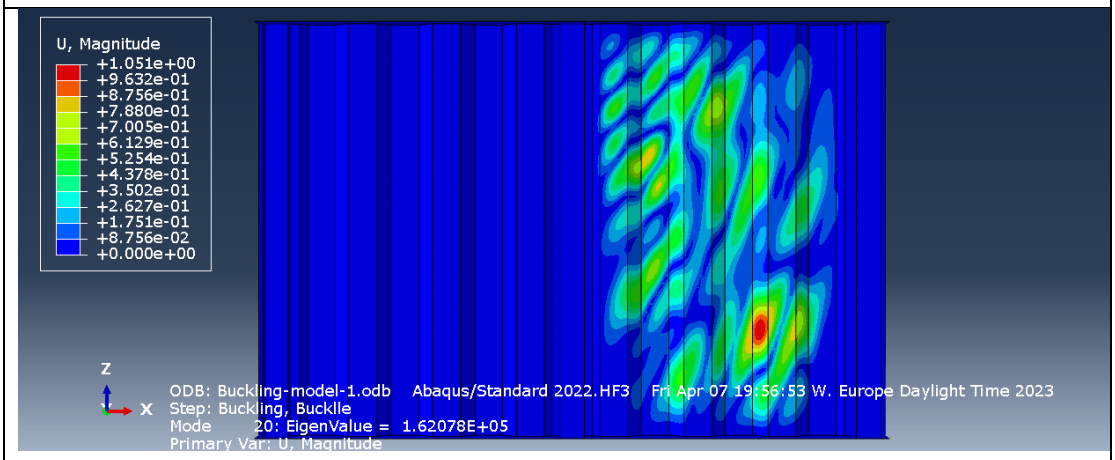

Figure 5.17 Buckling mode 20 for model-3 which is critical for failure with imperfection equal to $\frac{a_{max}}{200}$.

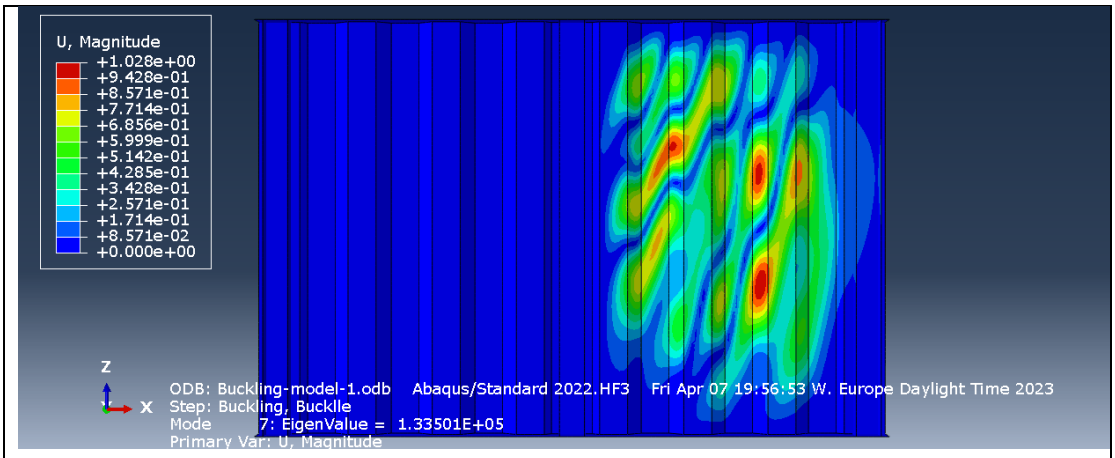

Figure 5.18 *Buckling mode 7 for model-3 which is critical for failure with imperfection equal to* $\frac{h_w}{200}$.

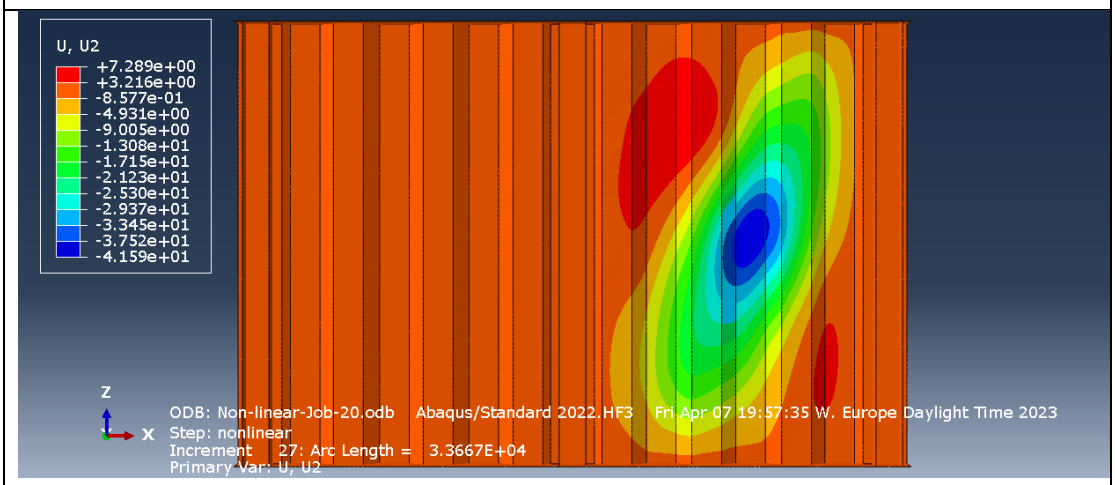

Figure 5.19 *Out of plane deflection for model-3 in failure increment with imperfection equal to* $\frac{a_{max}}{200}$.

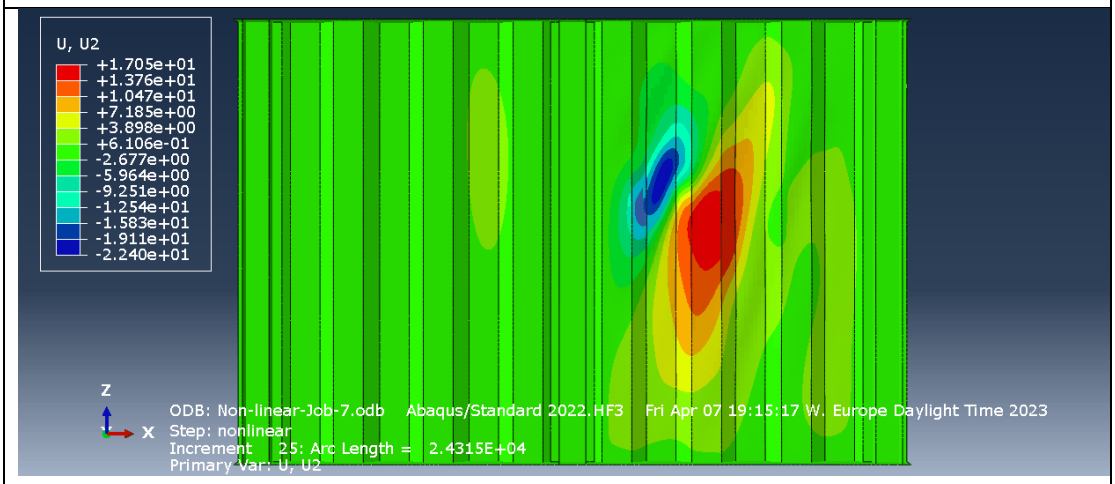

Figure 5.20 *Out of plane deflection for model-3 in failure increment with imperfection equal to* $\frac{h_w}{200}$.

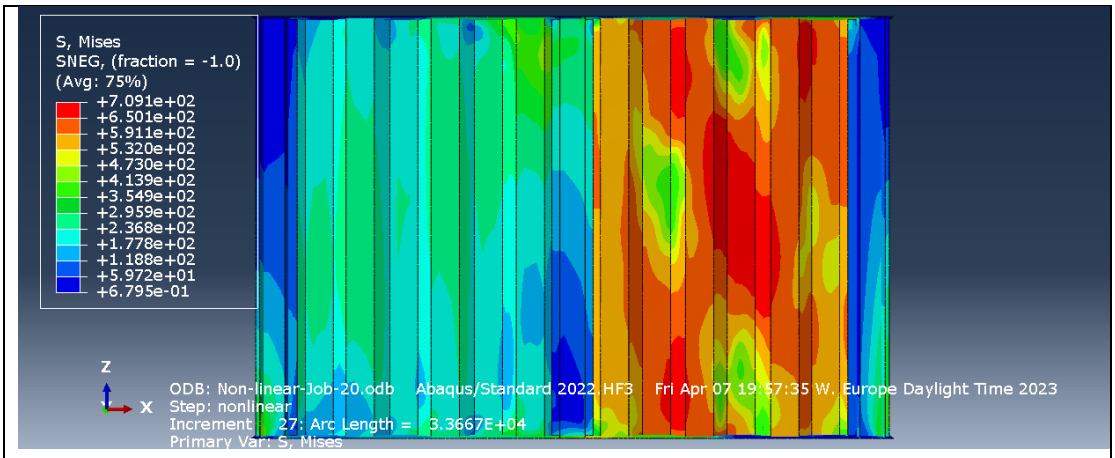

Figure 5.21 Maximum load increment for model-3 with imperfection equal to $\frac{a_{max}}{200}$.

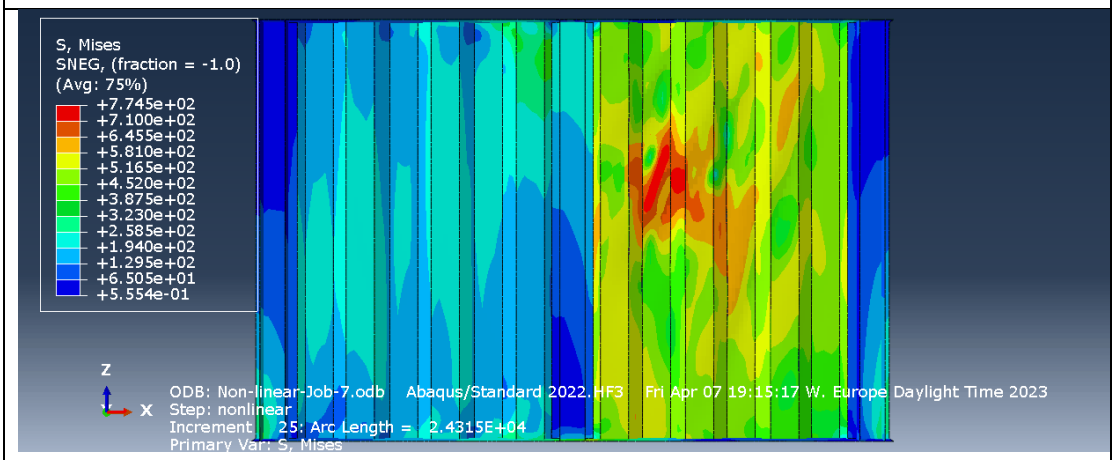

Figure 5.22 Maximum load increment for model-3 with imperfection equal to $\frac{h_w}{200}$.

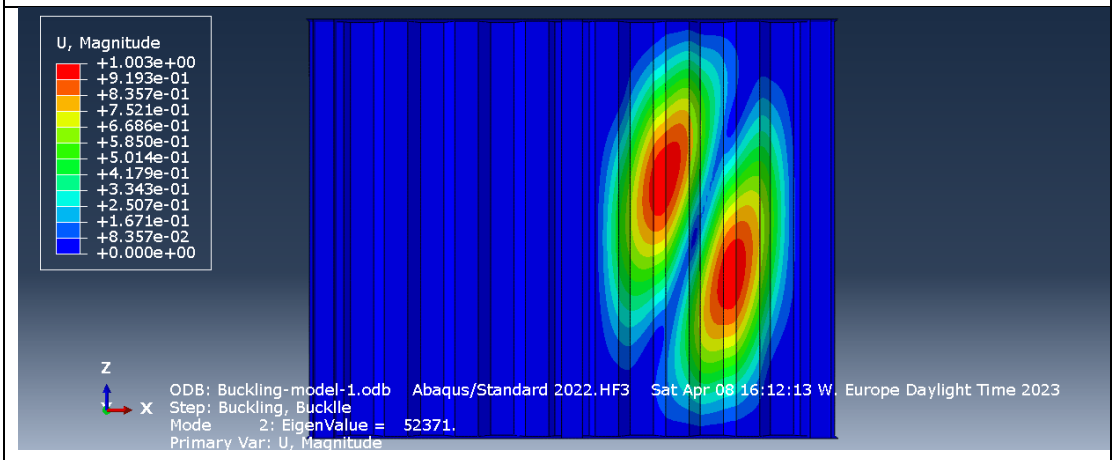

Figure 5.23 Buckling mode 2 for model-4 which is critical for failure with imperfection equal to $\frac{a_{max}}{200}$, t_{w1} *and* $\frac{h_w}{200}$.

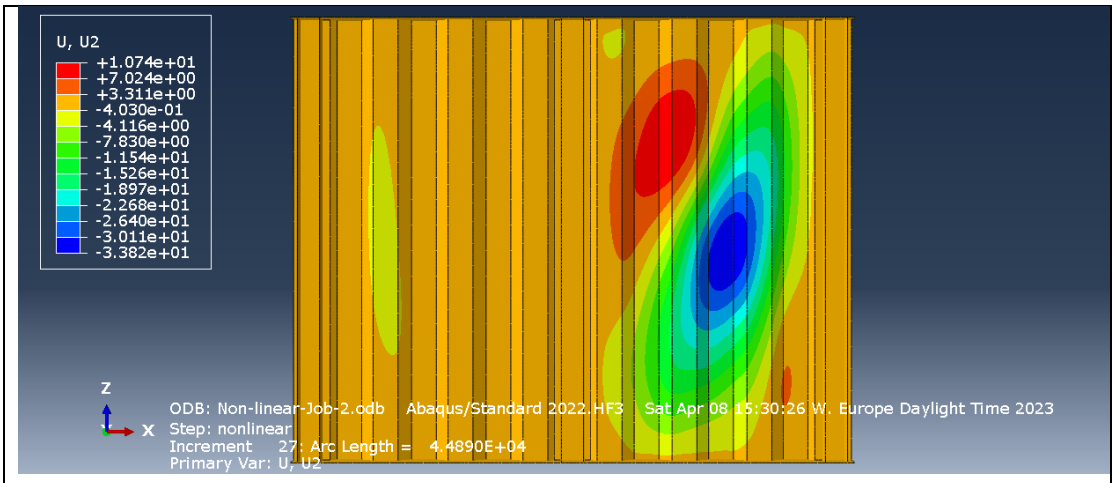

Figure 5.24 *Out of plane deflection for model-4 in failure increment with imperfection equal to* $\frac{a_{max}}{200}$.

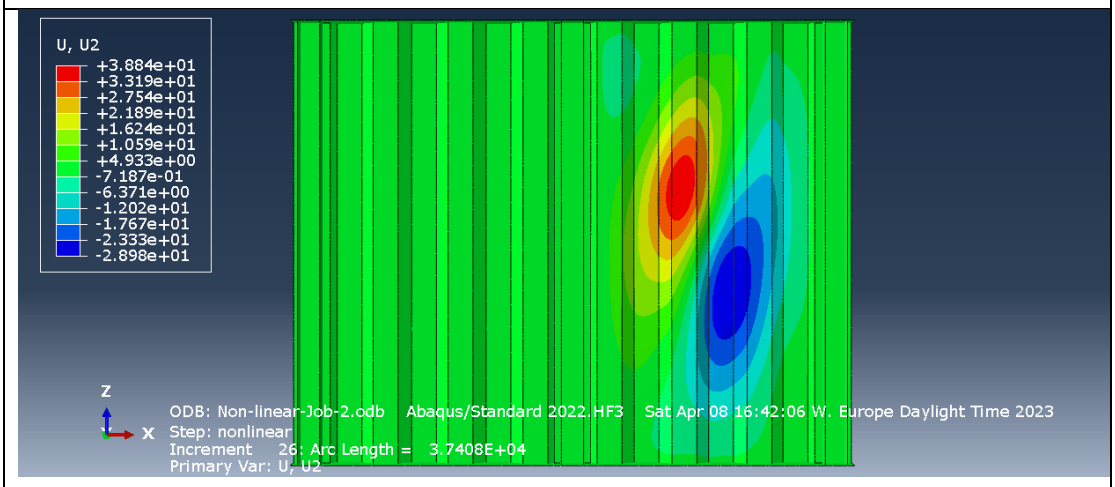

Figure 5.25 *Out of plane deflection for model-4 in failure increment with imperfection equal to* t_{w1}.

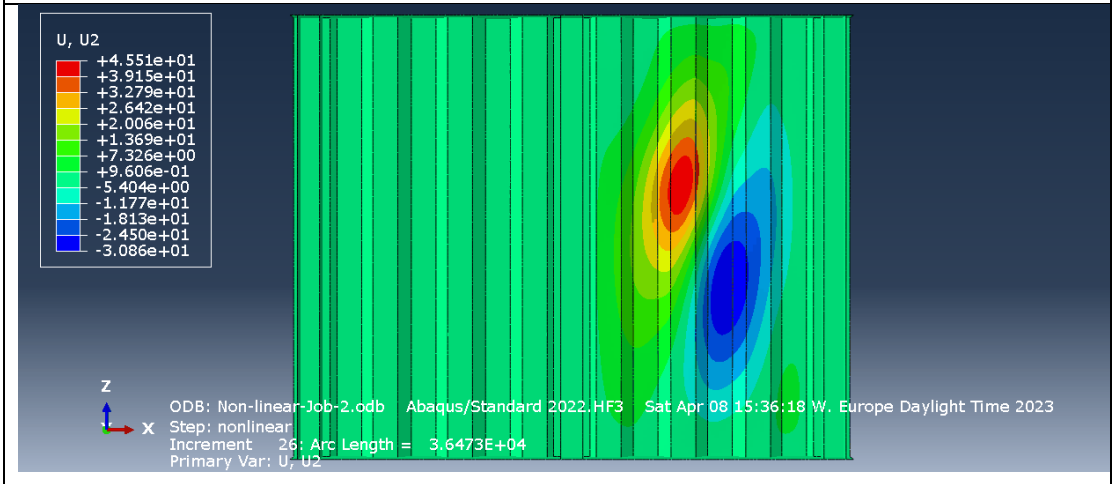

Figure 5.26 *Out of plane deflection for model-4 in failure increment with imperfection equal to* $\frac{h_w}{200}$.

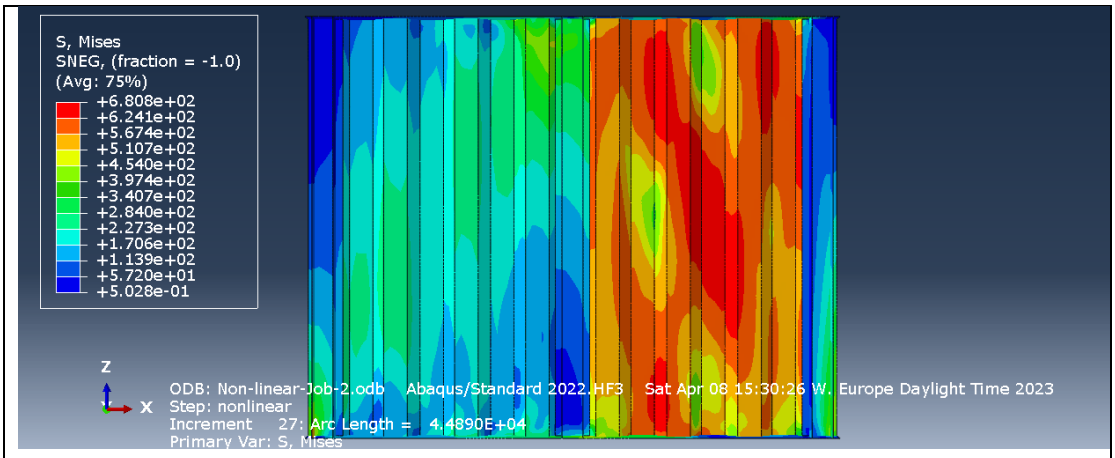

Figure 5.27 Maximum load increment for model-4 with imperfection equal to $\frac{a_{max}}{200}$.

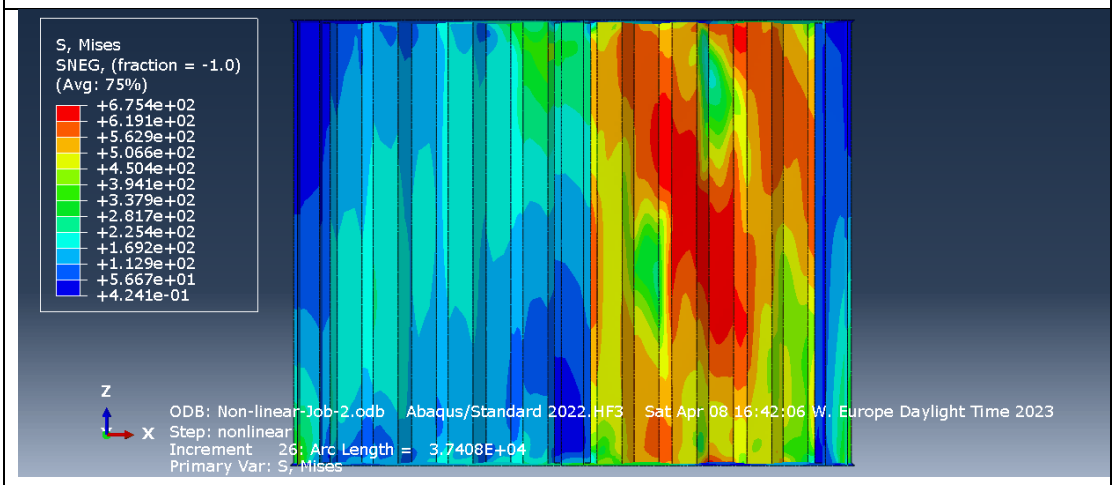

Figure 5.28 Maximum load increment for model-4 with imperfection equal to t_{w1}.

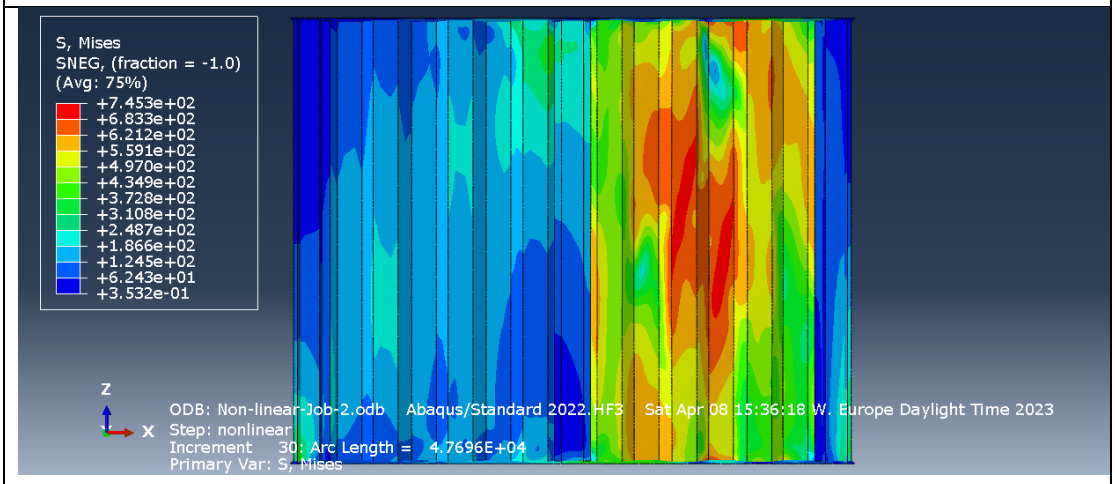

Figure 5.29 Maximum load increment for model-4 with imperfection equal to $\frac{h_w}{200}$.

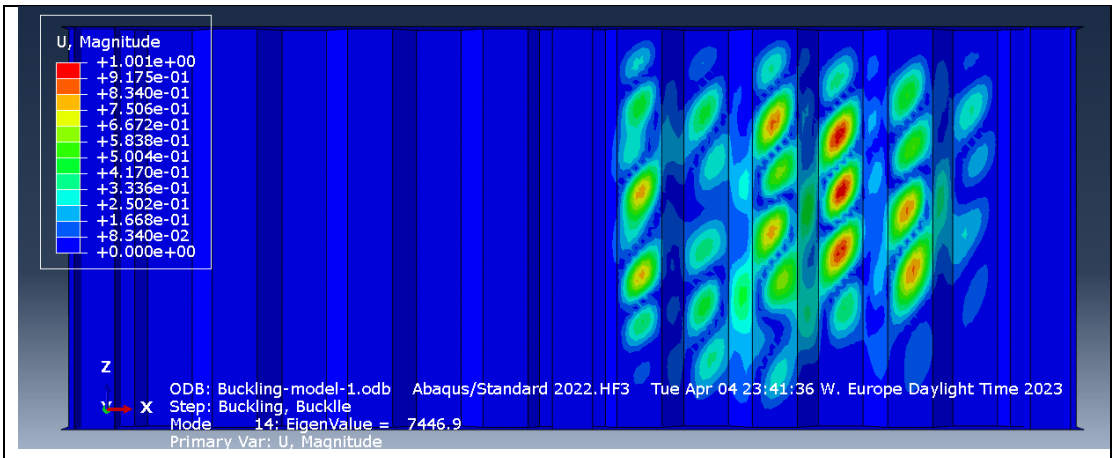

Figure 5.30 Buckling mode 14 for model-5 which is critical for failure with imperfection equal to $\frac{a_{max}}{200}$.

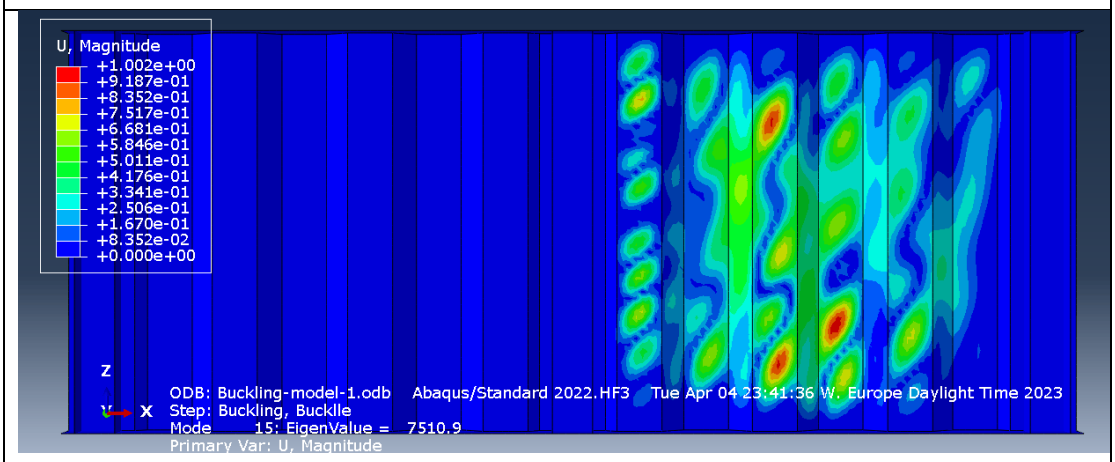

Figure 5.31 Buckling mode 15 for model-5 which is critical for failure with imperfection equal to t_{w1} .

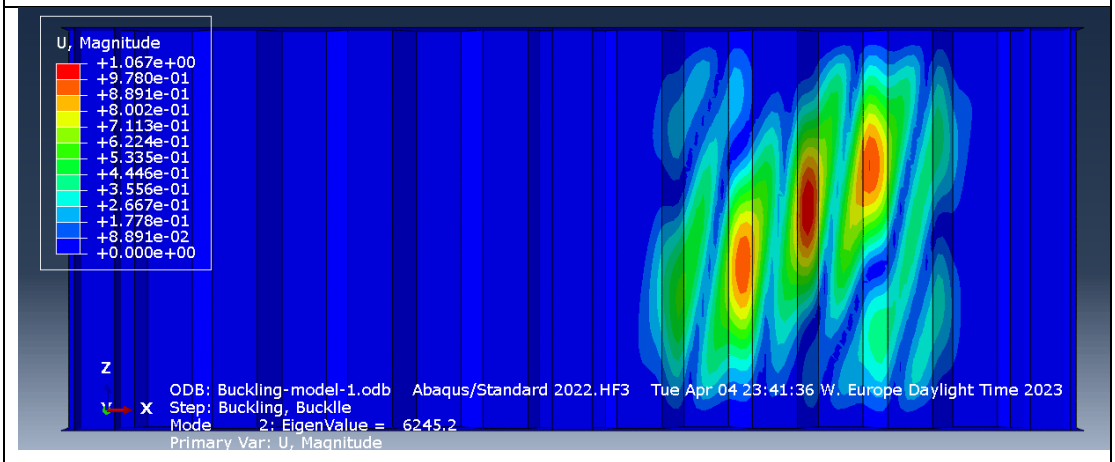

Figure 5.32 Buckling mode 2 for model-5 which is critical for failure with imperfection equal to $\frac{h_w}{200}$.

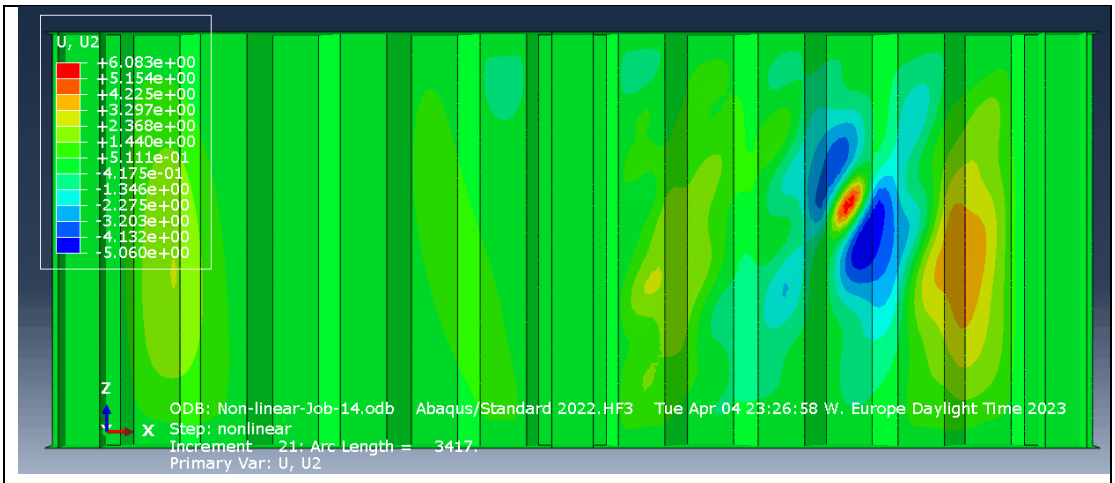

Figure 5.33 *Out of plane deflection for model-5 in failure increment with imperfection equal to* $\frac{a_{max}}{200}$.

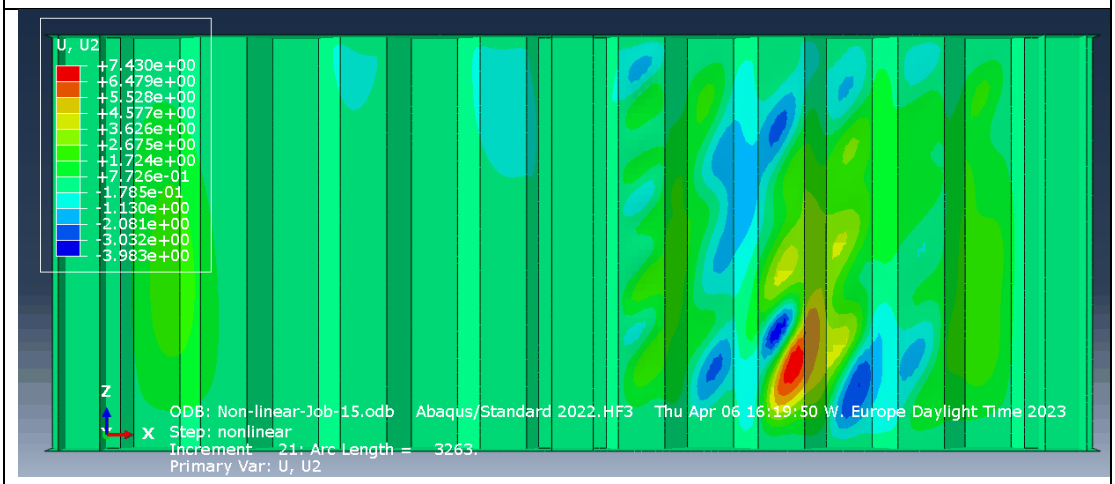

Figure 5.34 *Out of plane deflection for model-5 in failure increment with imperfection equal to* t_{w1}.

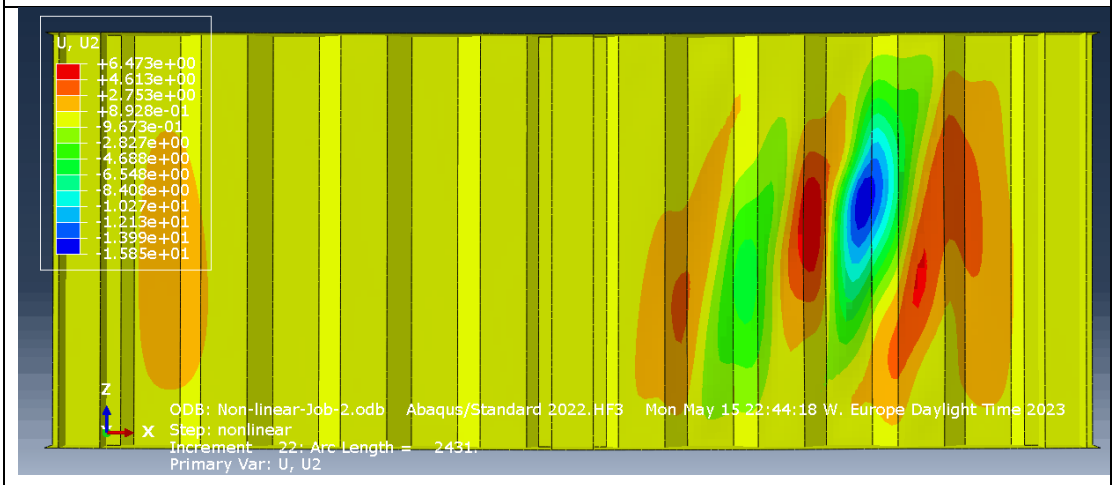

Figure 5.35 *Out of plane deflection for model-5 in failure increment with imperfection equal to* $\frac{h_w}{200}$.

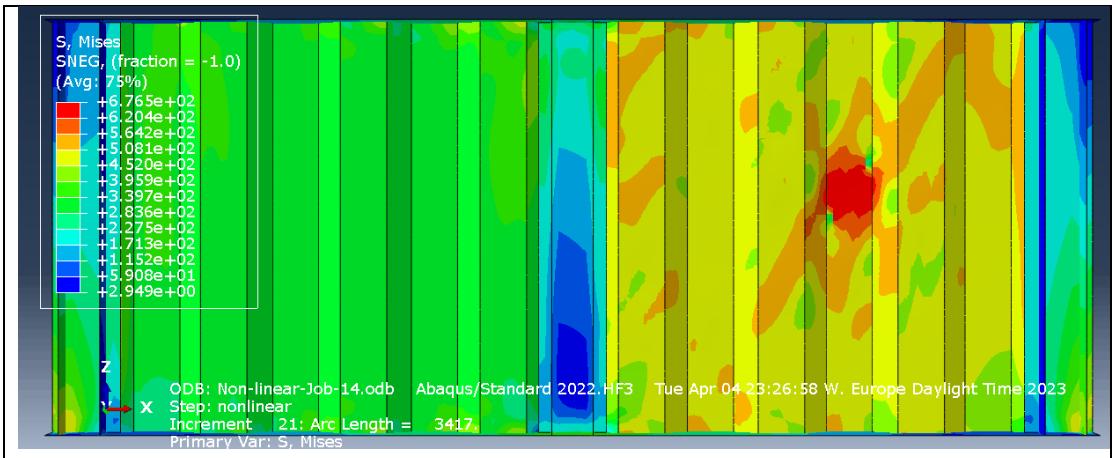

Figure 5.36 Maximum load increment for model-5 with imperfection equal to $\frac{a_{max}}{200}$.

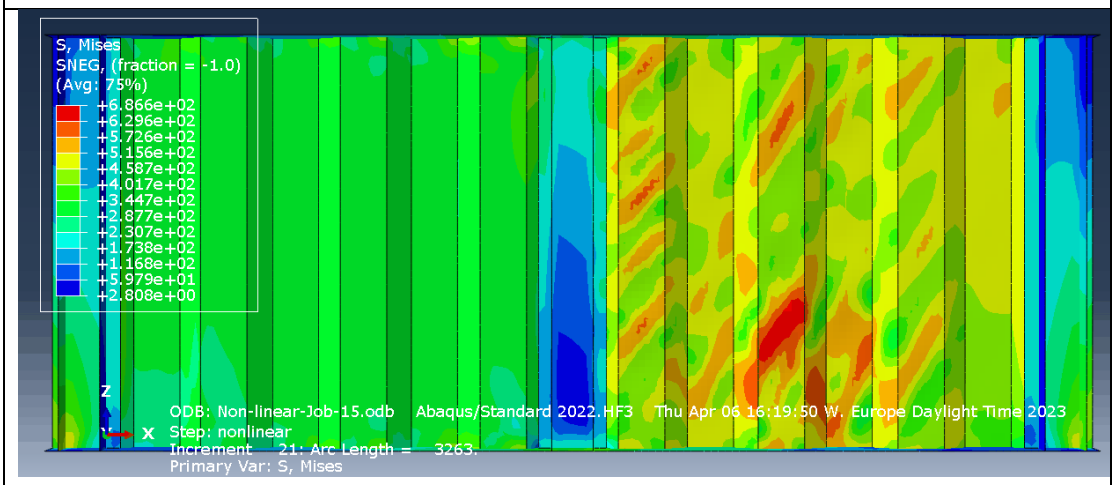

Figure 5.37 Maximum load increment for model-5 with imperfection equal to t_{w1}.

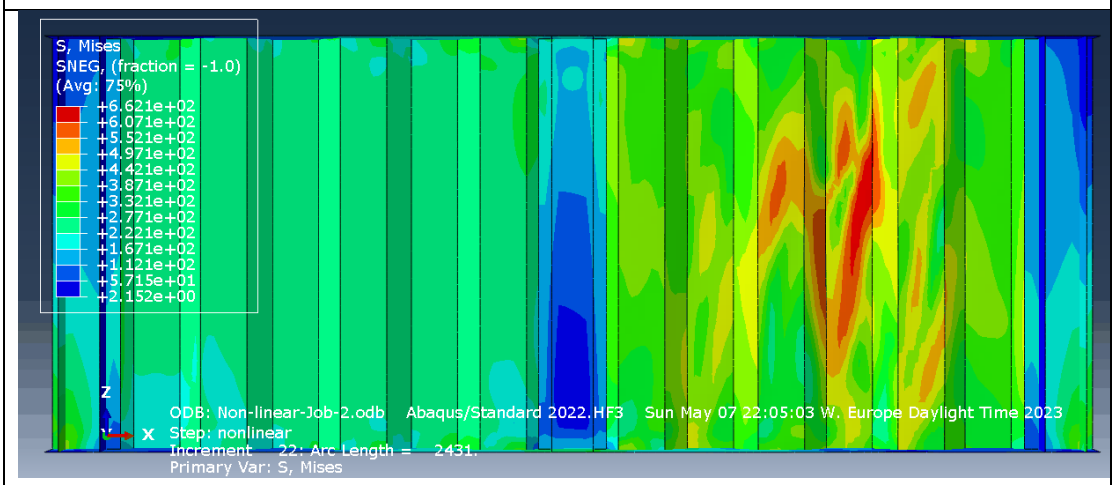

Figure 5.38 Maximum load increment for model-5 with imperfection equal to $\frac{h_w}{200}$.

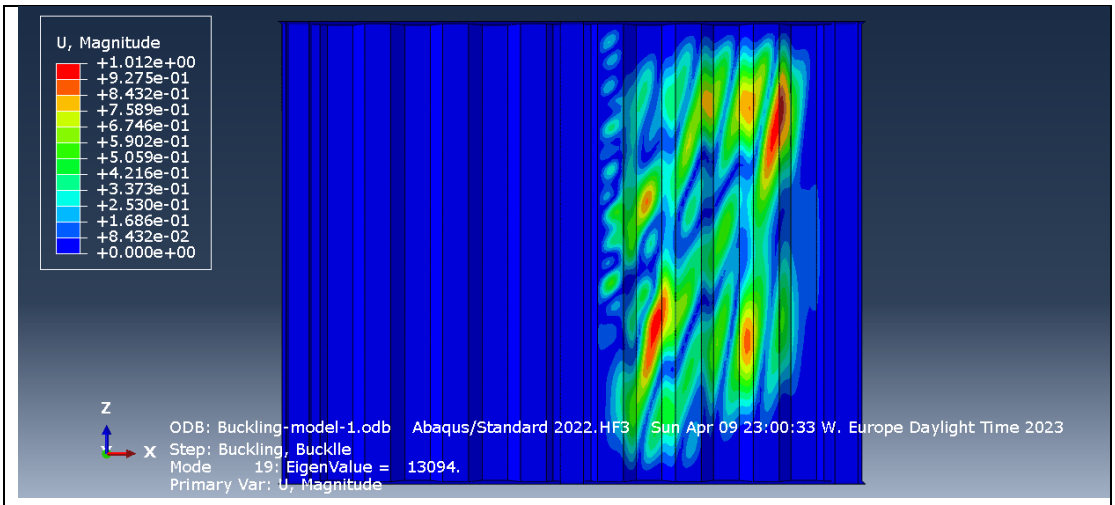

Figure 5.39 Buckling mode 19 for model-6 which is critical for failure with imperfection equal to $\frac{a_{max}}{200}$.

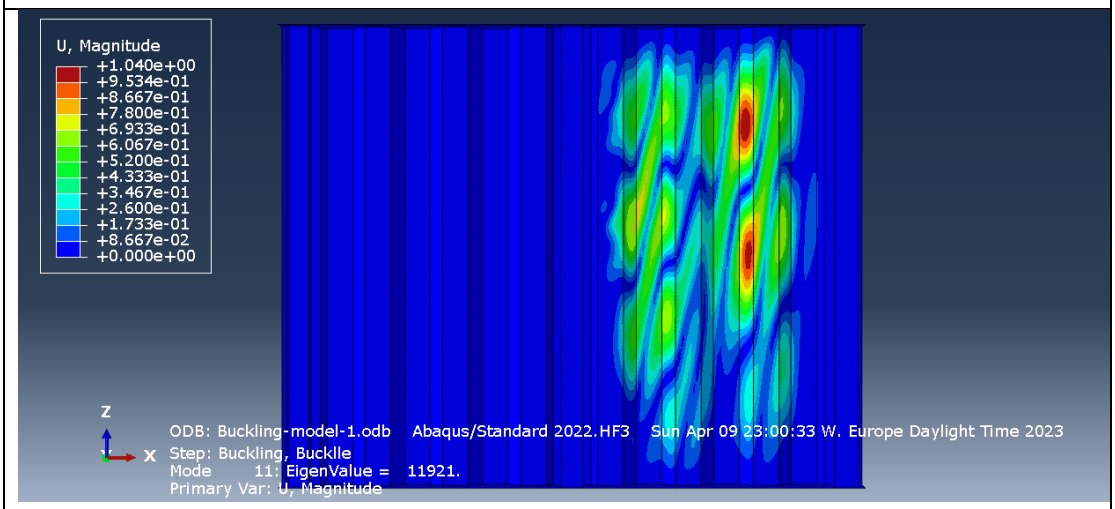

Figure 5.40 Buckling mode 11 for model-6 which is critical for failure with imperfection equal to t_{w1} *and* $\frac{h_w}{200}$.

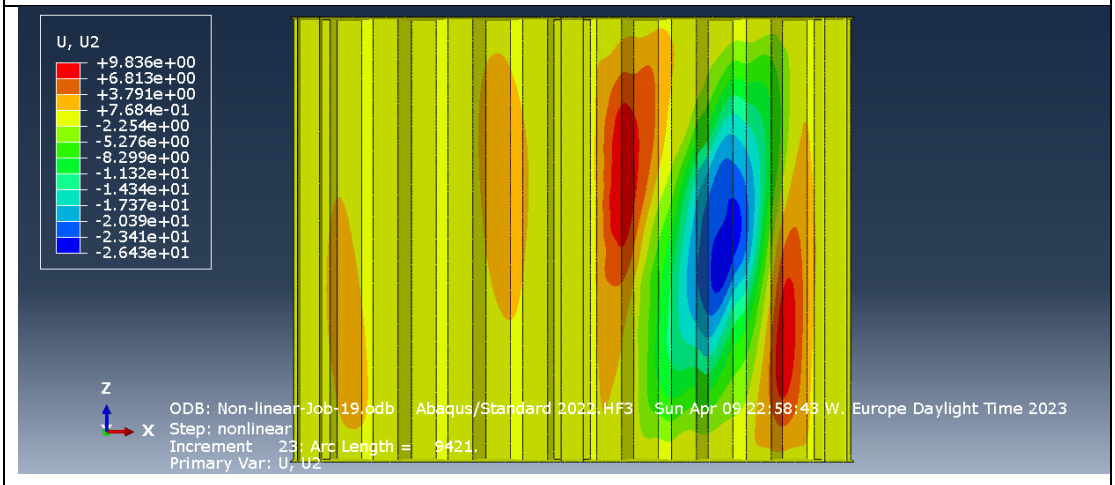

Figure 5.41 Out of plane deflection for model-6 in failure increment with imperfection equal to $\frac{a_{max}}{200}$.

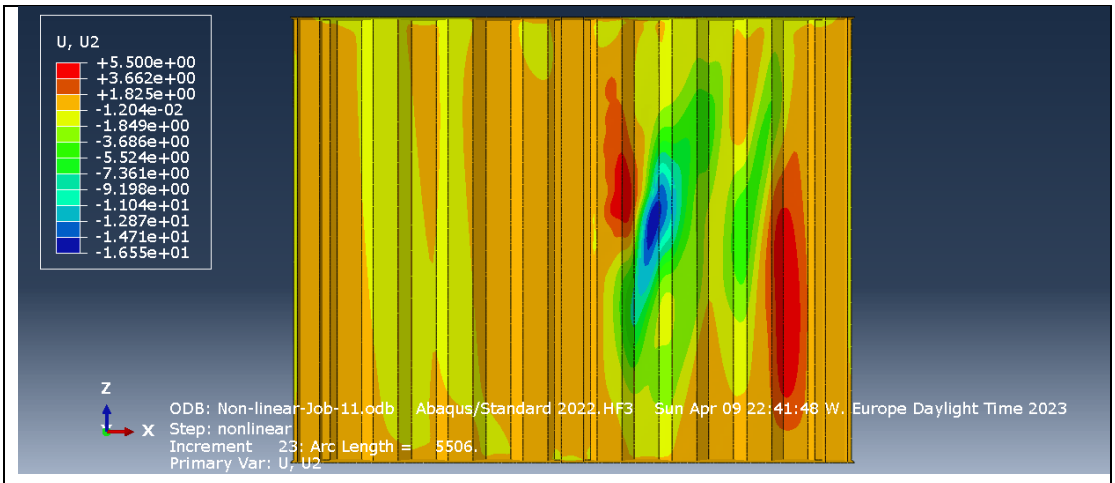

Figure 5.42 *Out of plane deflection for model-6 in failure increment with imperfection equal to* t_{w1}.

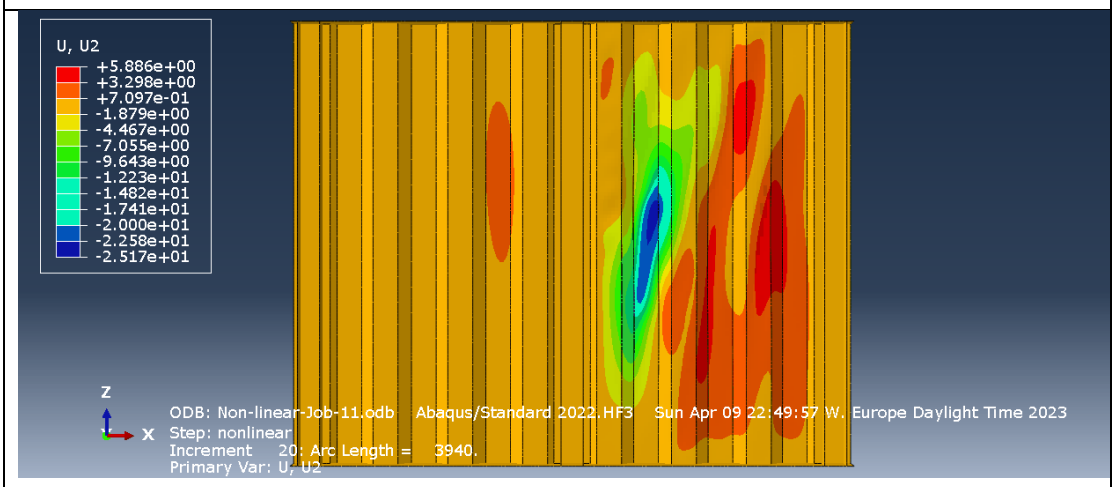

Figure 5.43 *Out of plane deflection for model-6 in failure increment with imperfection equal to* $\frac{h_w}{200}$.

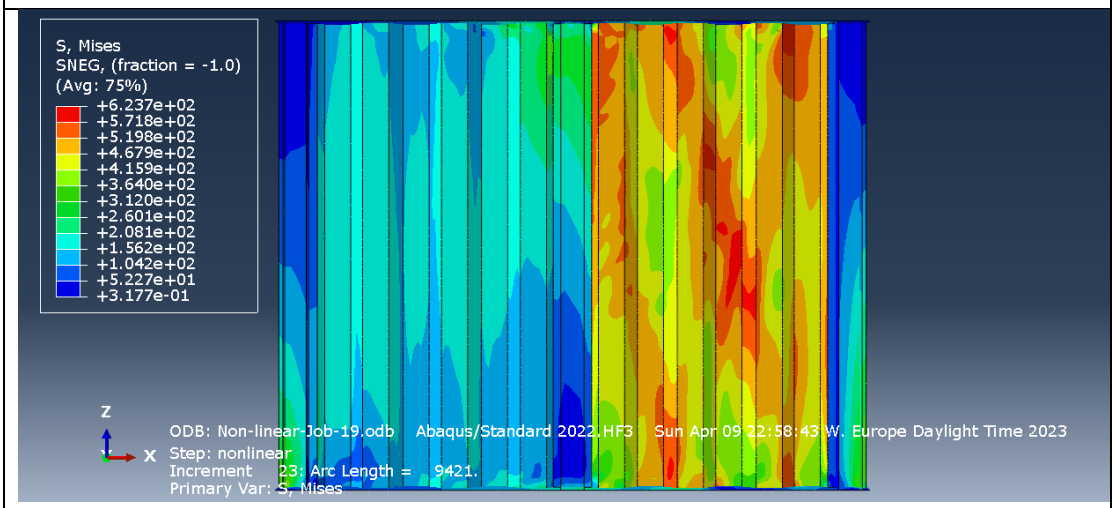

Figure 5.44 *Maximum load increment for model-6 with imperfection equal to* $\frac{a_{max}}{200}$.

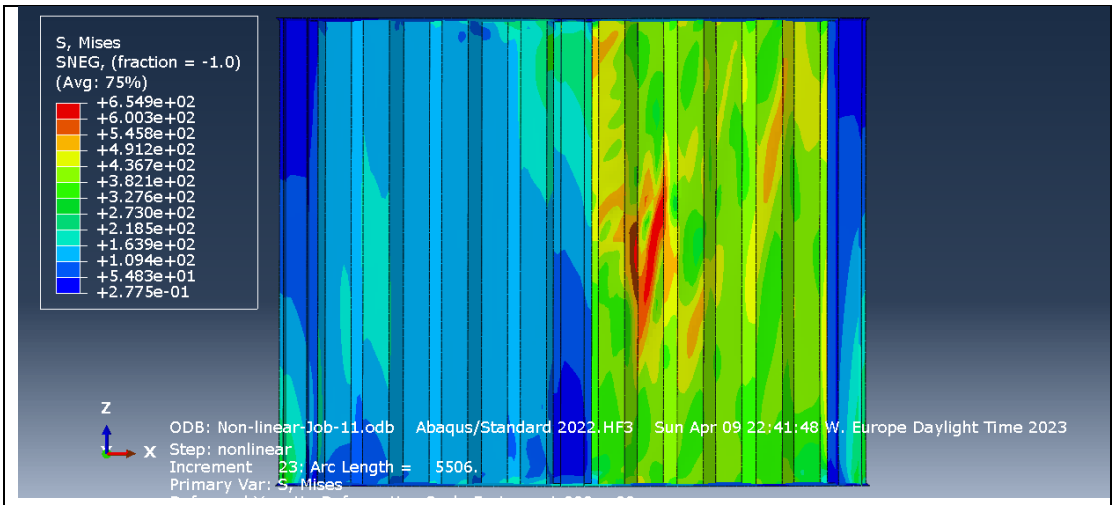

Figure 5.45 Maximum load increment for model-6 with imperfection equal to t_{w1} .

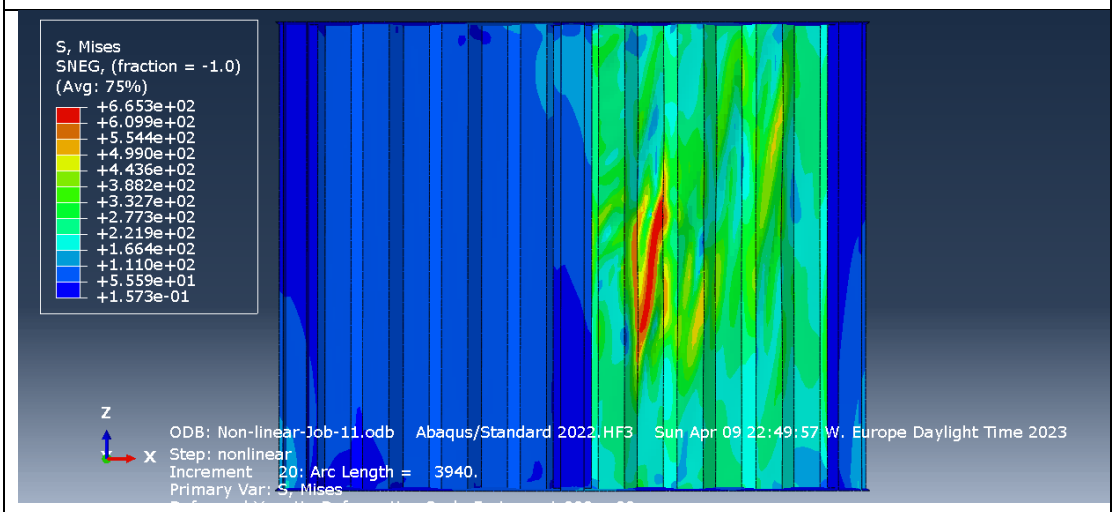

Figure 5.46 Maximum load increment for model-6 with imperfection equal to $\frac{h_w}{200}$.

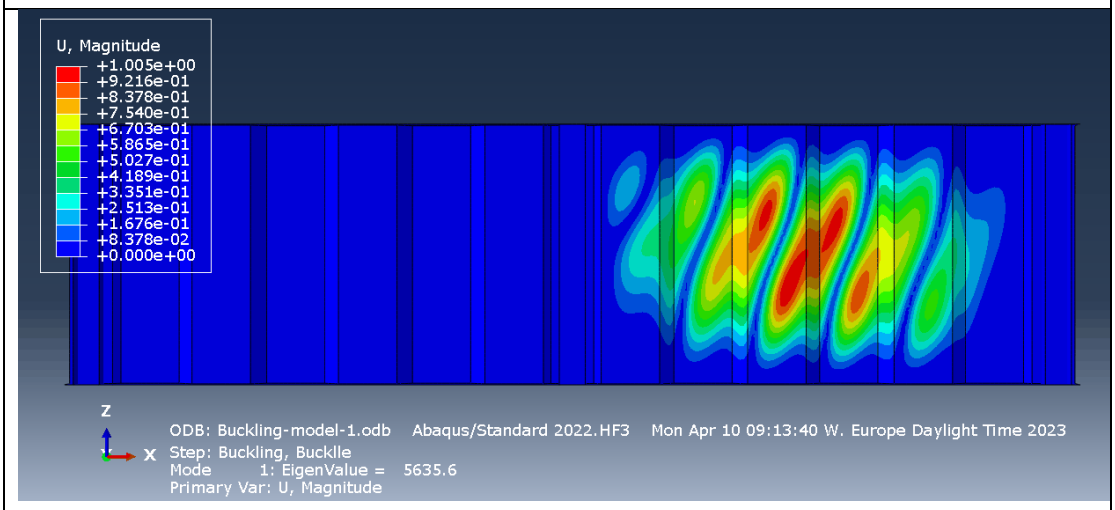

Figure 5.47 Buckling mode 1 for model-7 which is critical for failure with imperfection equal to $\frac{a_{max}}{200}$, t_{w1} *and* $\frac{h_w}{200}$.

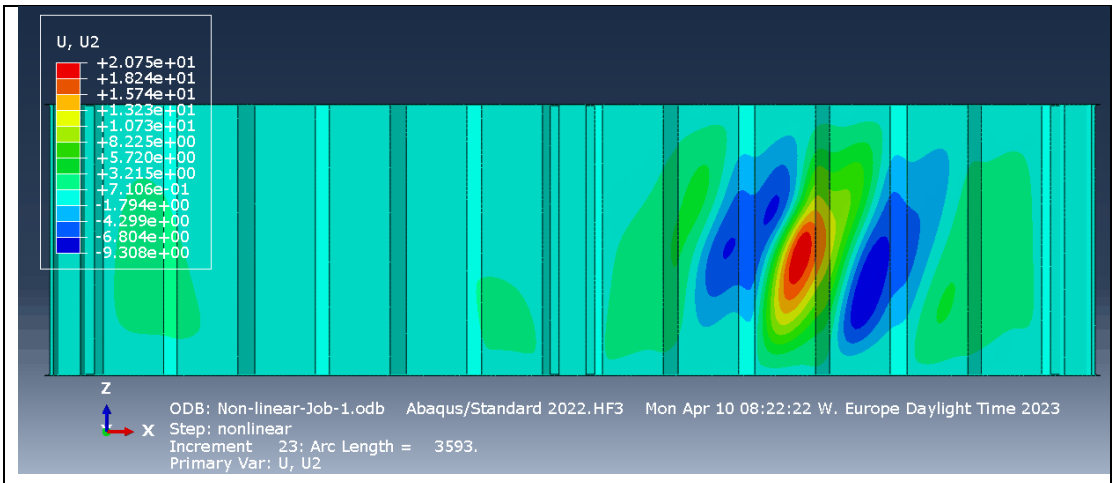

Figure 5.48 *Out of plane deflection for model-7 in failure increment with imperfection equal to* $\frac{a_{max}}{200}$.

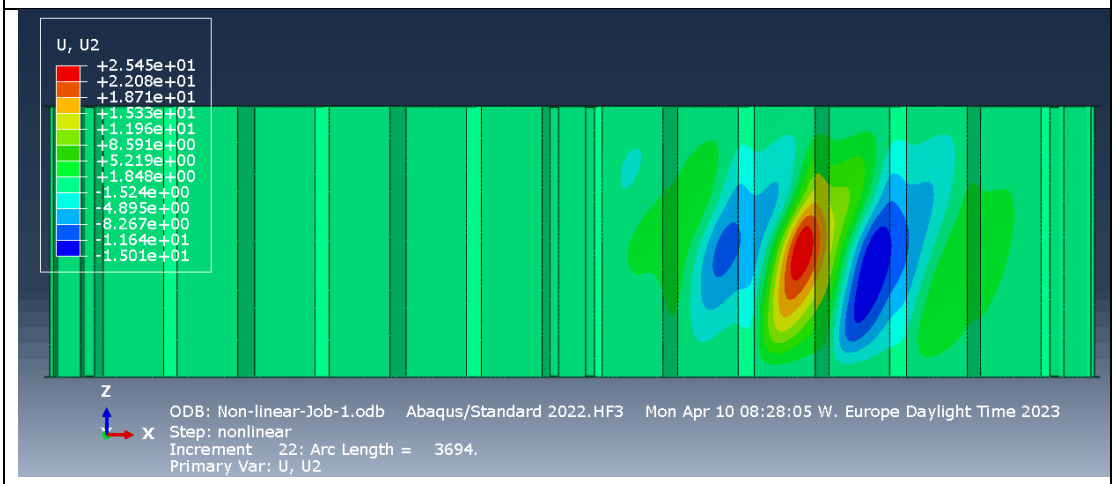

Figure 5.49 *Out of plane deflection for model-7 in failure increment with imperfection equal to* t_{w1}.

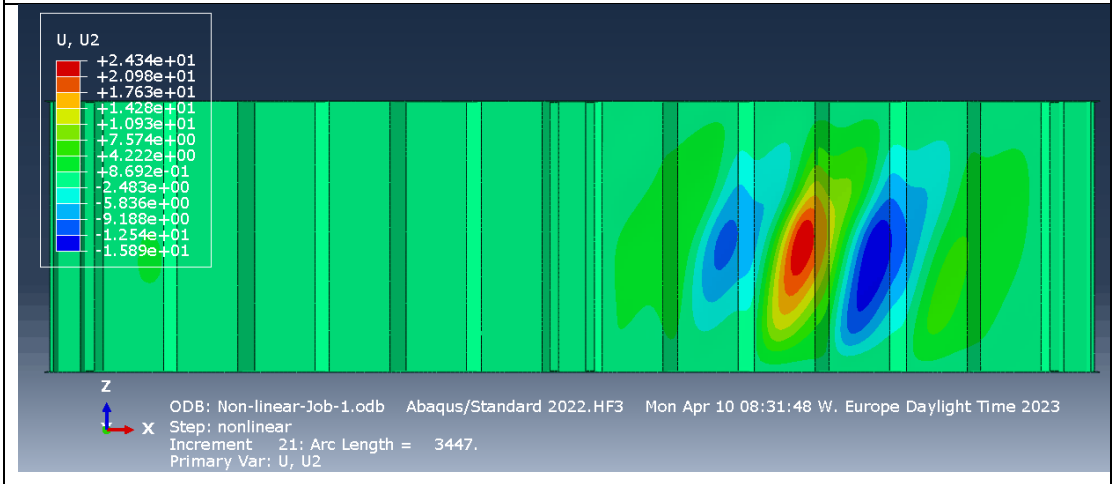

Figure 5.50 *Out of plane deflection for model-7 in failure increment with imperfection equal to* $\frac{h_w}{200}$.

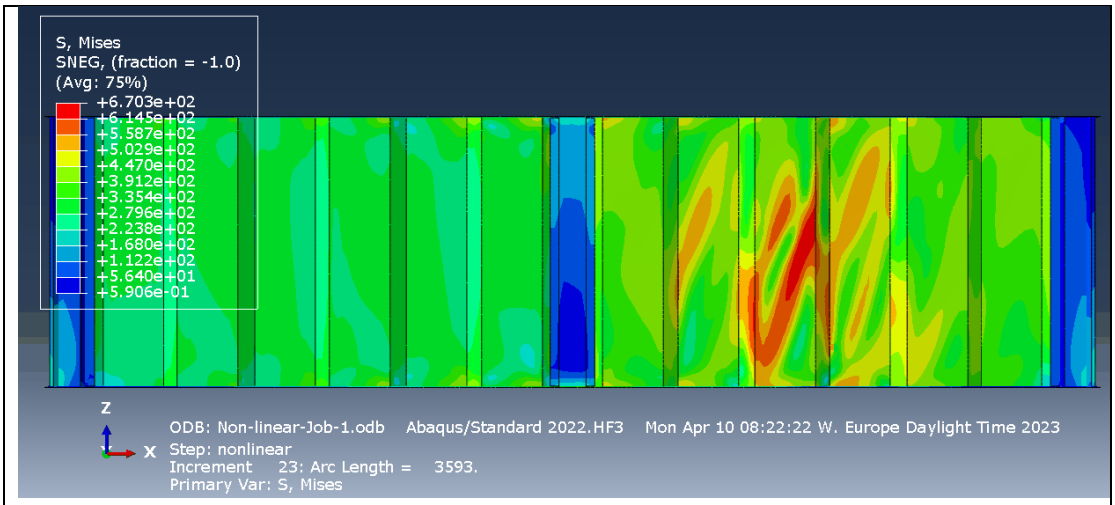

Figure 5.51 Maximum load increment for model-7 with imperfection equal to $\frac{a_{max}}{200}$.

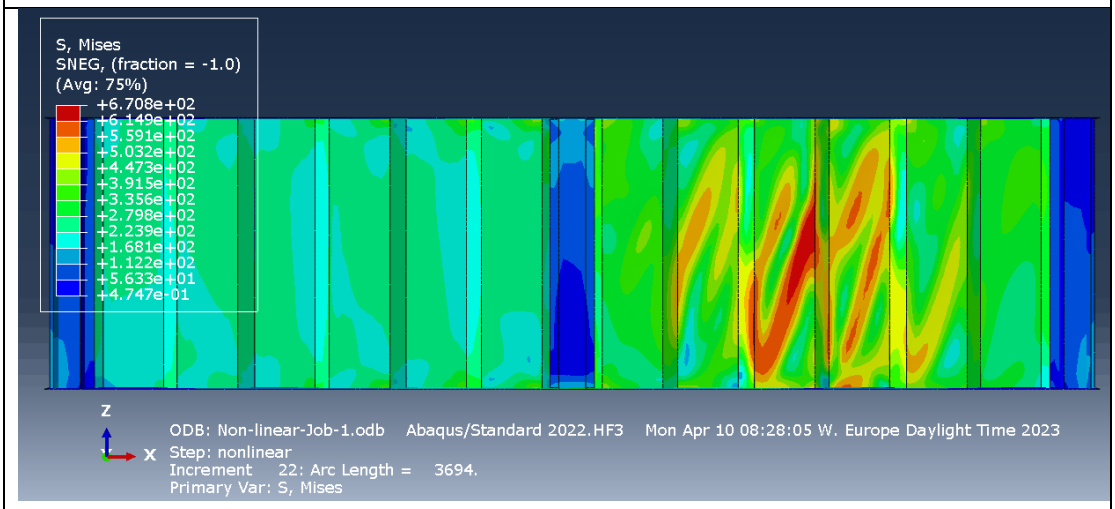

Figure 5.52 Maximum load increment for model-7 with imperfection equal to t_{w1} .

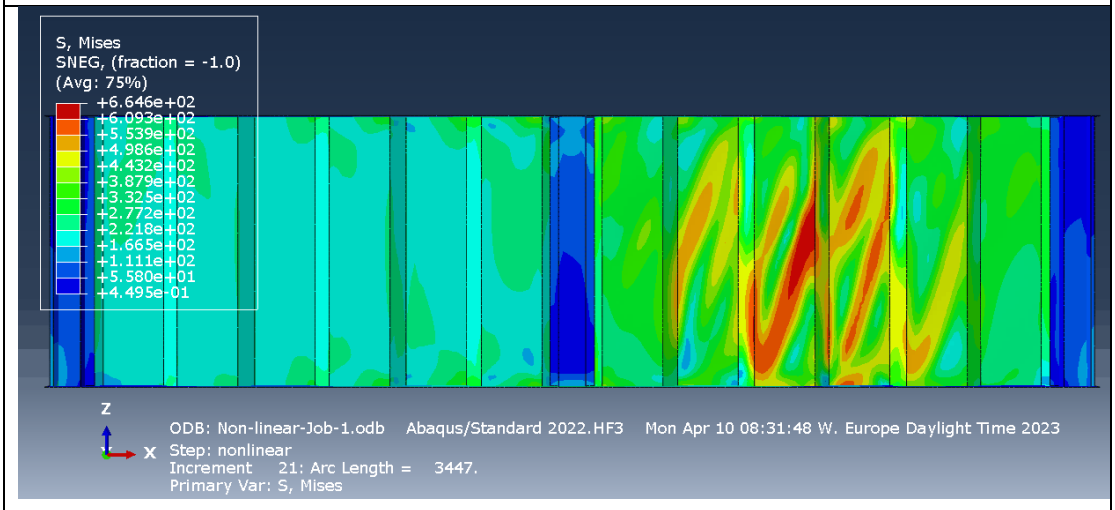

Figure 5.53 Maximum load increment for model-7 with imperfection equal to $\frac{h_w}{200}$.

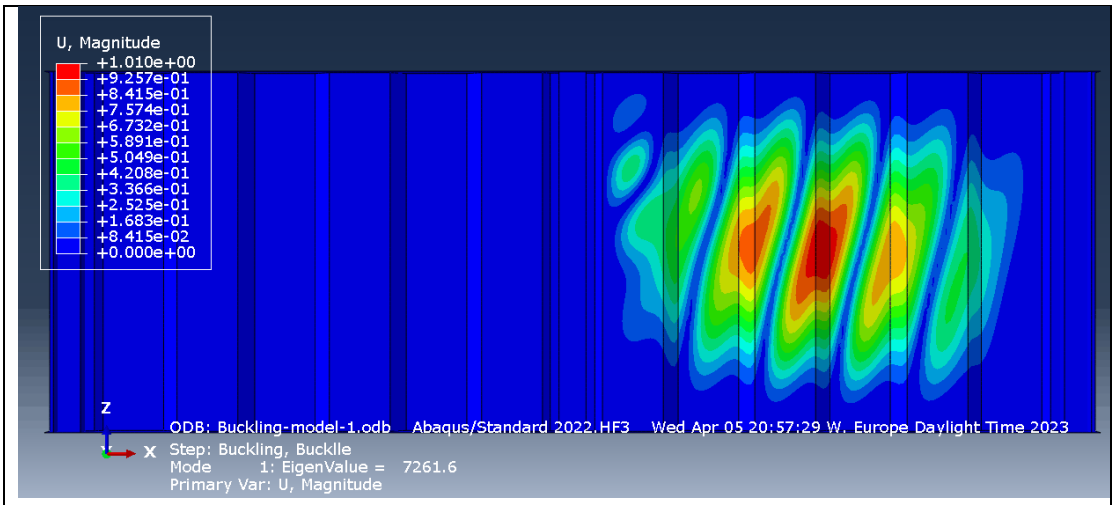

Figure 5.54 Buckling mode 1 for model-8 which is critical for failure with imperfection equal to $\frac{a_{max}}{200}$ *and* $\frac{h_w}{200}$.

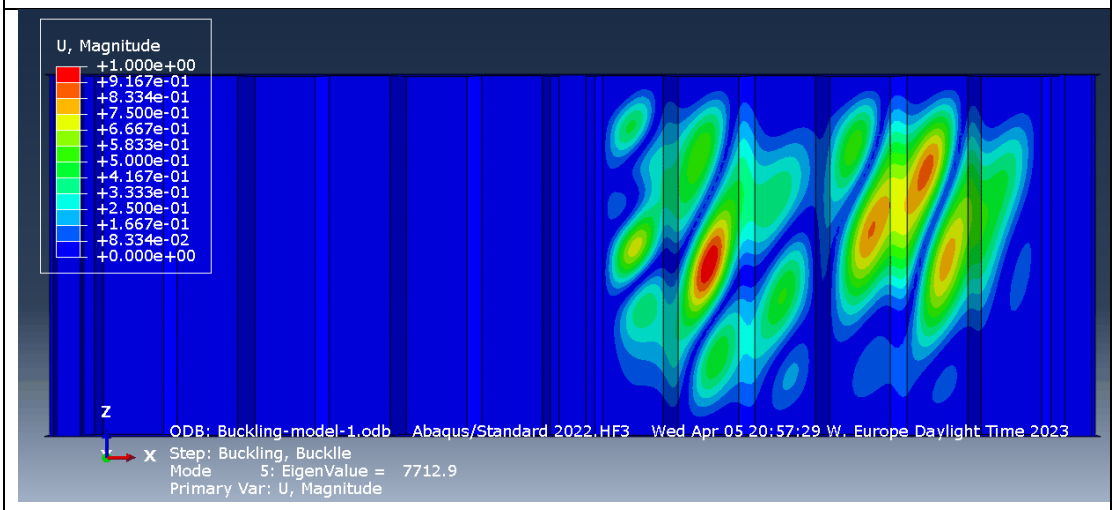

Figure 5.55 Buckling mode 5 for model-8 which is critical for failure with imperfection equal to t_{w1} .

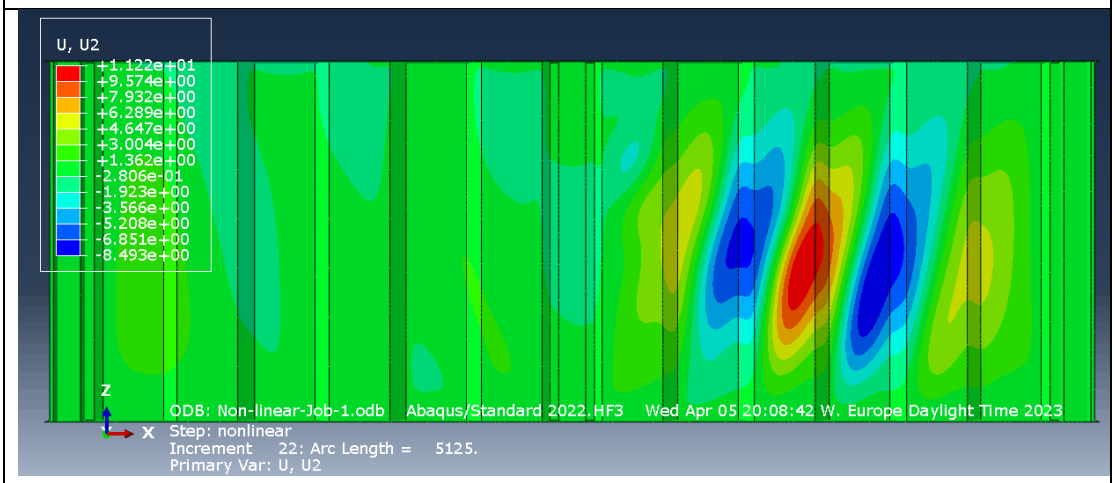

Figure 5.56 Out of plane deflection for model-8 in failure increment with imperfection equal to $\frac{a_{max}}{200}$.

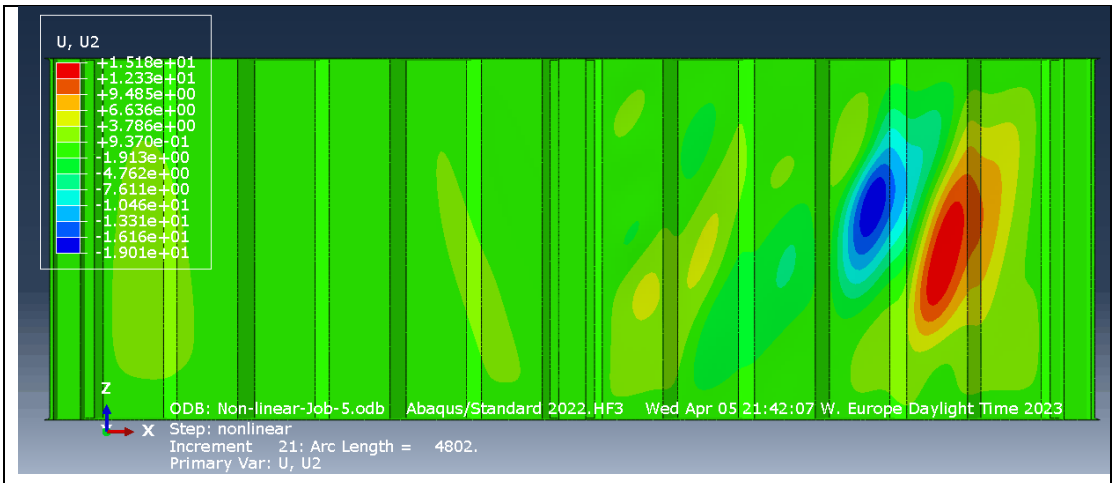

Figure 5.57 *Out of plane deflection for model-8 in failure increment with imperfection equal to* t_{w1}.

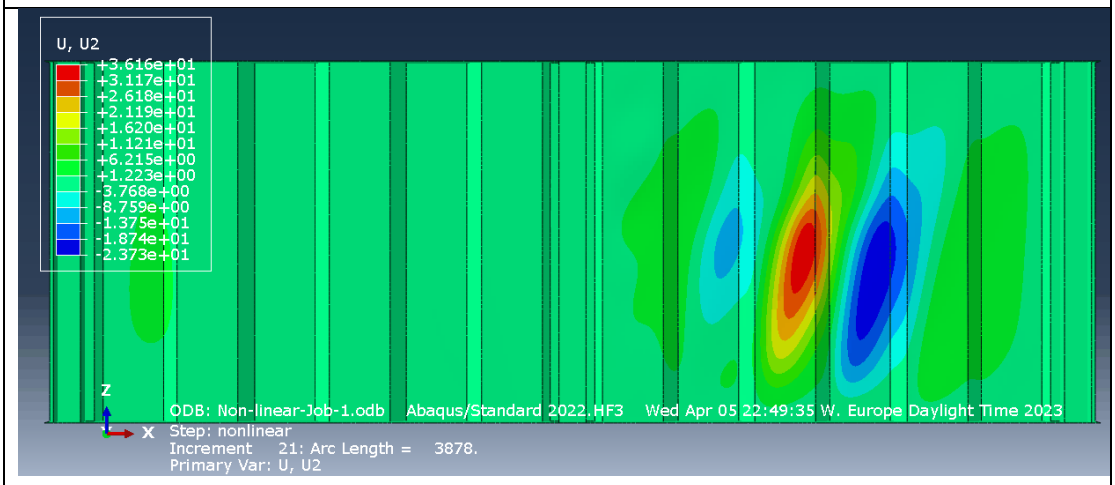

Figure 5.58 *Out of plane deflection for model-8 in failure increment with imperfection equal to* $\frac{h_w}{200}$.

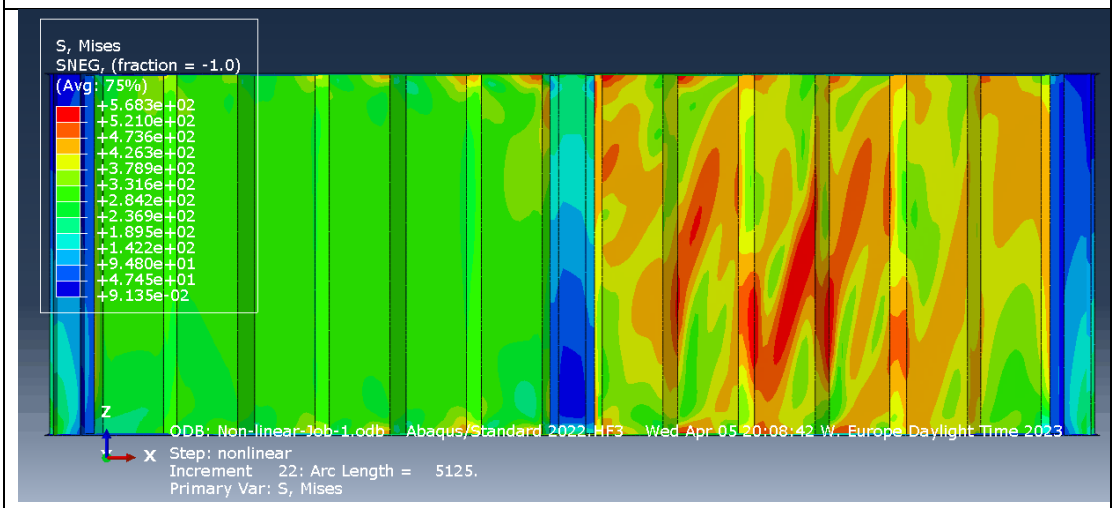

Figure 5.59 *Maximum load increment for model-8 with imperfection equal to* $\frac{a_{max}}{200}$.

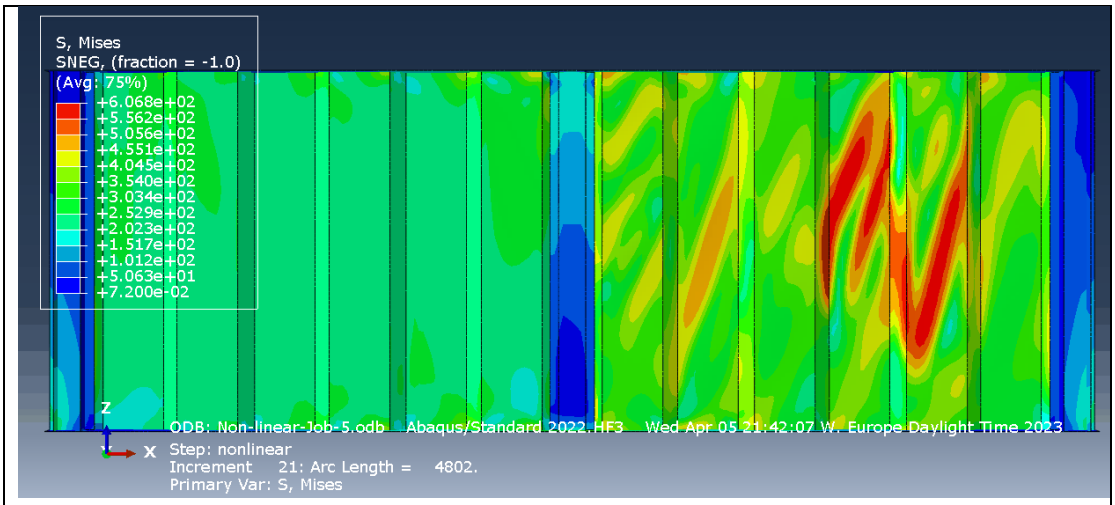

Figure 5.60 Maximum load increment for model-8 with imperfection equal to t_{w1}.

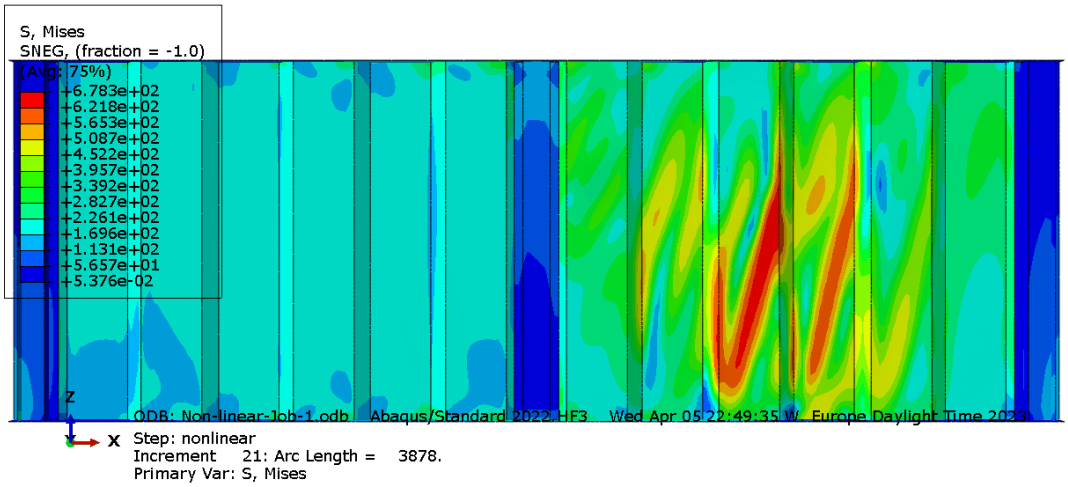

Figure 5.61 Maximum load increment for model-8 with imperfection equal to $\frac{h_w}{200}$.

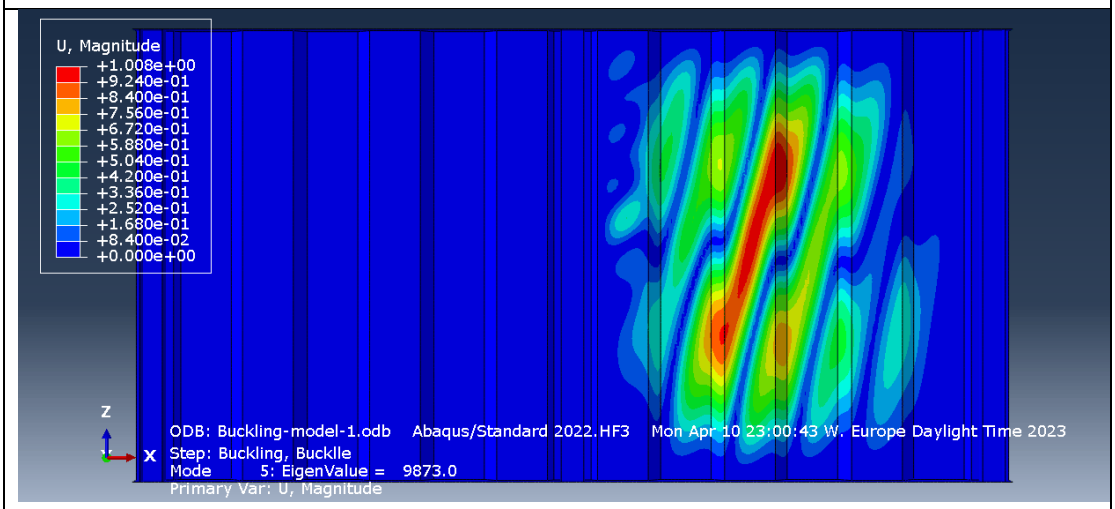

Figure 5.62 Buckling mode 5 for model-9 which is critical for failure with imperfection equal to $\frac{a_{max}}{200}$, t_{w1} *and* $\frac{h_w}{200}$.

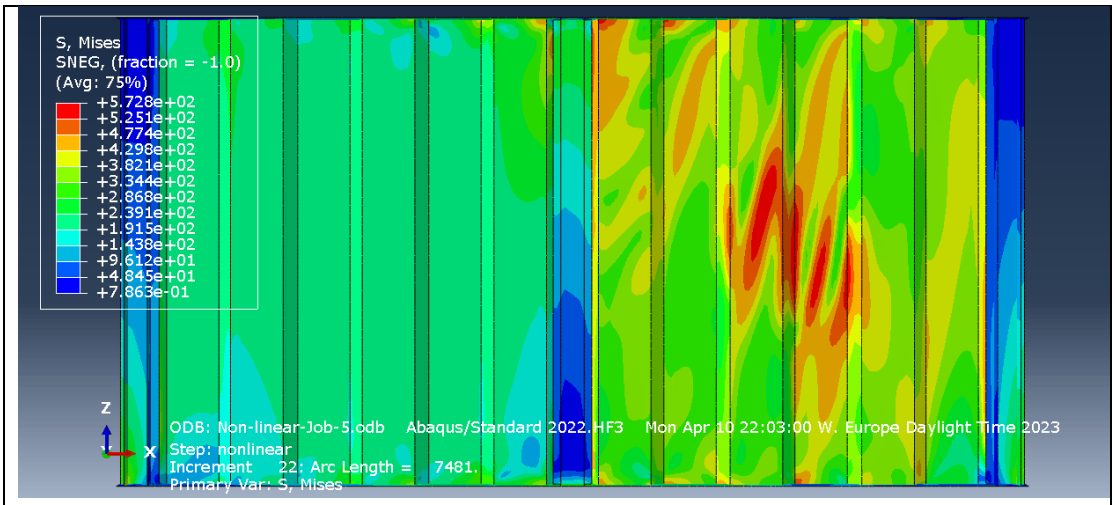

Figure 5.63 Maximum load increment for model-9 with imperfection equal to $\frac{a_{max}}{200}$.

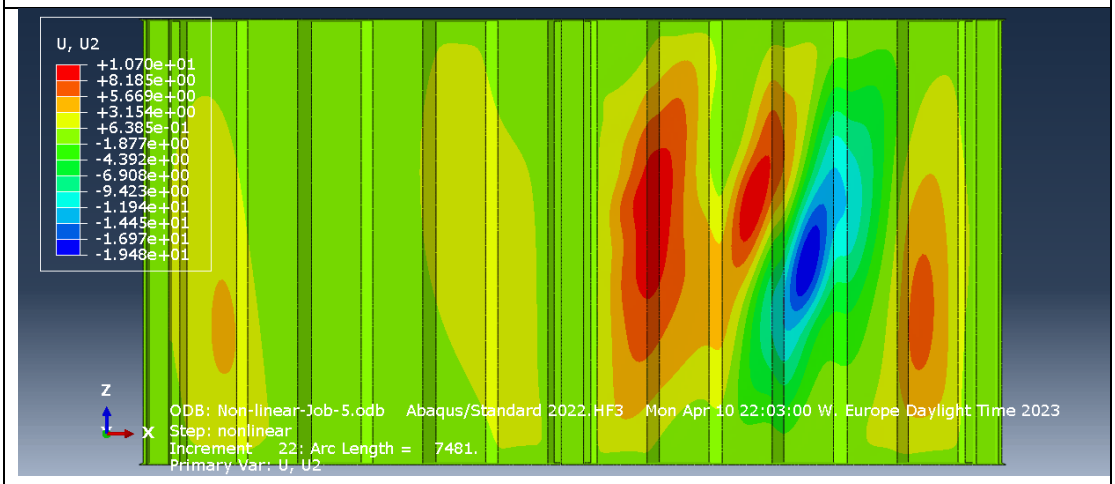

Figure 5.64 Out of plane deflection for model-9 in failure increment with imperfection equal to $\frac{a_{max}}{200}$.

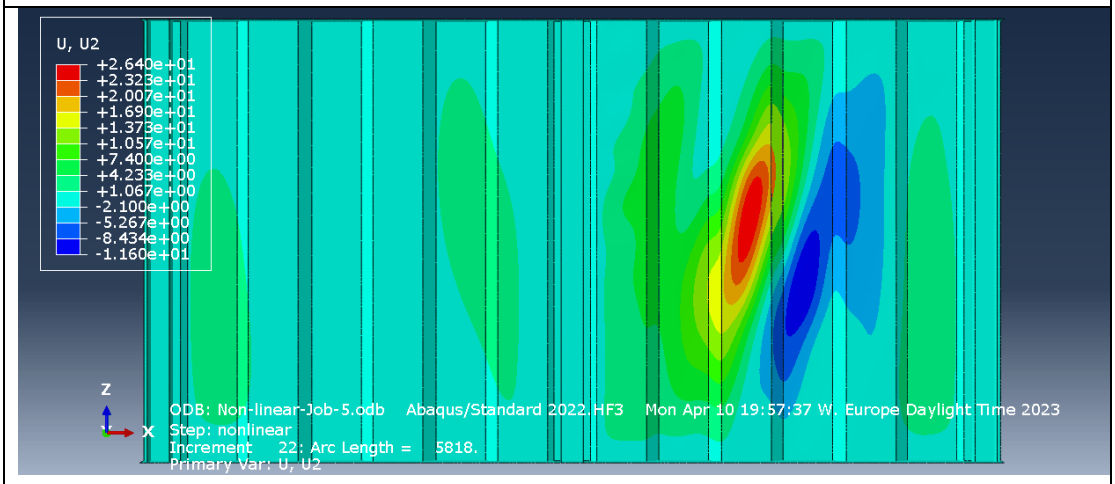

Figure 5.65 Out of plane deflection for model-9 in failure increment with imperfection equal to t_{w1}.

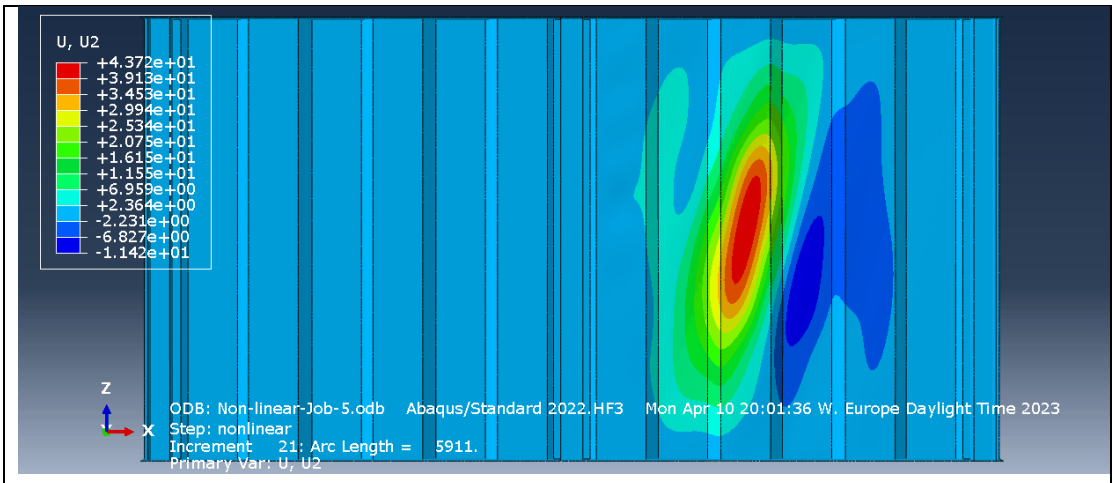

Figure 5.66 Out of plane deflection for model-9 in failure increment with imperfection equal to $\frac{h_w}{200}$.

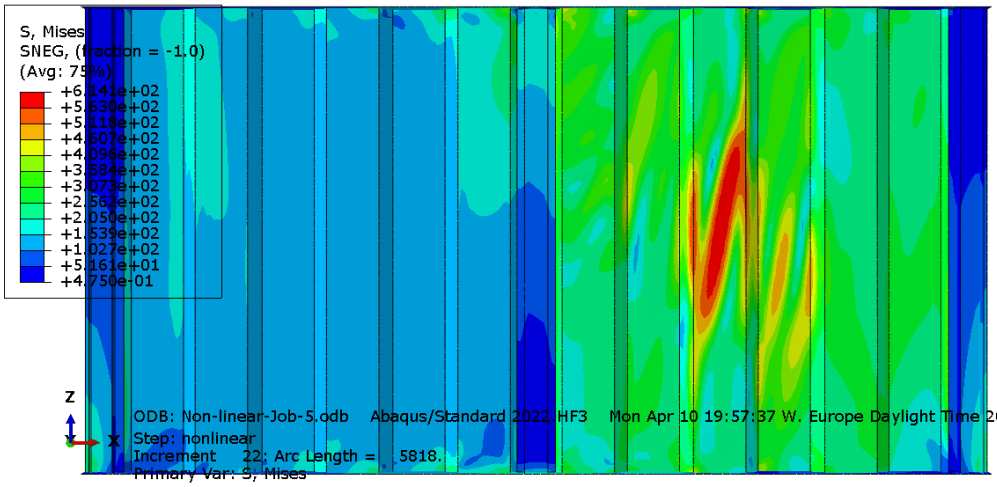

Figure 5.67 Maximum load increment for model-9 with imperfection equal to t_{w1}.

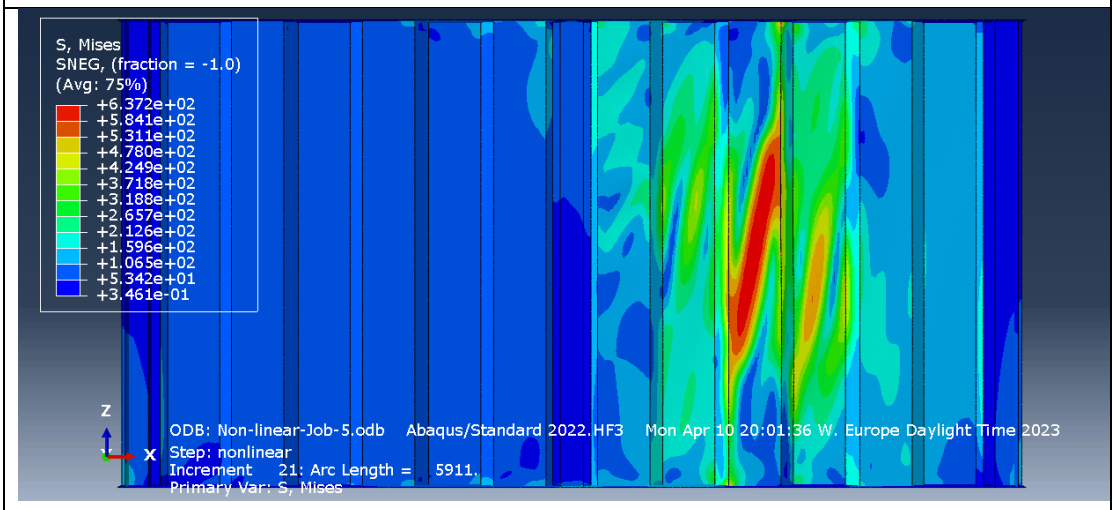

Figure 5.68 Maximum load increment for model-9 with imperfection equal to $\frac{h_w}{200}$.

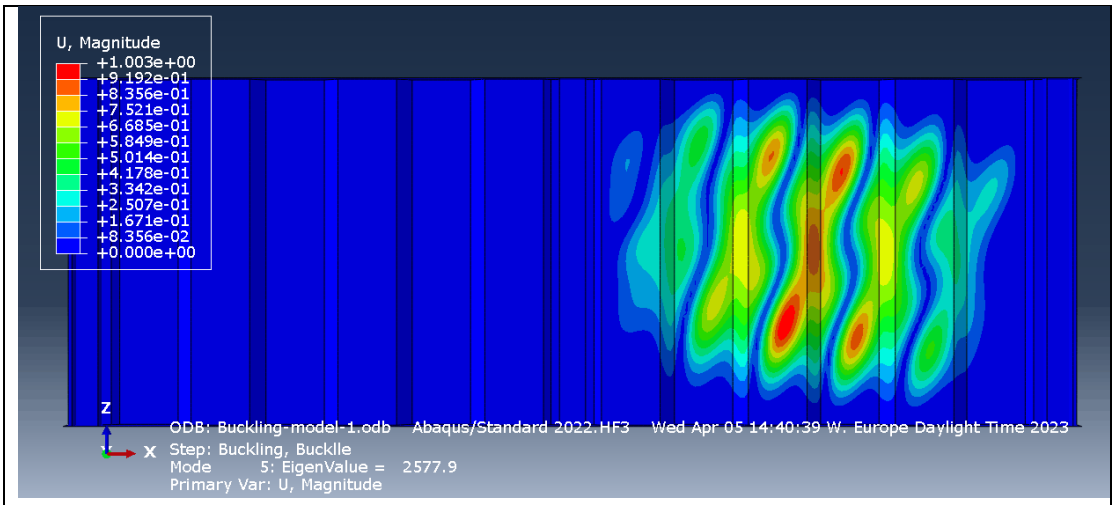

Figure 5.69 *Buckling mode 5 for model-10 which is critical for failure with imperfection equal to* $\frac{a_{max}}{200}$, t_{w1} *and* $\frac{h_w}{200}$.

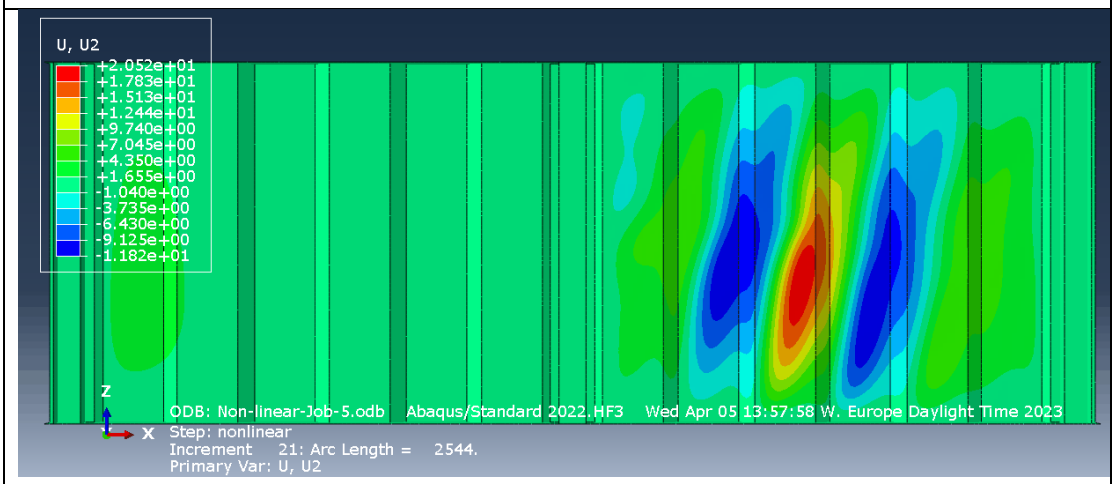

Figure 5.70 *Out of plane deflection for model-10 in failure increment with imperfection equal to* $\frac{a_{max}}{200}$.

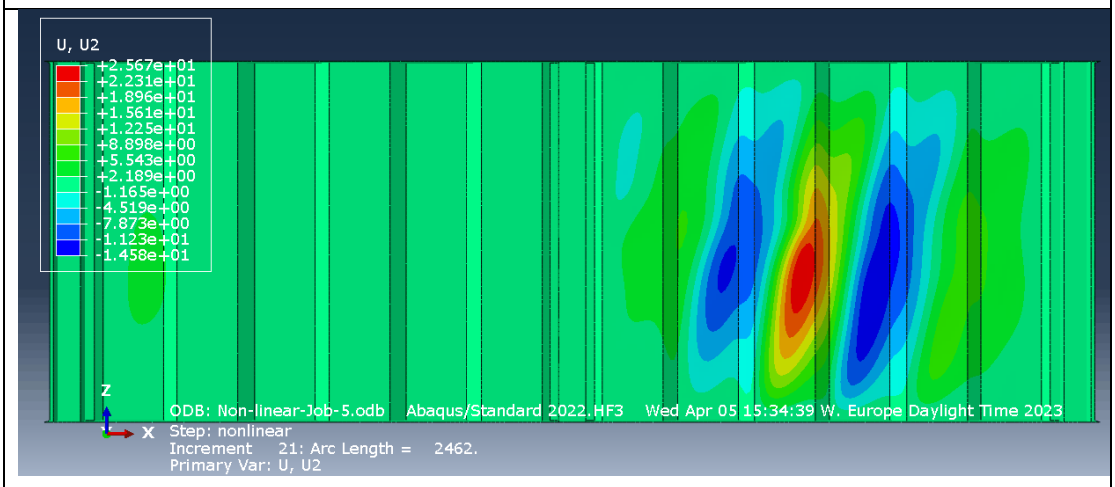

Figure 5.71 *Out of plane deflection for model-10 in failure increment with imperfection equal to* t_{w1}.

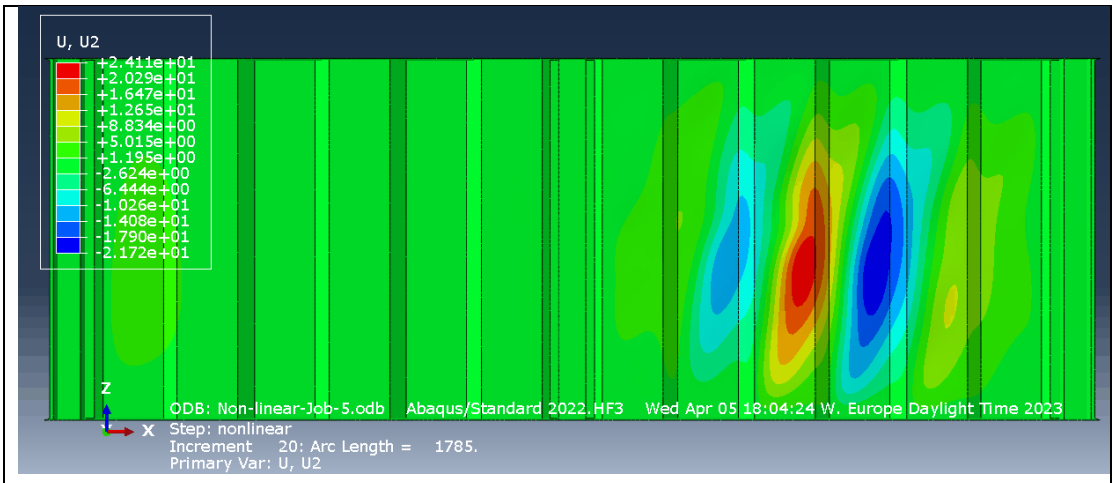

Figure 5.72 *Out of plane deflection for model-10 in failure increment with imperfection equal to* $\frac{h_w}{200}$.

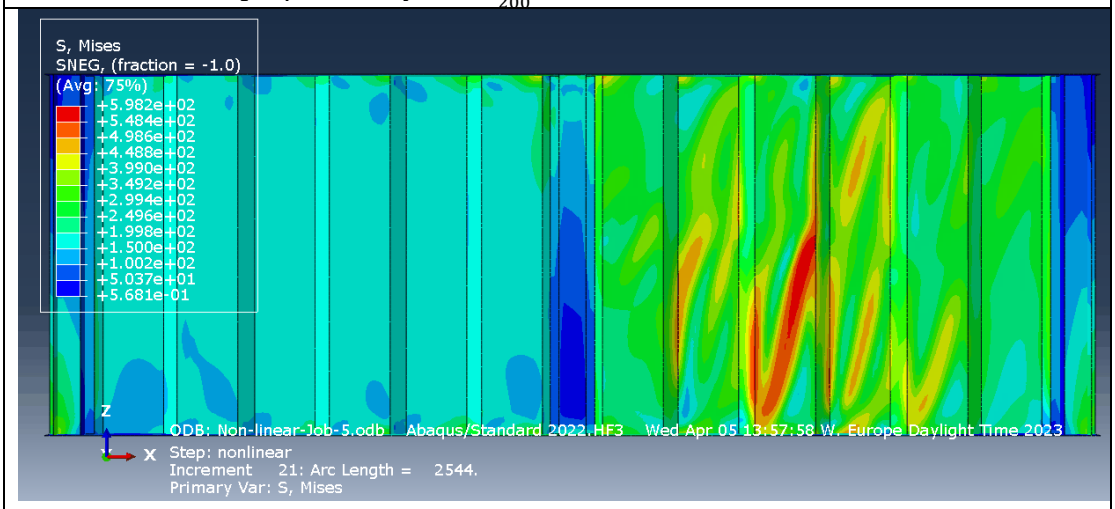

Figure 5.73 *Maximum load increment for model-10 with imperfection equal to* $\frac{a_{max}}{200}$.

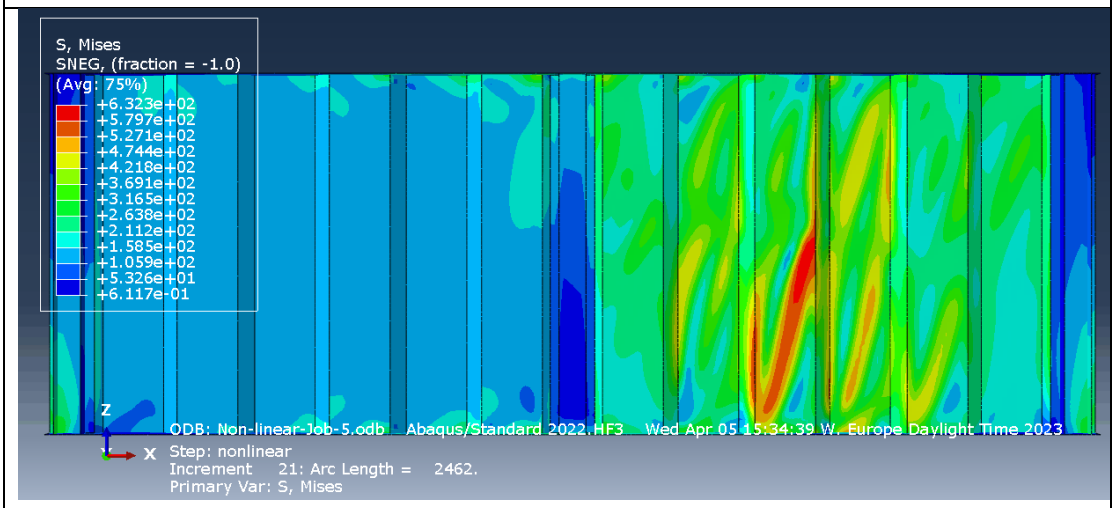

Figure 5.74 *Maximum load increment for model-10 with imperfection equal to* t_{w1}.

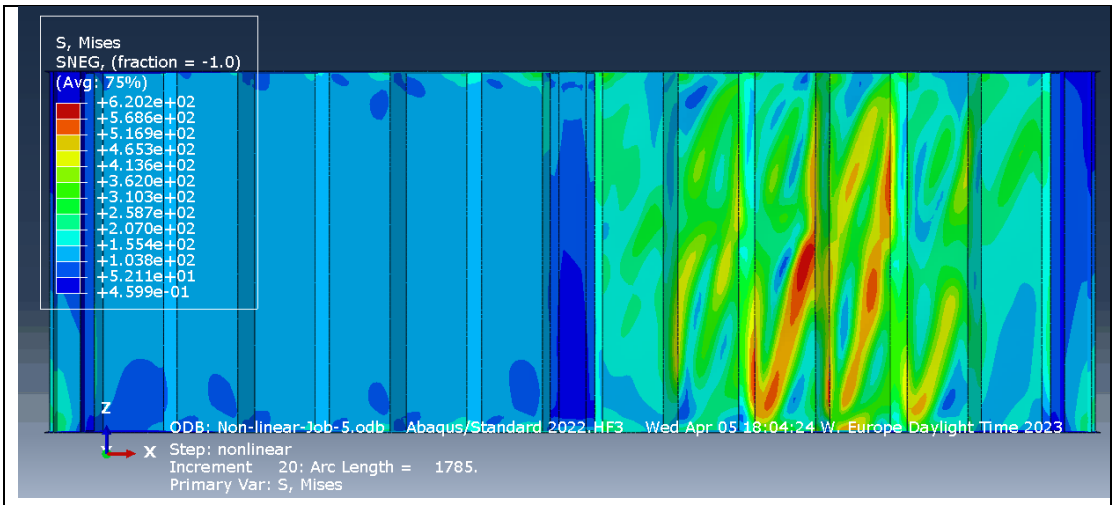

Figure 5.75 Maximum load increment for model-10 with imperfection equal to $\frac{h_w}{200}$.

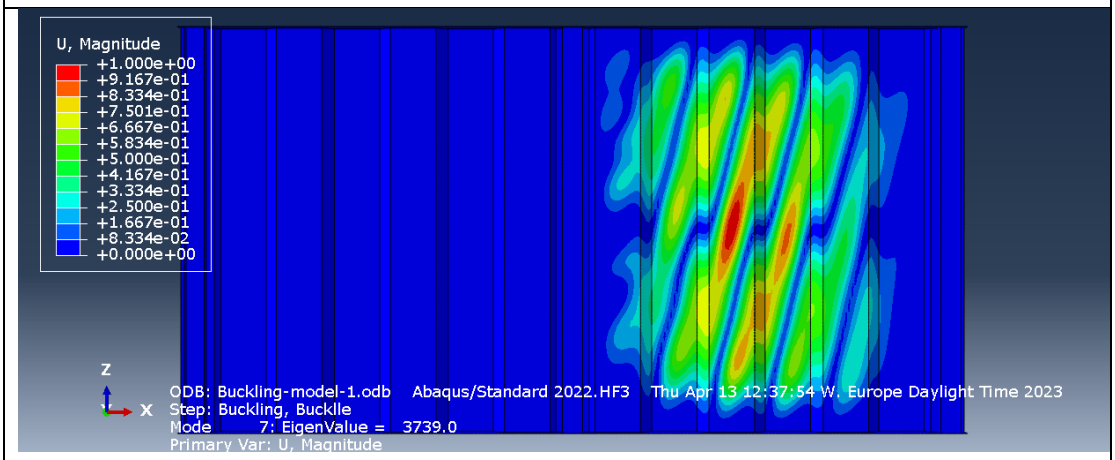

Figure 5.76 Buckling mode 7 for model-11 which is critical for failure with imperfection equal to $\frac{a_{max}}{200}$, t_{w1} *and* $\frac{h_w}{200}$.

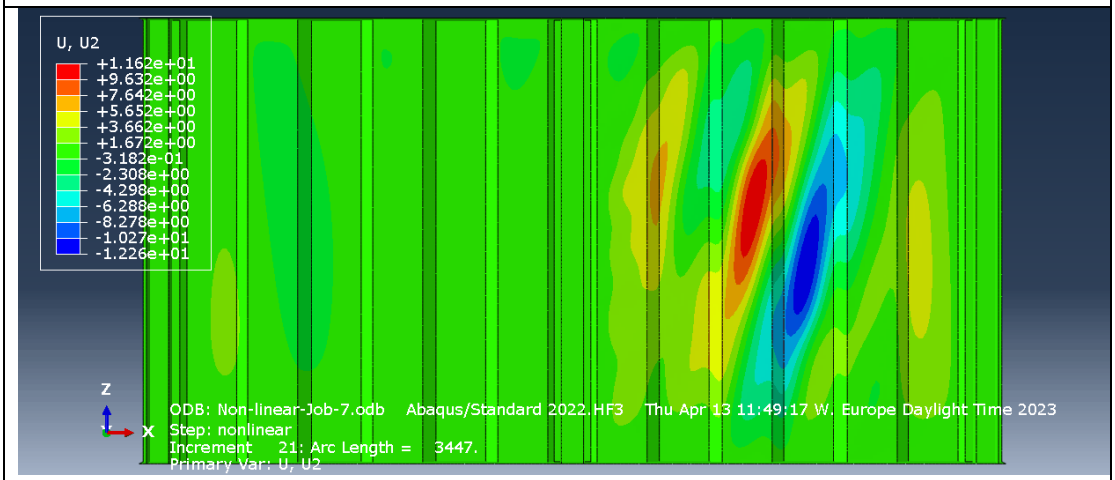

Figure 5.77 Out of plane deflection for model-11 in failure increment with imperfection equal to $\frac{a_{max}}{200}$.

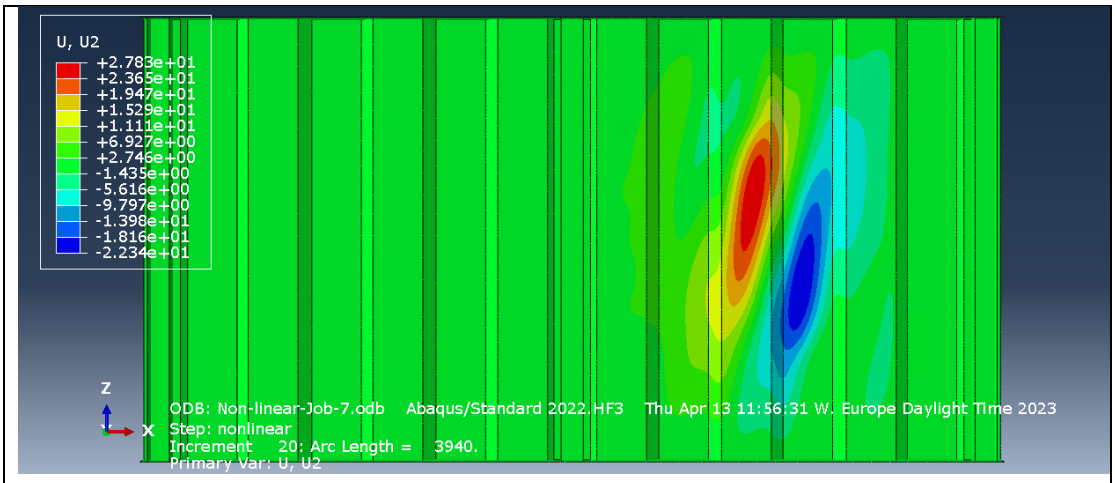

Figure 5.78 *Out of plane deflection for model-11 in failure increment with imperfection equal to* t_{w1}.

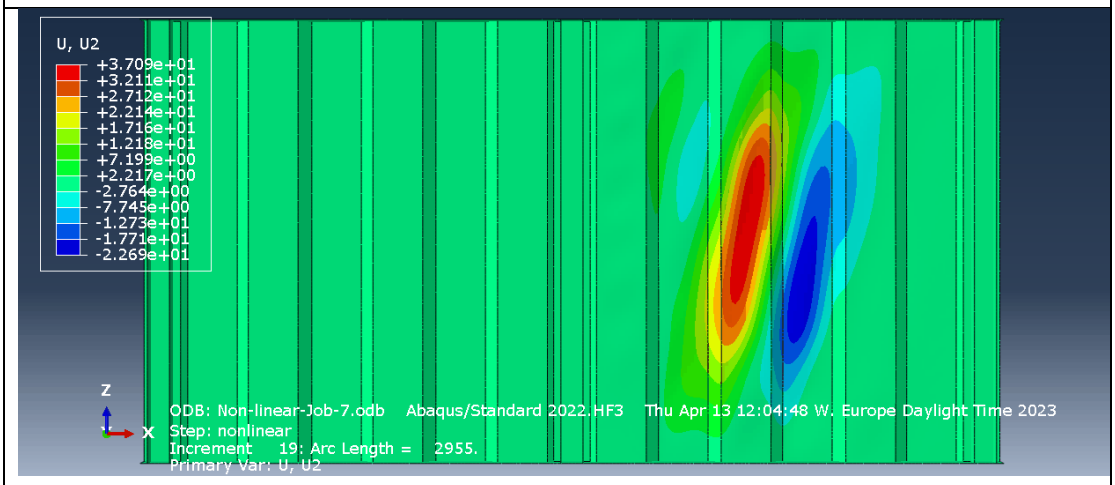

Figure 5.79 *Out of plane deflection for model-11 in failure increment with imperfection equal to* $\frac{h_w}{200}$.

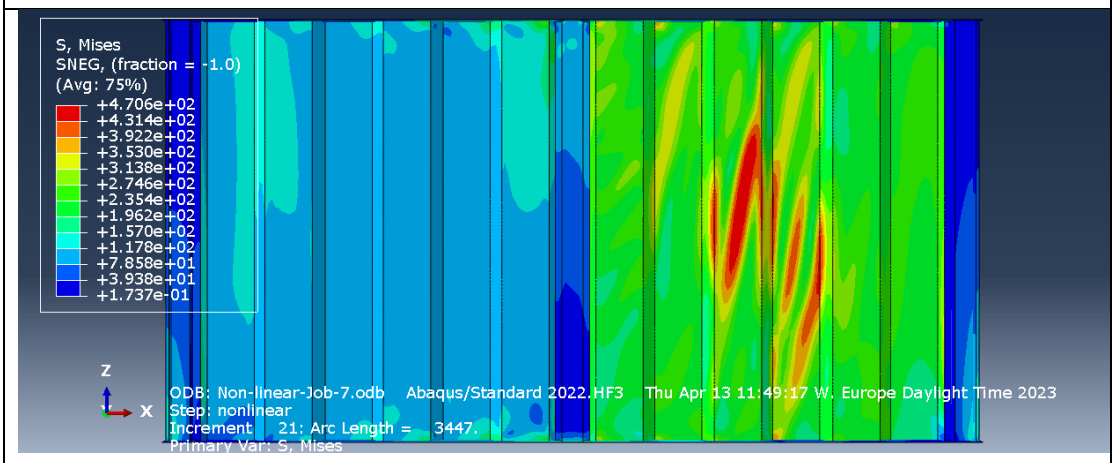

Figure 5.80 *Maximum load increment for model-11 with imperfection equal to* $\frac{a_{max}}{200}$.

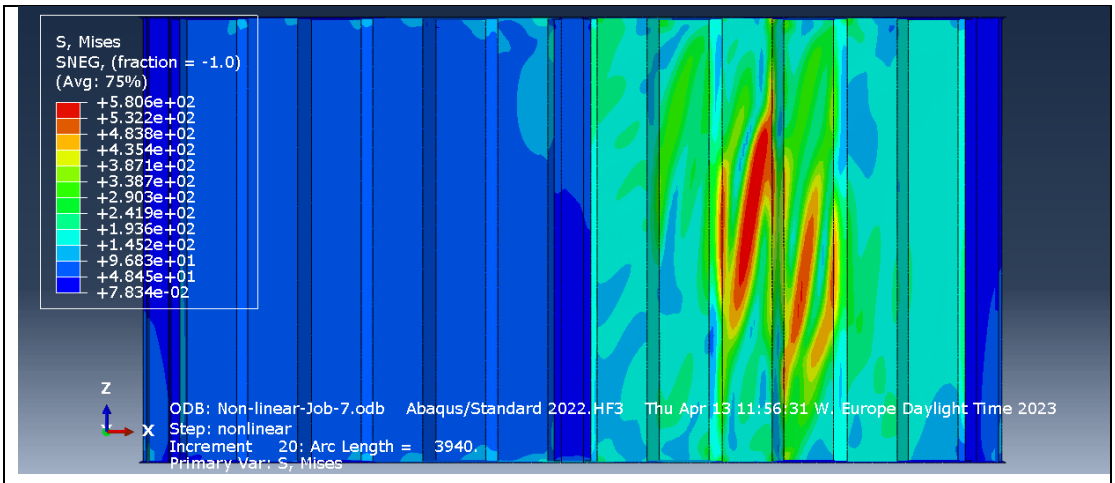

Figure 5.81 Maximum load increment for model-11 with imperfection equal to t_{w1}.

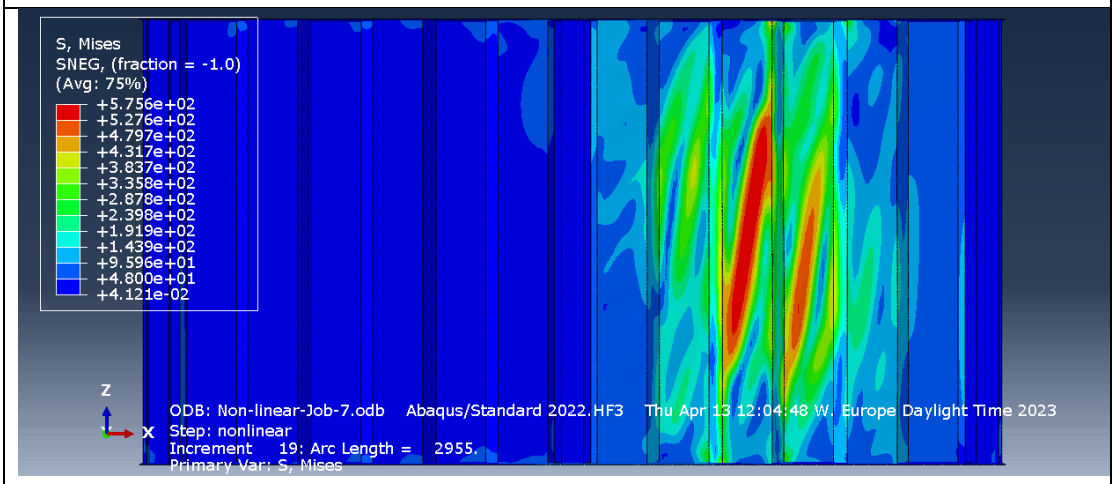

Figure 5.82 Maximum load increment for model-11 with imperfection equal to $\frac{h_w}{200}$.

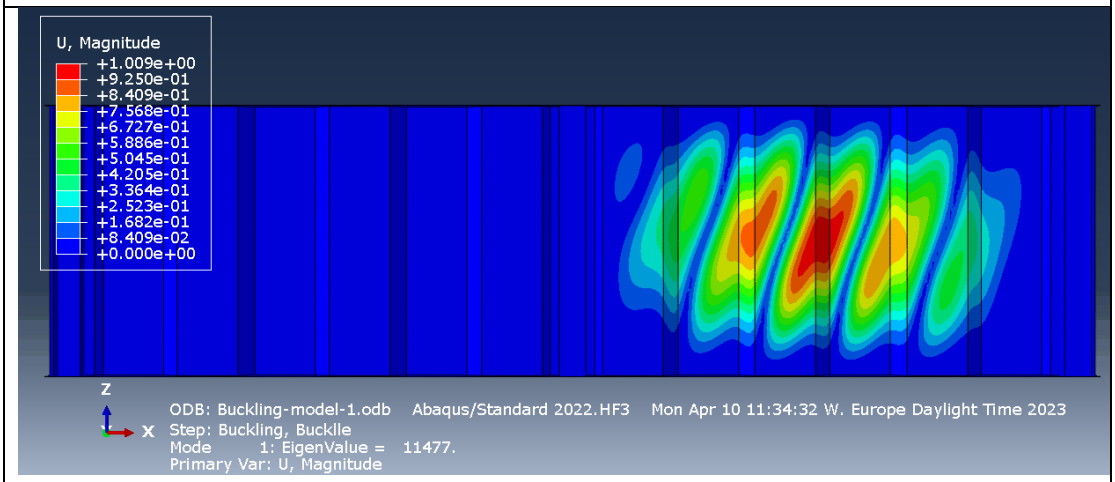

Figure 5.83 Buckling mode 1 for model-12 which is critical for failure with imperfection equal to $\frac{a_{max}}{200}$.

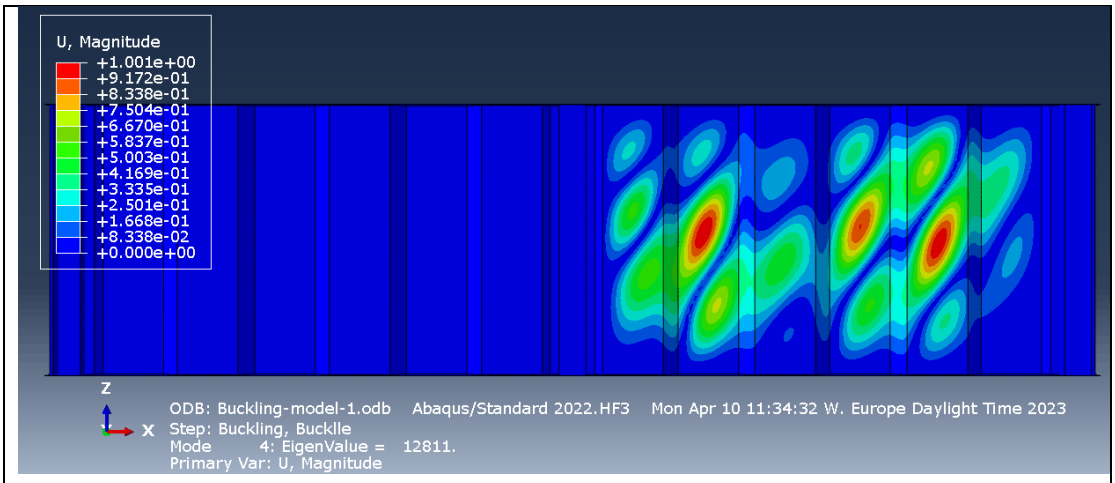

Figure 5.84 Buckling mode 4 for model-12 which is critical for failure with imperfection equal to t_{w1}.

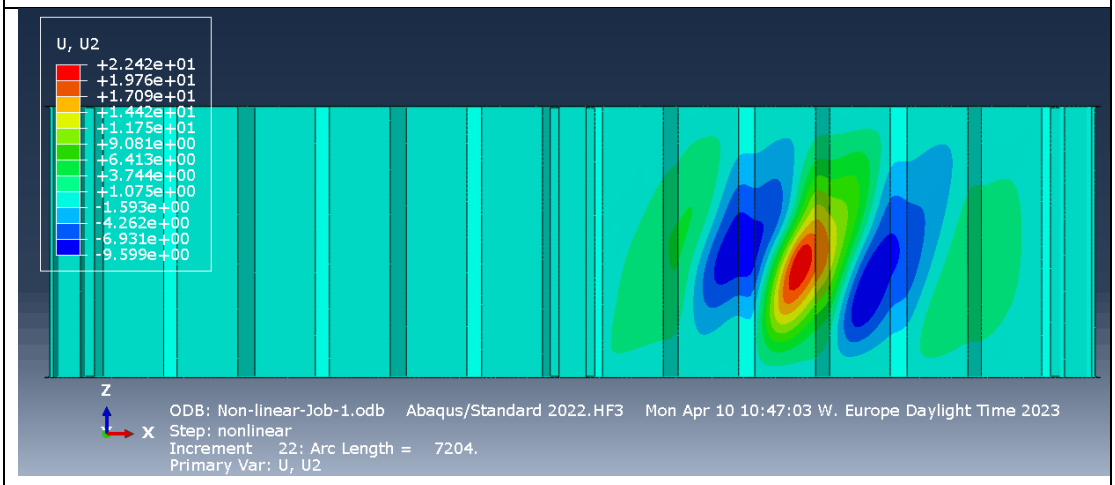

Figure 5.85 Out of plane deflection for model-12 in failure increment with imperfection equal to $\frac{a_{max}}{200}$.

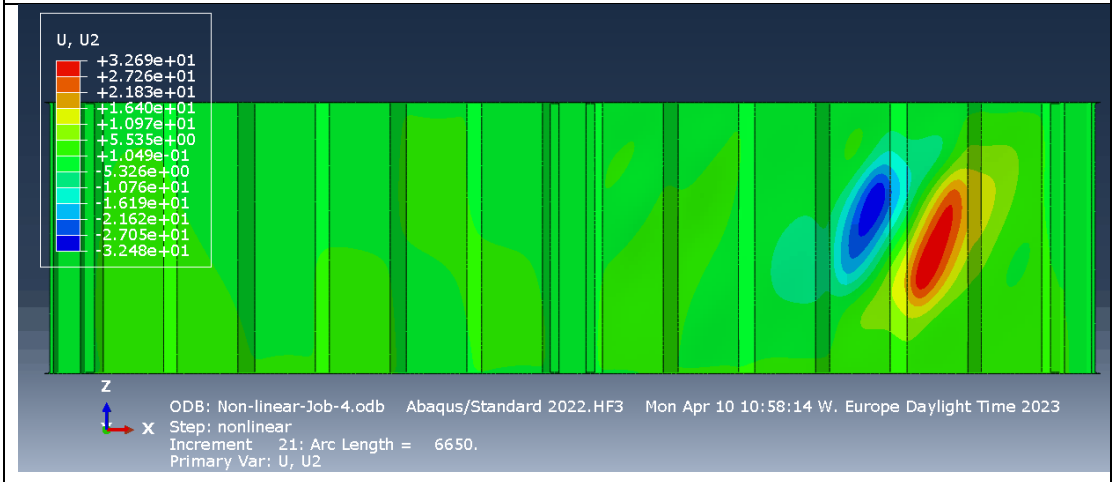

Figure 5.86 Out of plane deflection for model-12 in failure increment with imperfection equal to t_{w1}.

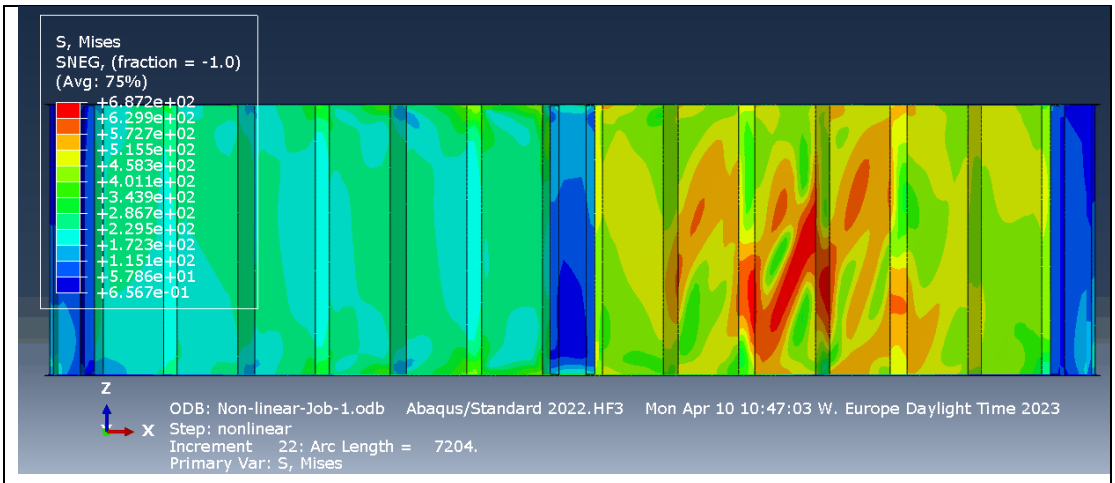

Figure 5.87 Maximum load increment for model-12 with imperfection equal to $\frac{a_{max}}{200}$.

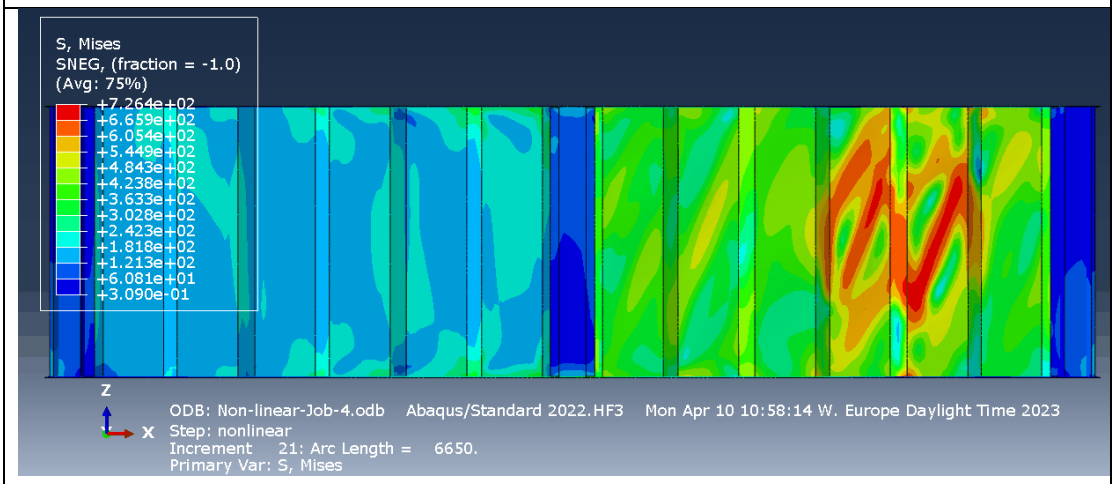

Figure 5.88 Maximum load increment for model-12 with imperfection equal to t_{w1}.

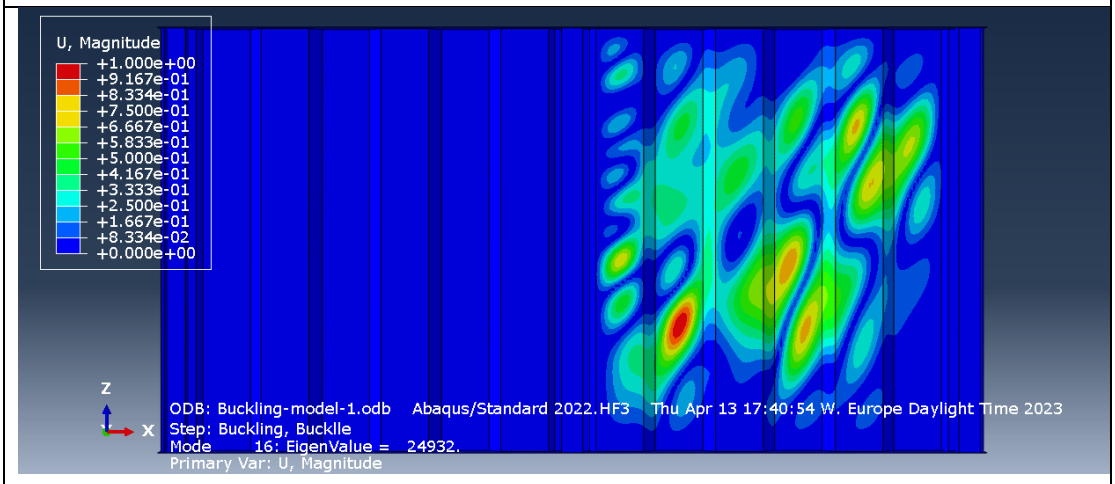

Figure 5.89 Buckling mode 16 for model-13 which is critical for failure with imperfection equal to $\frac{a_{max}}{200}$.

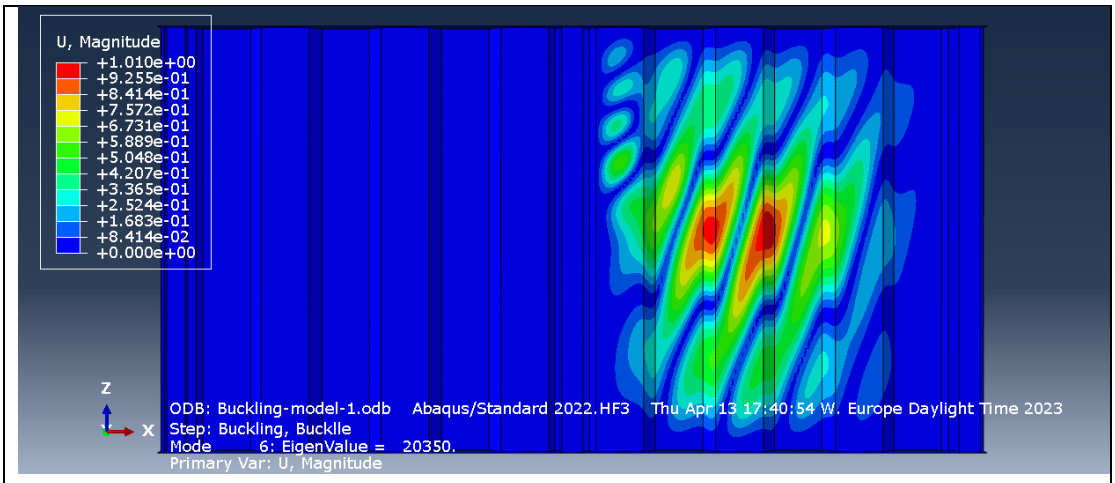

Figure 5.90 *Buckling mode 6 for model-13 which is critical for failure with imperfection equal to* t_{w1} *and* $\frac{h_w}{200}$.

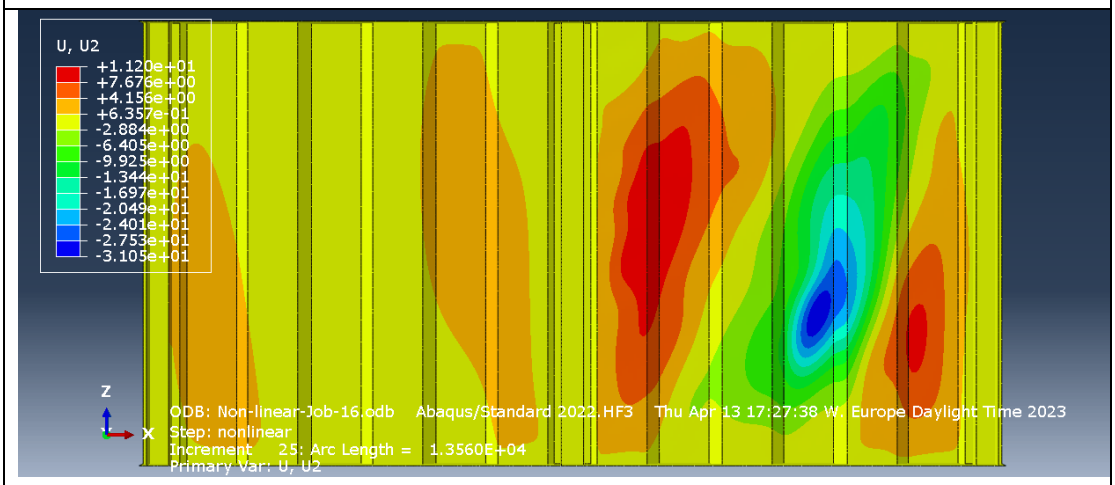

Figure 5.91 *Out of plane deflection for model-13 in failure increment with imperfection equal to* $\frac{a_{max}}{200}$.

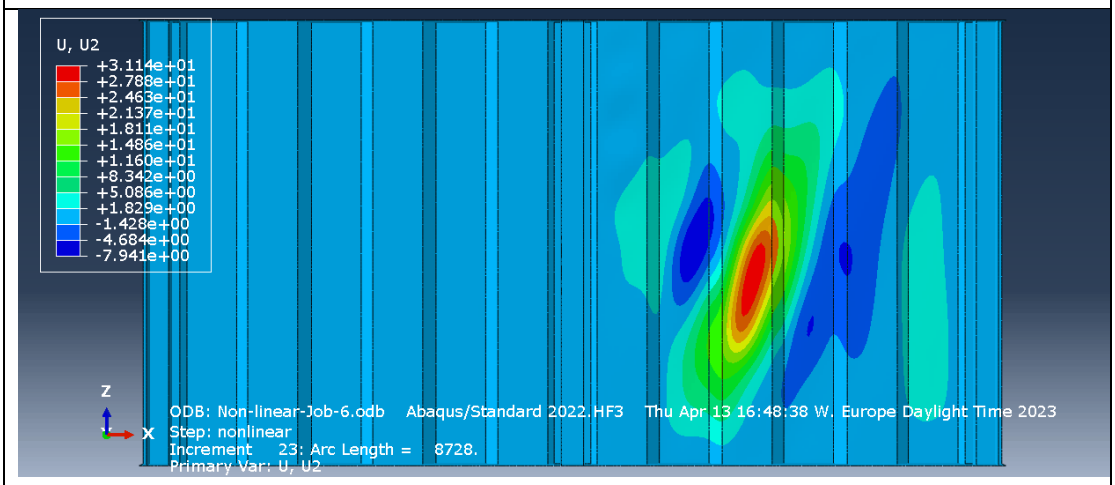

Figure 5.92 *Out of plane deflection for model-13 in failure increment with imperfection equal to* t_{w1}.

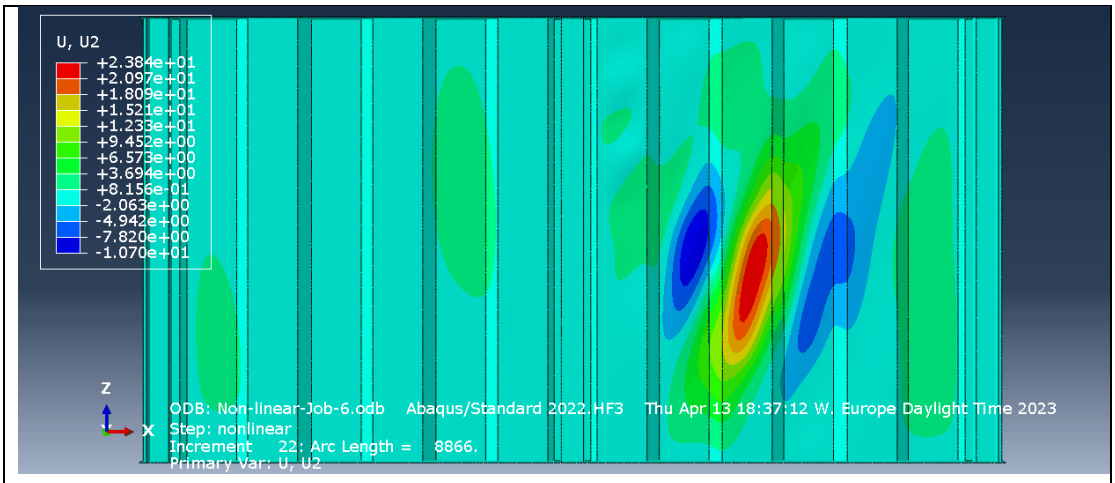

Figure 5.93 *Out of plane deflection for model-13 in failure increment with imperfection equal to* $\frac{h_w}{200}$.

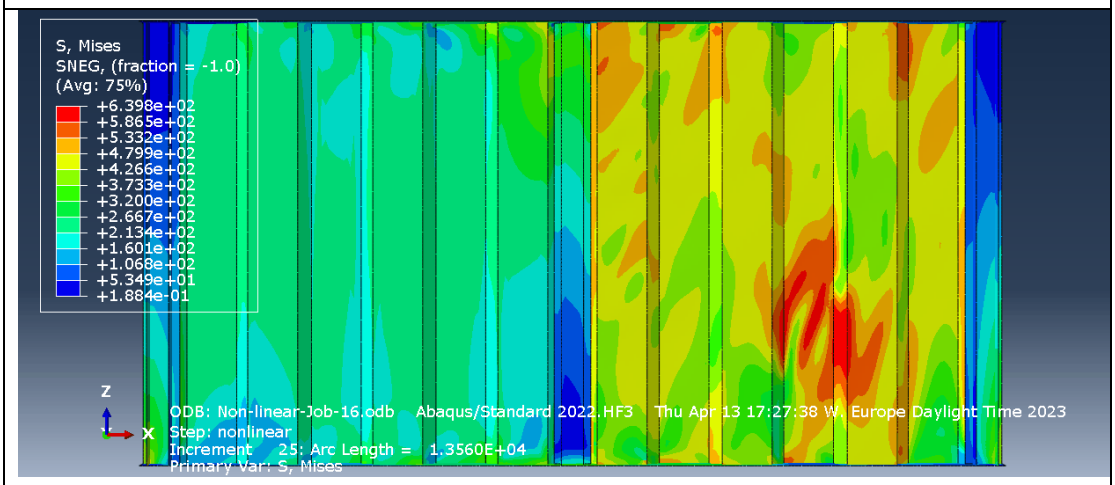

Figure 5.94 *Maximum load increment for model-13 with imperfection equal to* $\frac{a_{max}}{200}$.

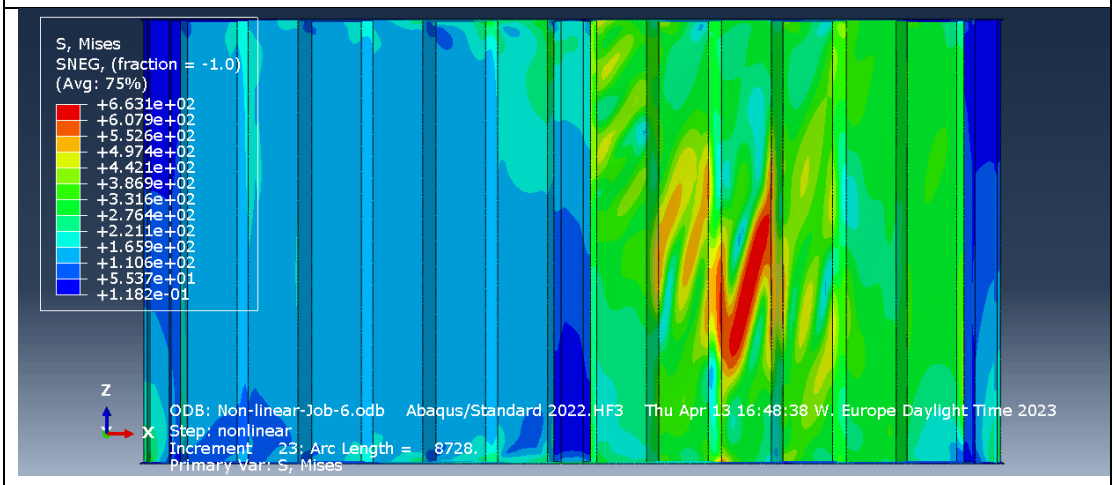

Figure 5.95 *Maximum load increment for model-13 with imperfection equal to* t_{w1}.

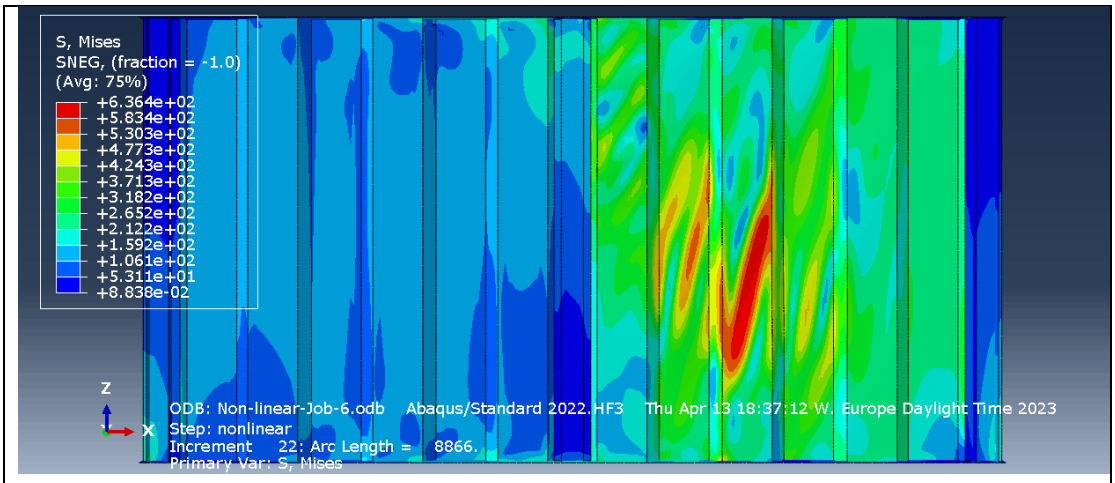

Figure 5.96 Maximum load increment for model-13 with imperfection equal to $\frac{h_w}{200}$.

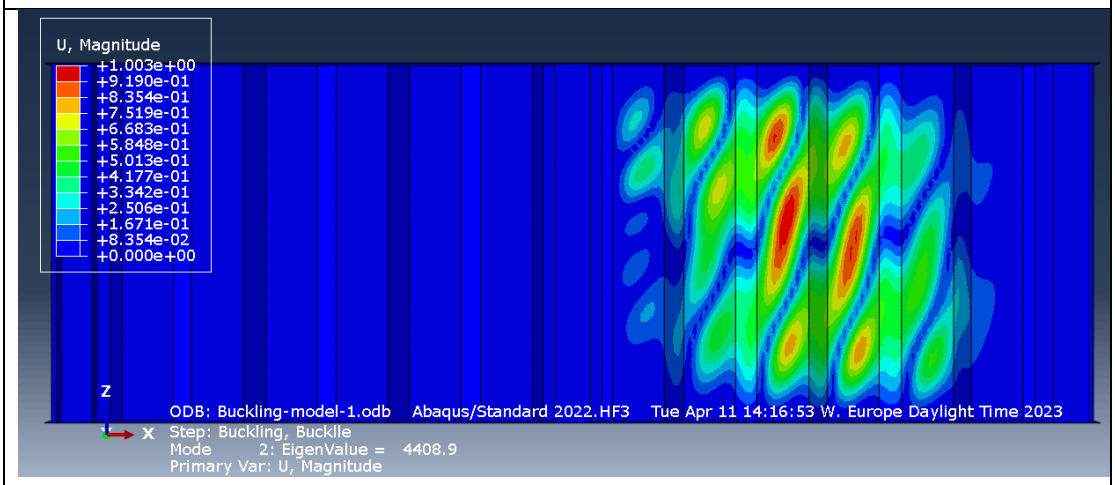

Figure 5.97 Buckling mode 2 for model-14 which is critical for failure with imperfection equal to $\frac{a_{max}}{200}$, t_{w1} *and* $\frac{h_w}{200}$.

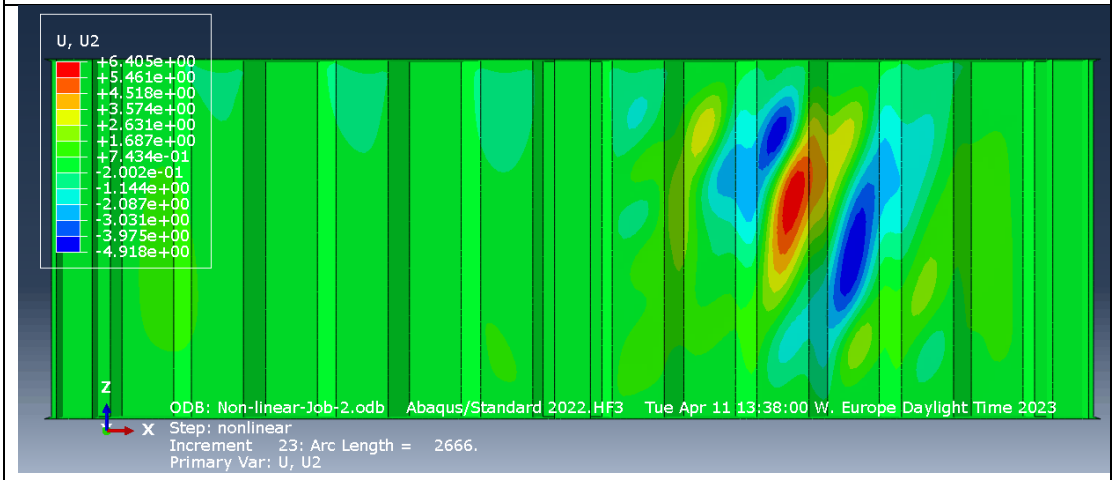

Figure 5.98 Out of plane deflection for model-14 in failure increment with imperfection equal to $\frac{a_{max}}{200}$.

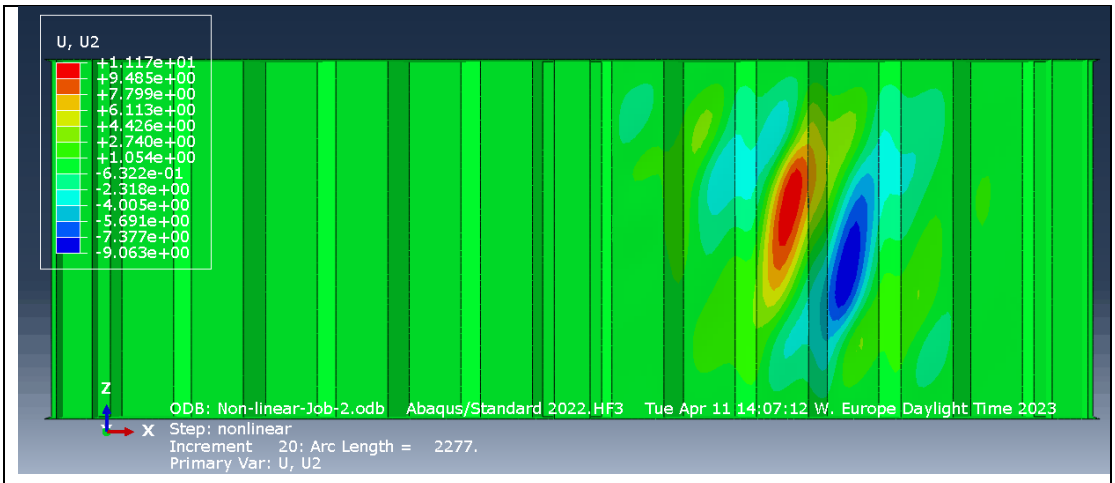

Figure 5.99 *Out of plane deflection for model-14 in failure increment with imperfection equal to* t_{w1}.

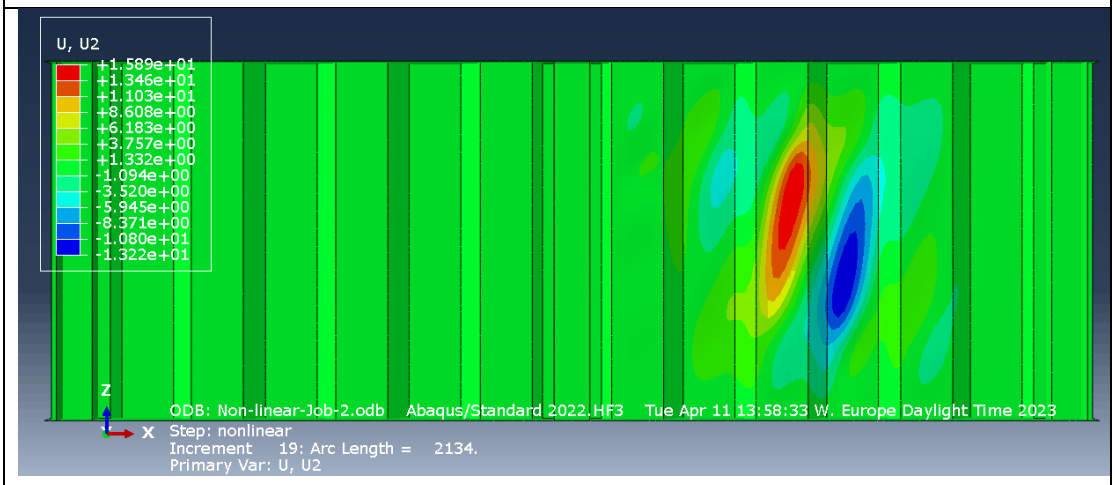

Figure 5.100 *Out of plane deflection for model-14 in failure increment with imperfection equal to* $\frac{h_w}{200}$.

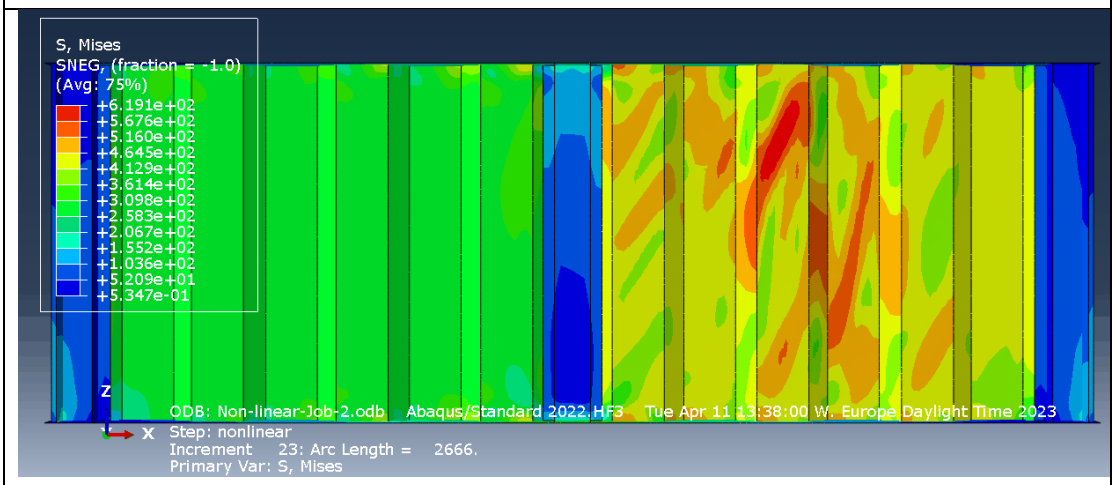

Figure 5.101 *Maximum load increment for model-14 with imperfection equal to* $\frac{a_{max}}{200}$.

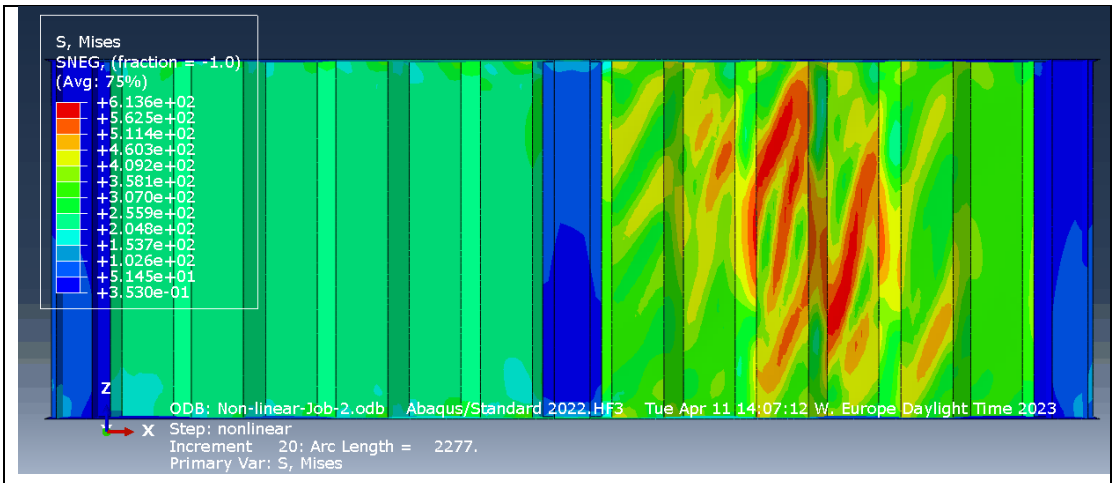

Figure 5.102 Maximum load increment for model-14 with imperfection equal to t_{w1}.

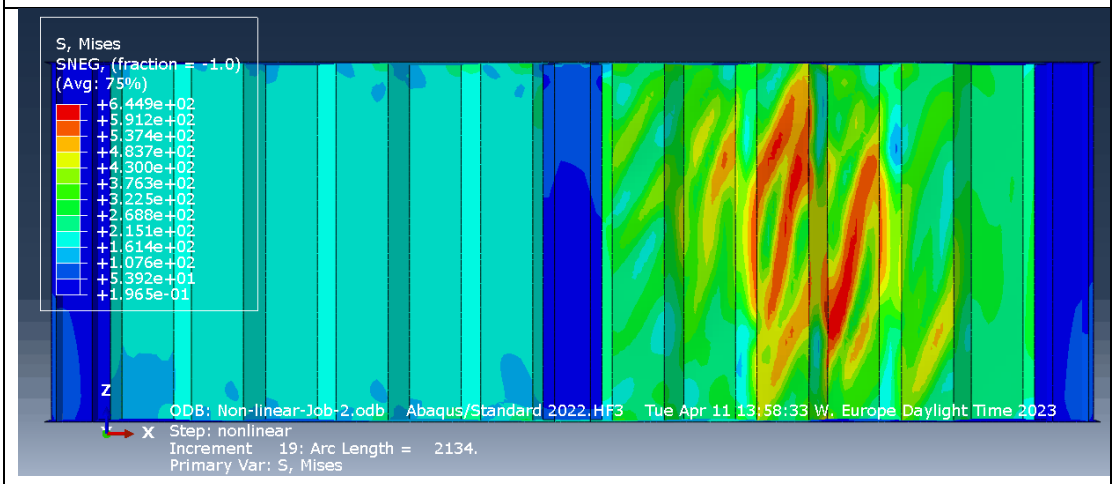

Figure 5.103 Maximum load increment for model-14 with imperfection equal to $\frac{h_w}{200}$.

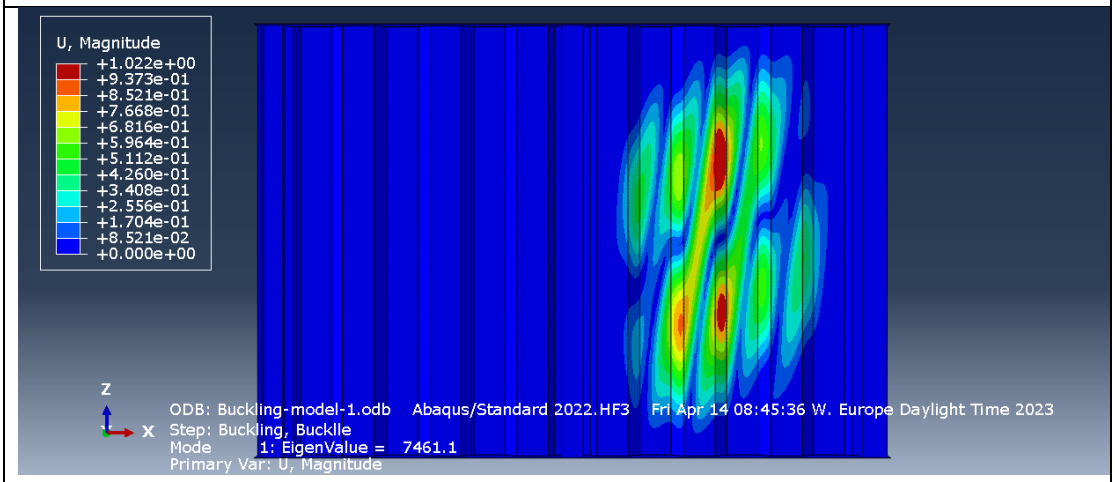

Figure 5.104 Buckling mode 1 for model-15 which is critical for failure with imperfection equal to $\frac{a_{max}}{200}$, t_{w1} *and* $\frac{h_w}{200}$.

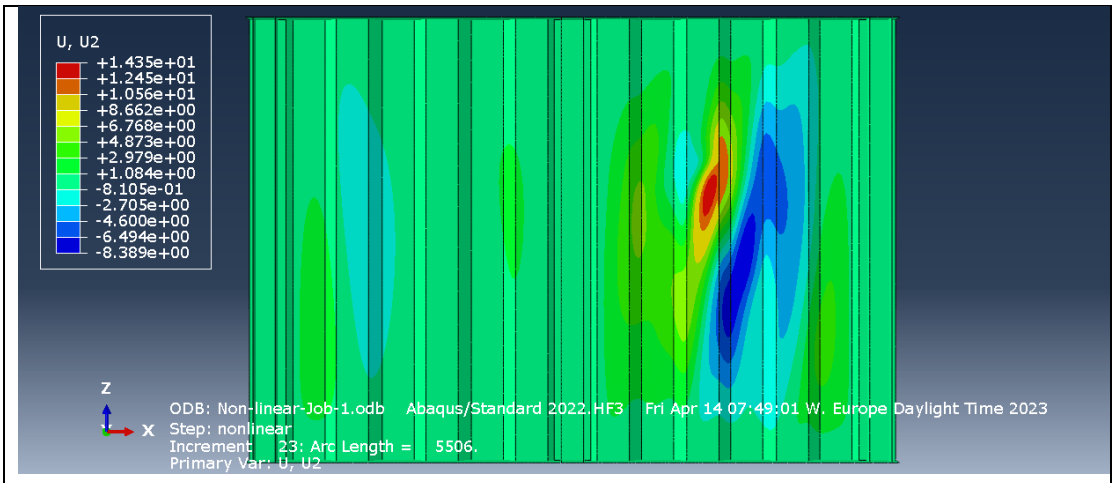

Figure 5.105 Out of plane deflection for model-15 in failure increment with imperfection equal to $\frac{a_{max}}{200}$.

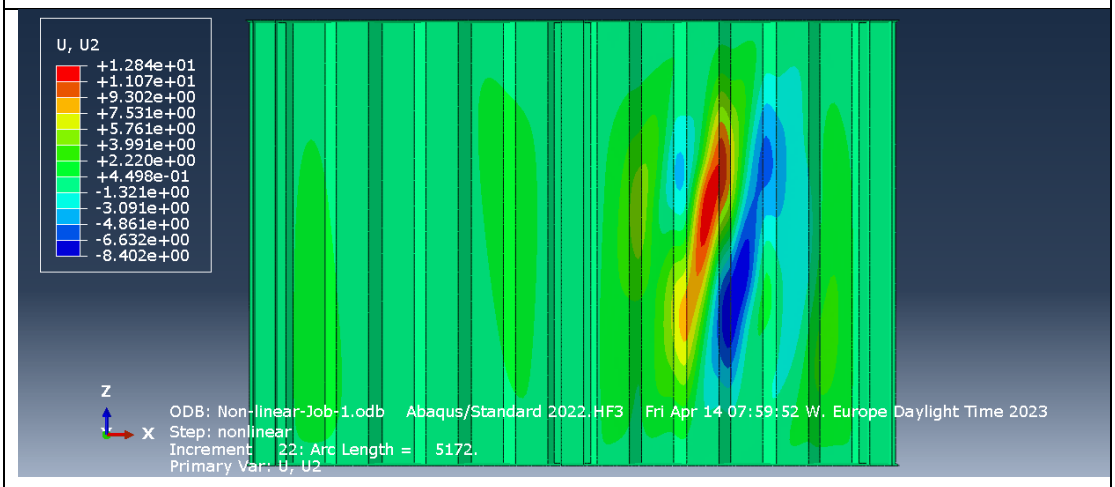

Figure 5.106 Out of plane deflection for model-15 in failure increment with imperfection equal to t_{w1}.

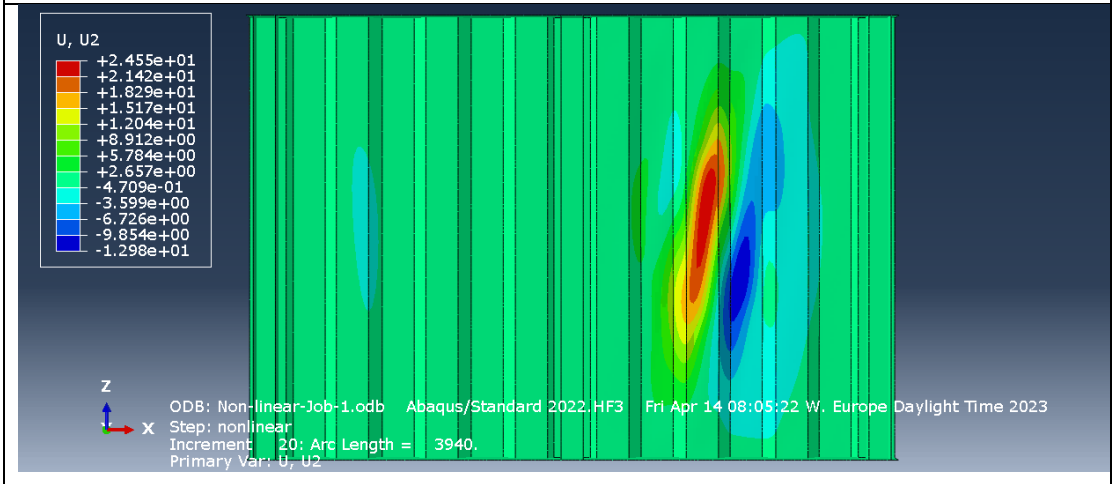

Figure 5.107 Out of plane deflection for model-15 in failure increment with imperfection equal to $\frac{h_w}{200}$.

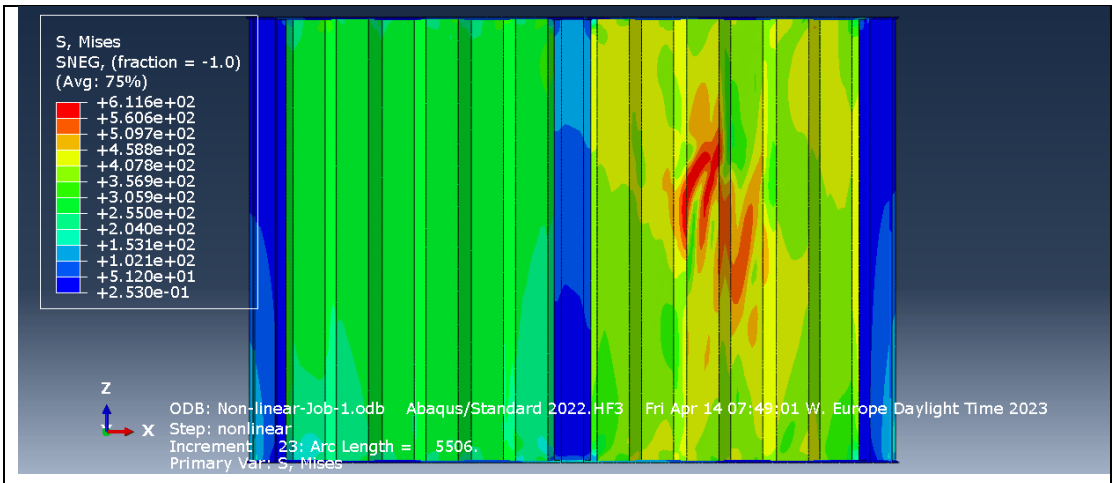

Figure 5.108 Maximum load increment for model-15 with imperfection equal to $\frac{a_{max}}{200}$.

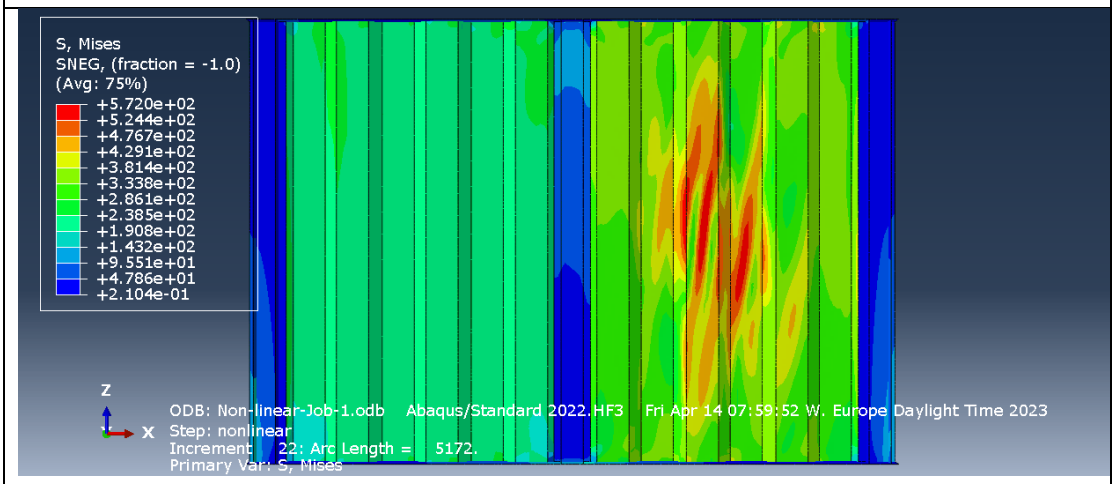

Figure 5.109 Maximum load increment for model-15 with imperfection equal to t_{w1}.

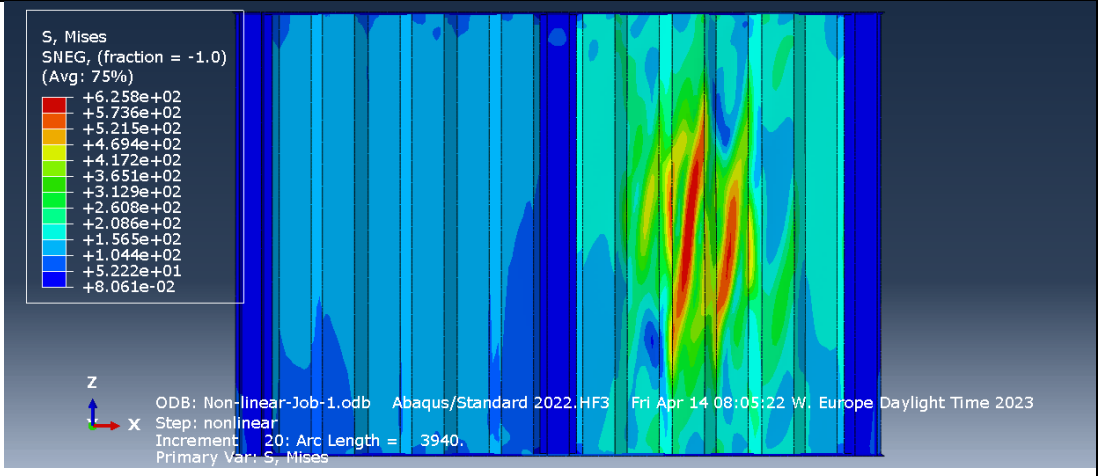

Figure 5.110 Maximum load increment for model-15 with imperfection equal to $\frac{h_w}{200}$.

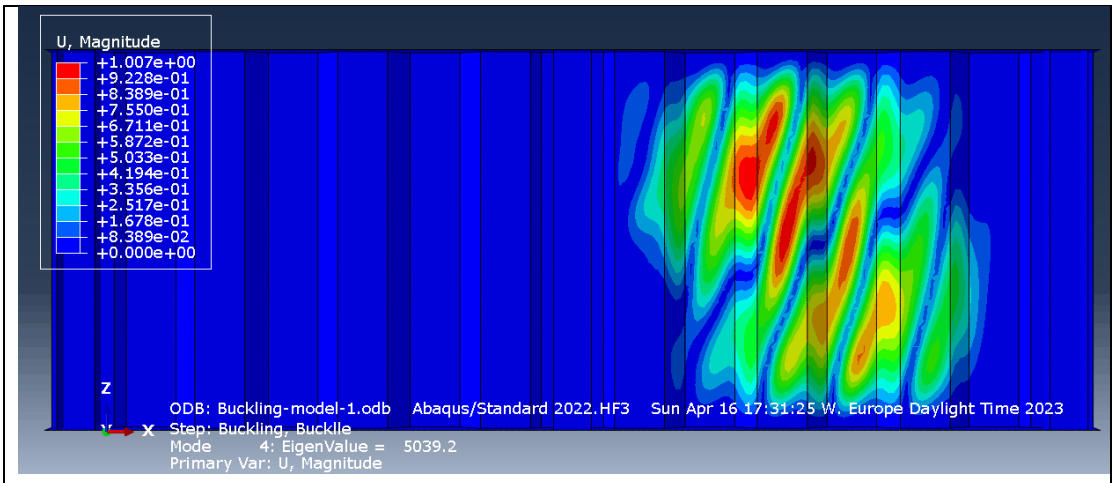

Figure 5.111 Buckling mode 4 for model-16 which is critical for failure with imperfection equal to $\frac{a_{max}}{200}$, t_{w1} *and* $\frac{h_w}{200}$.

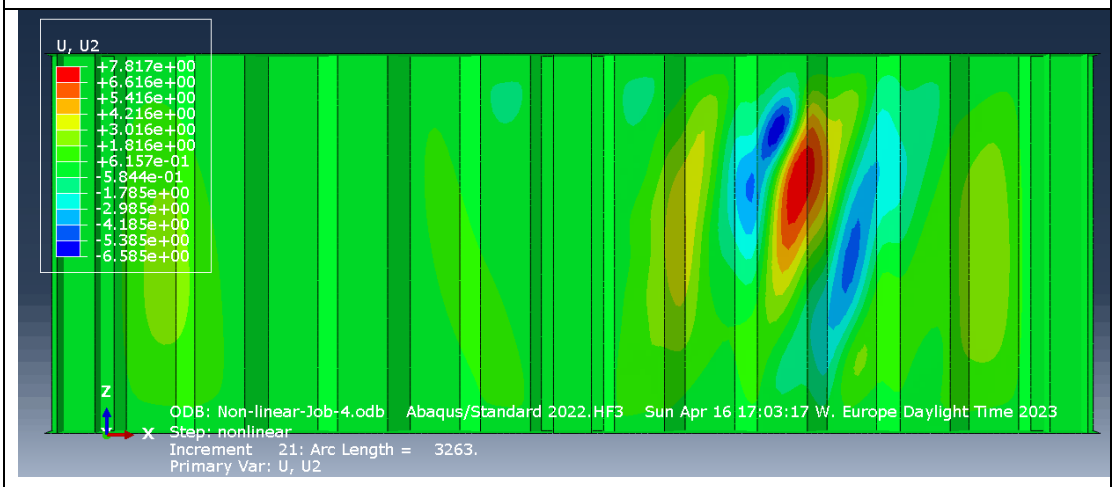

Figure 5.112 Out of plane deflection for model-16 in failure increment with imperfection equal to $\frac{a_{max}}{200}$.

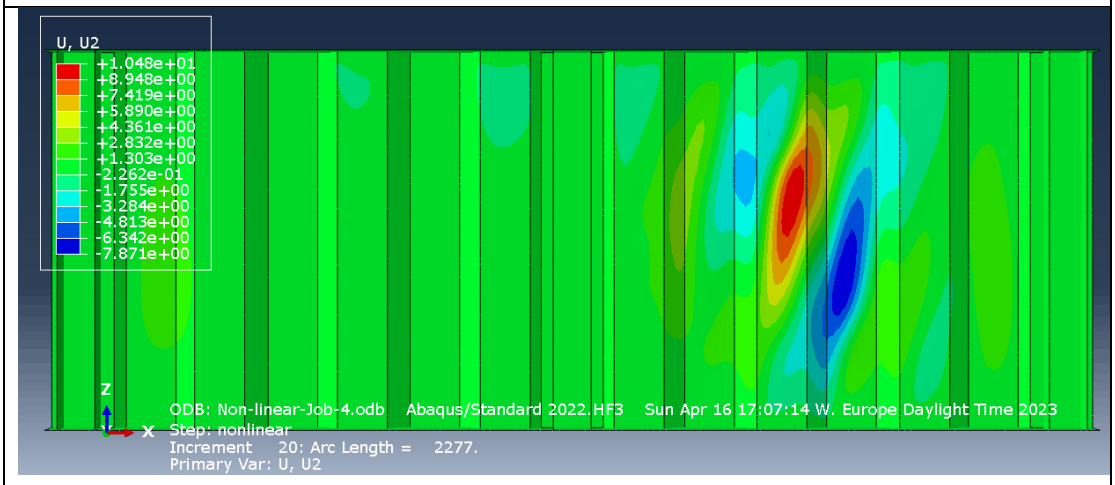

Figure 5.113 Out of plane deflection for model-16 in failure increment with imperfection equal to t_{w1}.

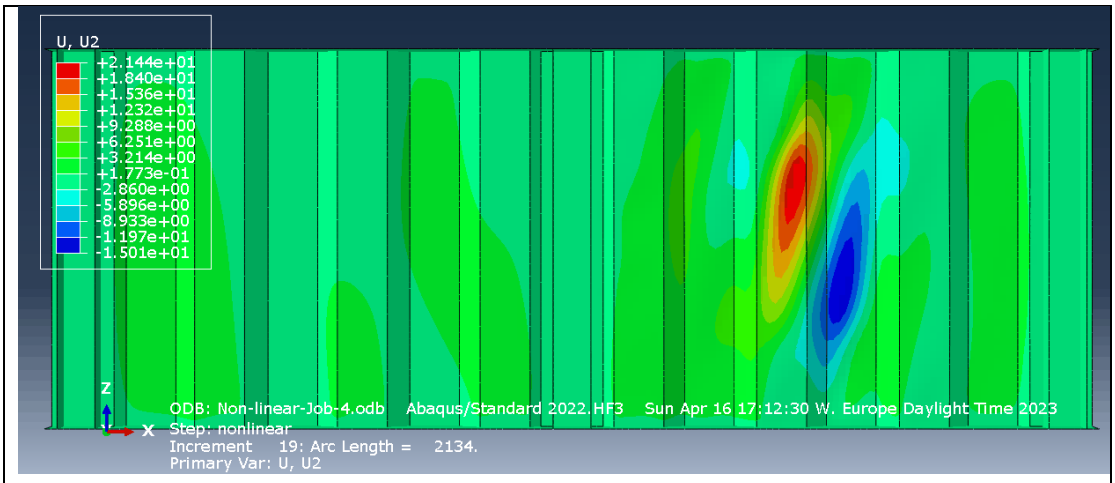

Figure 5.114 Out of plane deflection for model-16 in failure increment with imperfection equal to $\frac{h_w}{200}$.

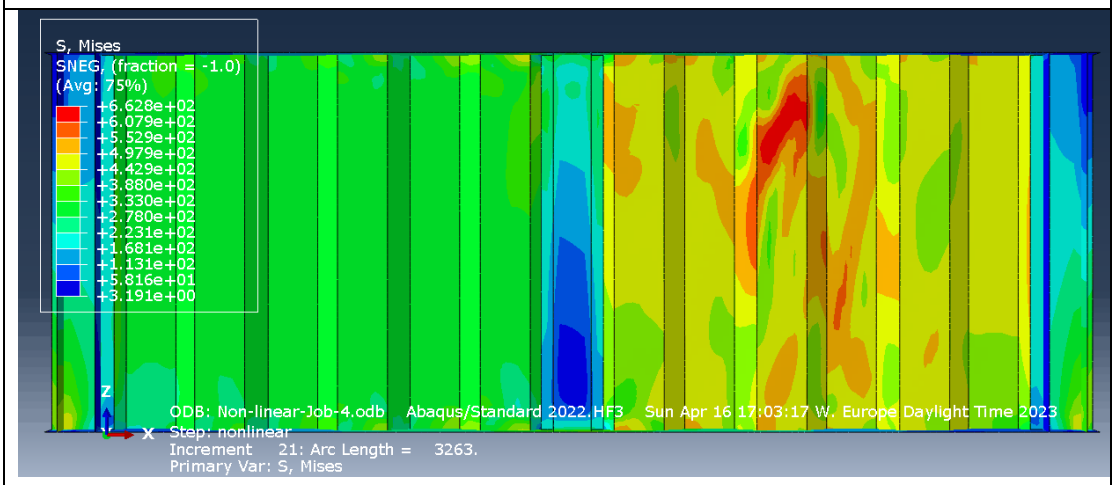

Figure 5.115 Maximum load increment for model-16 with imperfection equal to $\frac{a_{max}}{200}$.

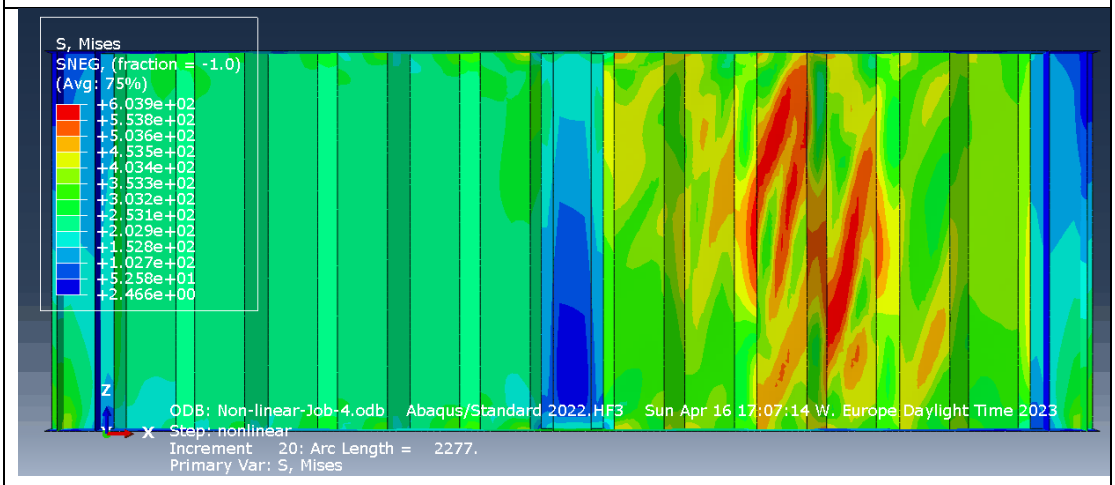

Figure 5.116 Maximum load increment for model-16 with imperfection equal to t_{w1}.

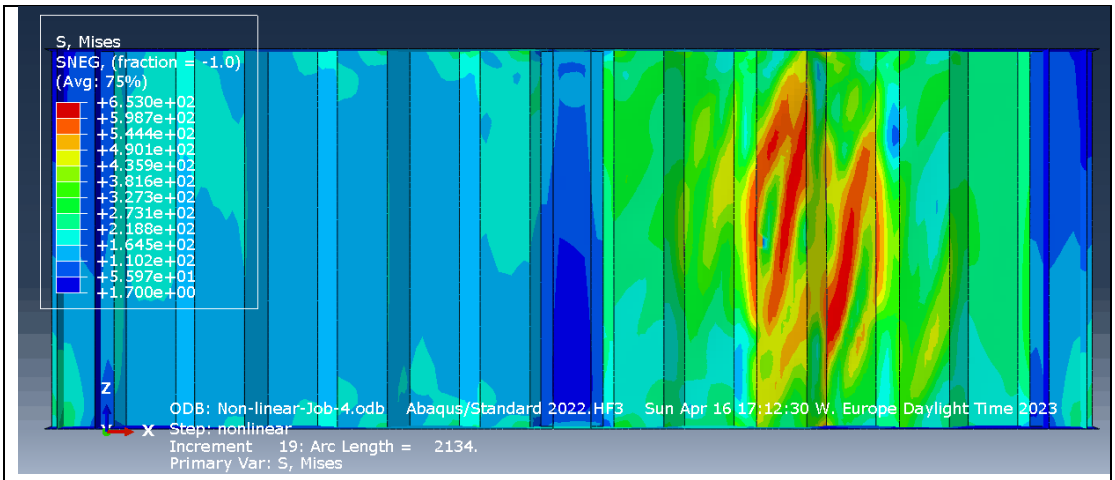

Figure 5.117 Maximum load increment for model-16 with imperfection equal to $\frac{h_w}{200}$

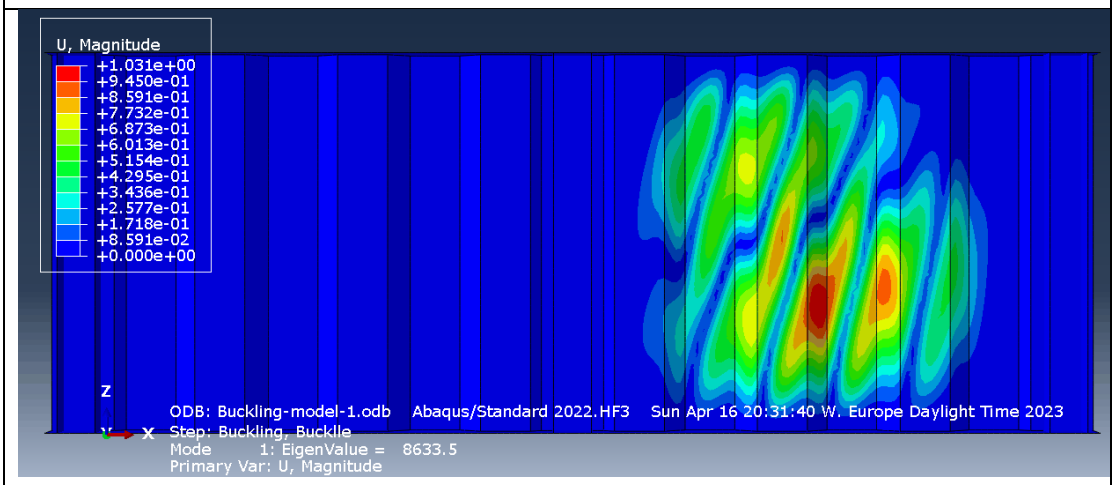

Figure 5.118 Buckling mode 1 for model-17 which is critical for failure with imperfection equal to $\frac{a_{max}}{200}$.

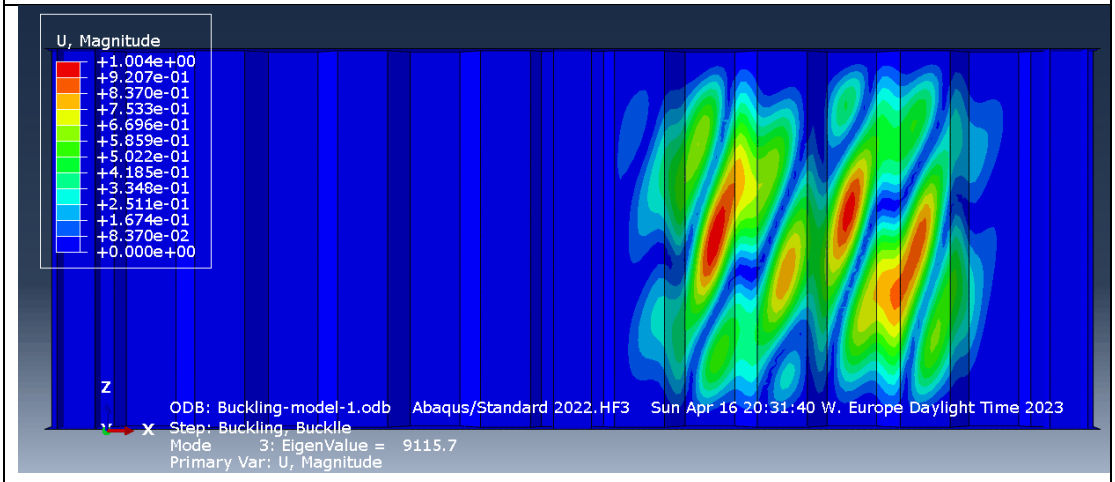

Figure 5.119 Buckling mode 3 for model-17 which is critical for failure with imperfection equal to t_{w1} *and* $\frac{h_w}{200}$.

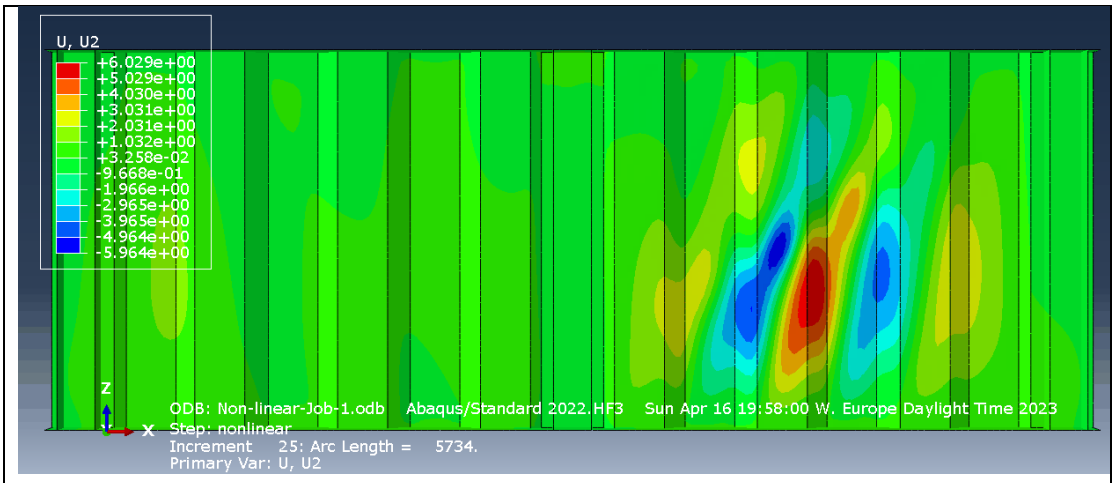

Figure 5.120 Out of plane deflection for model-17 in failure increment with imperfection equal to $\frac{a_{max}}{200}$.

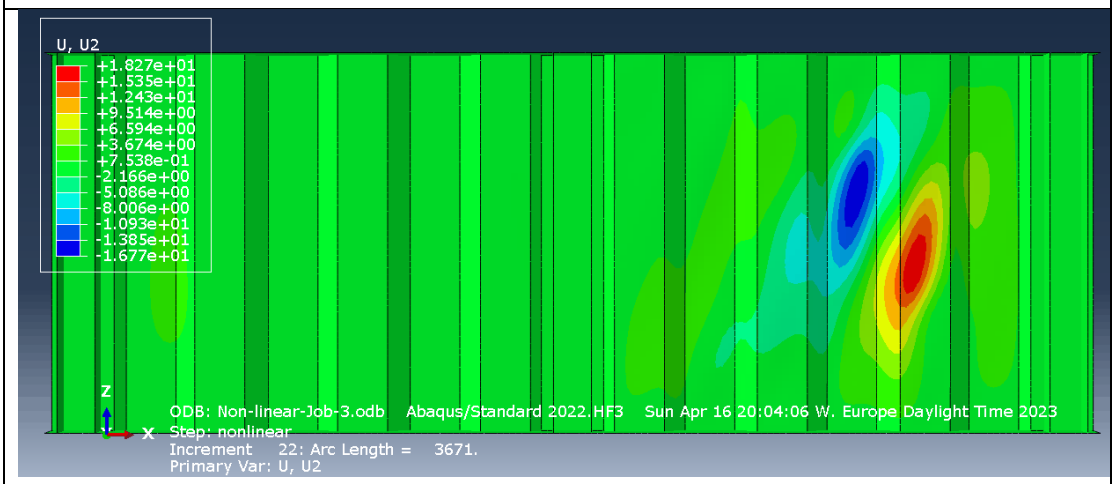

Figure 5.121 Out of plane deflection for model-17 in failure increment with imperfection equal to t_{w1}.

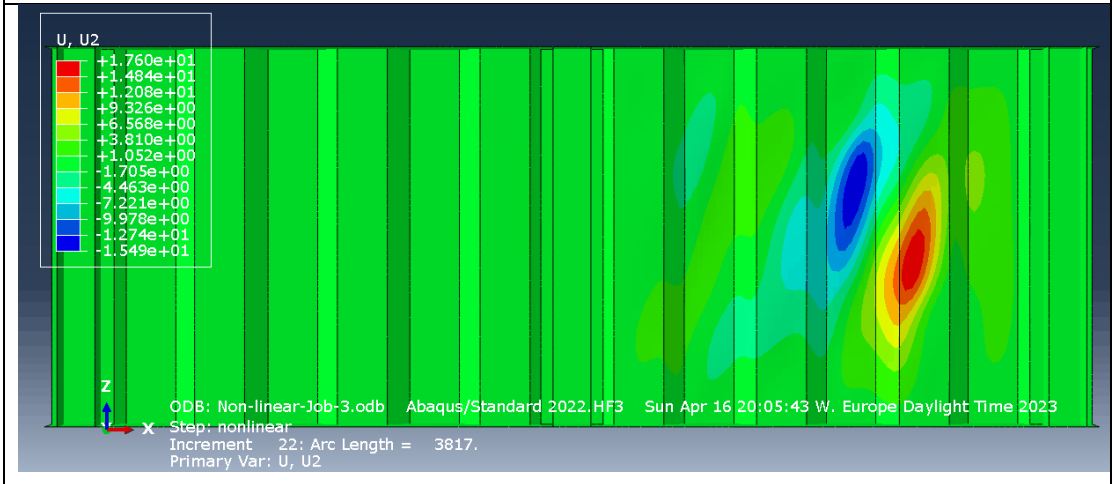

Figure 5.122 Out of plane deflection for model-17 in failure increment with imperfection equal to $\frac{h_w}{200}$.

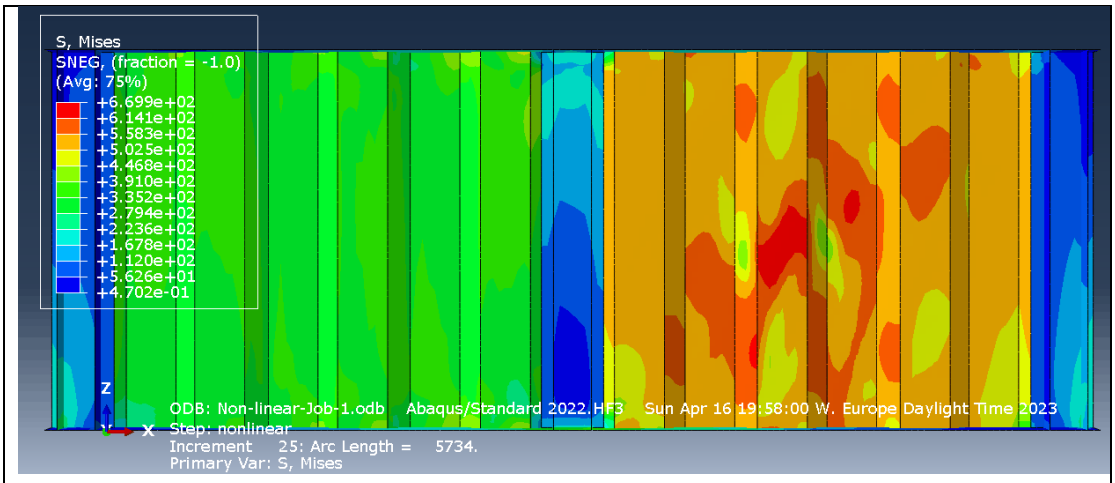

Figure 5.123 Maximum load increment for model-17 with imperfection equal to $\frac{a_{max}}{200}$.

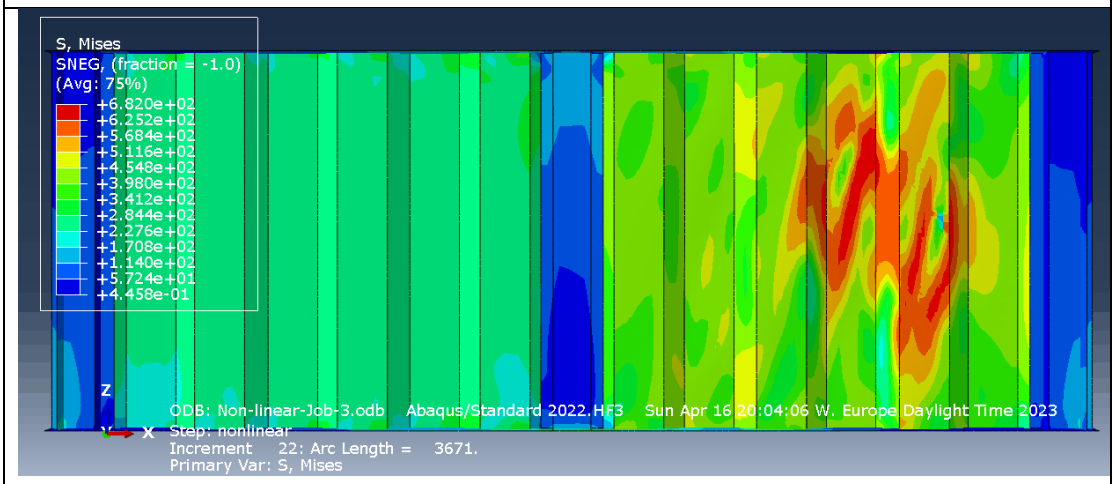

Figure 5.124 Maximum load increment for model-17 with imperfection equal to t_{w1}.

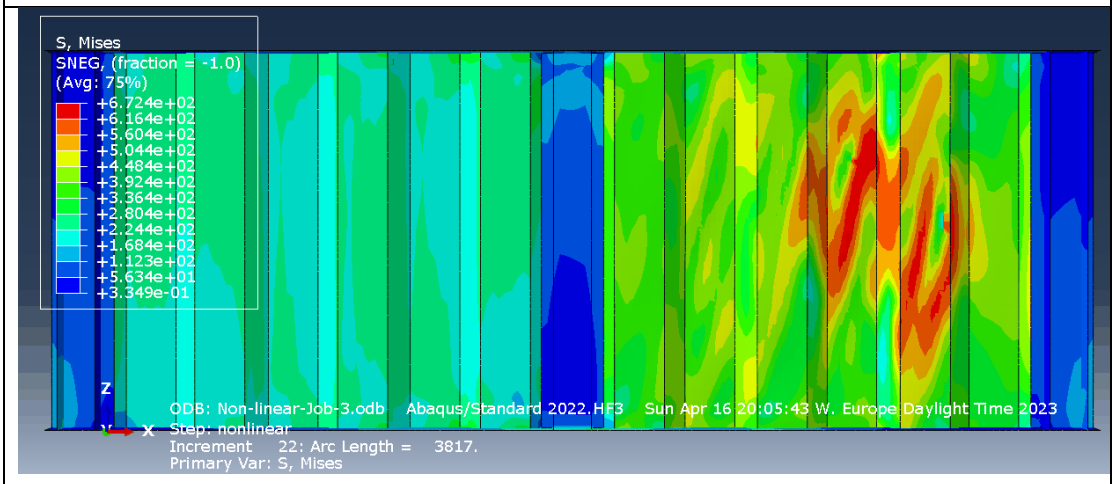

Figure 5.125 Maximum load increment for model-17 with imperfection equal to $\frac{h_w}{200}$.